THERMOMECHANICAL CYCLIC RESPONSE OF TiNiPd HIGH-TEMPERATURE SHAPE MEMORY ALLOYS

A Dissertation

by

KADRI C. ATLI

Submitted to the Office of Graduate Studies of
Texas A&M University
in partial fulfillment of the requirements for the degree of

DOCTOR OF PHILOSOPHY

August 2011

Major Subject: Mechanical Engineering

Thermomechanical Cyclic Response of TiNiPd

High-Temperature Shape Memory Alloys

THERMOMECHANICAL CYCLIC RESPONSE OF TiNiPd HIGH-TEMPERATURE SHAPE MEMORY ALLOYS

A Dissertation

by

KADRI C. ATLI

Submitted to the Office of Graduate Studies of
Texas A&M University
in partial fulfillment of the requirements for the degree of

DOCTOR OF PHILOSOPHY

Approved by:

Chair of Committee,	Ibrahim Karaman
Committee Members,	K. Ted Hartwig
	Dimitris C. Lagoudas
	Ronald D. Noebe
	Xinghang Zhang
Head of Department,	Jerald Caton

August 2011

Major Subject: Mechanical Engineering

ABSTRACT

Thermomechanical Cyclic Response of TiNiPd High-Temperature Shape Memory Alloys. (August 2011)

Kadri C. Atli, B.S., Bogazici University;

M.S., Bogazici University

Chair of Advisory Committee: Dr. Ibrahim Karaman

TiNiPd high-temperature shape memory alloys (HTSMAs) have attracted considerable attention as potential solid-state actuators capable of operating at temperatures up to 500 °C, exhibiting excellent corrosion resistance, adequate ductility levels and significant strain recovery under both constrained and unconstrained thermomechanical conditions. During operation, these actuators may be subjected to multiple cycles and from an application point of view, the functional stability, i.e. conservation of original actuator dimensions and transformation temperatures during repeated employment, is of considerable importance.

This study addresses functional stability in a model HTSMA, $Ti_{50.5}Ni_{24.5}Pd_{25}$, for actuator applications. Since the primary reason for functional instability is the creation of lattice defects (dislocations, vacancies, etc.) during repeated transformation cycles, several methods were successfully undertaken to improve the functional stability through inhibiting the generation of these defects. Solid-solution strengthening through Sc microalloying and severe plastic deformation (SPD) were two approaches used to

strengthen the HTSMA against defect generation. Thermal cycling under stress was the third method to voluntarily introduce defects into the microstructure such that further defect generation during application would be impeded. Overall, SPD was found to be more efficient than other strengthening methods in improving the functional stability, yet it brought about disadvantages such as reduction in transformation strain and transformation temperatures.

While functional instability is due to the creation of lattice defects, the generation of these defects is mainly controlled by the crystallographic incompatibility between martensitically transforming phases and the strength levels for plastic deformation. It was shown that TiNiPd HTSMAs, which exhibited martensitic transformation from a cubic to orthorhombic symmetry, illustrated better compatibility and thus better functional stability levels compared to TiNi SMAs, which had a cubic to monoclinic transition. Although crystallographic incompatibility seems to be the governing factor for the functional stability of the TiNiPd HTSMA, the strength differential between the onset of plastic deformation and local constraint due to the martensitic transformation was also found to be an influential factor determining the overall stable behavior.

Functional stability was also investigated for the two-way shape memory effect (TWSME) in TiNiPd HTSMAs. Better strength and compatibility levels compared to TiNi SMAs were also reflected in the TWSME characteristics in the form of enhanced stability under stress-free thermal cycling. The stability during constrained thermal cycling was not as good and TWSME degraded rapidly while doing work against an opposing stress.

To my family who has given tremendous support and motivation at all times

ACKNOWLEDGEMENTS

I would like to express my respect and gratitude to my graduate advisor, Dr. Ibrahim Karaman, for believing in me and giving me the chance of pursuing a doctoral degree. During my four years of education and research, he has been a role model for me with his unparalleled discipline, perseverance and hard work in every aspect of life and his great enthusiasm for research.

I would like to thank Dr. Dimitris C. Lagoudas, Dr. K. Ted Hartwig and Dr. Xinghang Zhang for serving in my committee and giving valuable suggestions during my studies.

I am indebted to Dr. Ronald D. Noebe, Dr. Anita Garg, Darrell Gaydosh and Glen Bigelow, members of NASA Glenn Research Center, Structural and Materials Division. This dissertation could not have been accomplished without the insightful discussions and support of these people. Special thanks to Dr. Noebe for his guidance and assistance with writing all the internationally recognized journal papers I could put together, proofreading the dissertation and also serving as a committee member. I am grateful to Dr. Garg for her assistance with electron microscopy studies; Darrell Gaydosh and Glen Bigelow for conducting numerous thermomechanical tests and sharing their results.

Robert Barber is credited for his help on the dirty part of the experimental work of the study, i.e. severe plastic deformation by equal channel angular extrusion. Without his expertise, several chapters would be missing from this dissertation. I would like to

thank Prof. Chumlyakov for his fruitful discussions and broadening my knowledge on the subject.

I would have never guessed that a bad situation, like lack of funding to pay my tuition, could turn well. I would like to thank Prof. Hans J. Maier for saving me from the Texas summer and hosting me for three months in the wonderful city of Paderborn, Germany. He and his group showed me that working as a team is the most essential key to success in research and that quality research is indeed possible without working in isolation for 100 hours a week.

I would like to thank all the colleagues I worked with over the years, who made my stay in College Station a memorable and tolerable one: Ji Ma, James A. Monroe, Dr. Burak Basaran, Nevin Ozdemir, Ebubekir Dogan, Cengiz Yegin, Ruixian Zhu, Erhan Akin, Sonia M. Razavi, Murat Kaynak, Alper Evirgen, Brian E. Franco. A special thanks to Ji Ma for always being there to assist and for being both a mentor and a teacher to me; to Dr. Burak Basaran for his great friendship, caring and support and to Nevin Ozdemir, who was always available for an afternoon coffee and who helped me relieve the stress of the day. I also wish to thank Brian E. Franco for his help with experimental setups and testing.

Last but not least, I am forever indebted to the continuous support and courage I received from my family. This dissertation would never have started or ended without their emotional support.

NOMENCLATURE

AISI:	American Iron and Steel Institute
A_f:	Austenite finish
A_s:	Austenite start
BSE:	Backscattered electron
CSS:	Critical shear stress
ΔH_{net}:	The net amount of heat released during phase transformation
DSC:	Differential scanning calorimetry
EDM:	Electrical discharge machining
EDS:	Energy-dispersive spectroscopy
ε_{irr}:	Irrecoverable strain
ε_{rec}:	Recovered transformation strain
ε_{total}:	Total irrecoverable strain generated during thermomechanical training
GNLTM:	Geometric non-linear theory of martensite
HTSMA:	High-temperature shape memory alloy
HV:	Vickers hardness
ICP-AES:	Inductively coupled plasma atomic emission spectroscopy
M_f:	Martensite finish
M_s:	Martensite start
OWSME:	One-way shape memory effect
SAD:	Selected area diffraction

SE: Superelasticity

SEM: Scanning electron microscopy

σ_{SIM}: Critical stress to induce martensite

σ_y^M: The yield strength of the stress-induced martensite

SMA: Shape memory alloy

TEM: Transmission electron microscopy

TRIP: Transformation induced plasticity

TWSME: Two-way shape memory effect

WDS: Wavelength-dispersive spectroscopy

XRD: X-ray diffraction

TABLE OF CONTENTS

Page

CHAPTER Page

CHAPTER Page

CHAPTER Page

LIST OF FIGURES

Page

Page

Page

Page

Page

Page

Page

LIST OF TABLES

Page

Page

CHAPTER I

INTRODUCTION

This chapter introduces the need and significance for the development of functionally stable TiNiPd high-temperature shape memory alloys (HTSMAs) to be used as solid-state actuators. The issue of functional stability, which is critical for the application of HTSMA actuators, is discussed and the methods for its improvement are summarized. At the end, the objectives of the present study are stated along with an outline of the experimental work to meet these objectives.

1.1 Motivation and Significance

Shape memory alloys (SMAs) undergo a diffusionless martensitic transformation, giving them the ability to recover large amounts of inelastic strains through superelasticity (SE) and shape memory effect (SME). Since their discovery in 1960s, TiNi based SMAs have attracted a great deal of interest due to their excellent mechanical properties. Despite being an intermetallic compound, TiNi is quite ductile, such that 60 % cold work is possible under certain conditions [1]. It also has outstanding corrosion resistance. Due to these advantages, most of the applications utilizing SMAs developed so far (e.g. cell-phone antenna, orthodontic wires, stents, switches, coupling for piping…) make use of TiNi alloys. The biomedical field, exploiting mostly the SE

This dissertation follows the style of Acta Materialia.

effect of SMAs, holds a major part of the actual market share. However, TiNi based SMAs are more often cited for their actuation capabilities, which stem from their shape memory behavior. Indeed, they can exhibit large recovery strains (up to 8 %) and large recovery stresses under constrained conditions (up to 800 MPa) in the solution treated condition when heated above their transformation temperatures [2]. This effect has led to the commercial application of TiNi SMAs as actuators performing work against a biasing force, and as fastening or clamping devices. Some potential applications, such as various aeronautic and underhood automobile applications require the SMA to operate at elevated temperatures. However, conventional binary TiNi SMAs have low transformation temperatures limiting their use well below 100 °C [3]. The unique properties of SMAs become much more critical at higher operating temperatures, since it is desirable to adopt simple, monolithic adaptive structures over complicated multi-component assemblies, which will occupy smaller spaces and be exposed to less wear and damage.

The use of ternary additions to TiNi, such as Au, Pt, Hf, Zr and Pd, has been successfully implemented to achieve increased transformation temperatures above 100 °C. Since the discovery of the martensitic transformation in TiPd by Donkersloot and Van Vucht [4], and the fact that TiPd and TiNi binaries form a continuous solid solution with a high temperature B2 phase, TiNiPd high-temperature SMAs (HTSMAs) have attracted significant attention as a potential choice for commercial actuator applications requiring high operating temperatures [5-10]. There are several reasons for such interest. TiNiPd alloys offer a potential operating temperature range, based on the transformation

temperatures, of 100 °C to about 500 °C at Pd contents ranging from 20 % to 50 % [3, 4, 10-12]. Their thermal hysteresis is narrow, which is ideal for applications requiring efficient and active, fast control. They have reasonable ductility and do not exhibit premature intergranular cracking, as frequently observed in some alternative alloys like CuAlNi [13]. Finally, TiNiPd alloys are capable of significant strain recovery under stress-free, as well as constrained conditions upon heating [5, 9, 14, 15].

In addition to the aforementioned properties, a reliable HTSMA should demonstrate long term microstructural stability and resistance to oxidation over its operating temperatures. It should have high resistance to dislocation slip in the high-temperature austenite phase to resist high-temperature deformation and thermally driven mechanisms such as recovery, recrystallization, and creep. At the same time, a stable HTSMA should be strong in both the high-temperature austenite and the low-temperature martensite phase, to prevent simultaneous macroscopic plasticity during detwinning/reorientation processes [12, 16, 17]. Transformation induced plasticity (TRIP), which is due to the accommodation of the transformation shear and volume change with defect generation, such as dislocations, during the transformation is also a concern [18, 19]. TRIP can take place at externally applied stress levels much lower than the plastic yield strengths of either of the transforming phases [16]. In addition, if the critical shear stress (CSS) for slip is low, then macroscopic plasticity can take place simultaneously during the transformation process [16]. However, macroscopic plasticity is usually pronounced above a certain temperature; whereas TRIP may even occur at low

temperatures [12]. All these problems contribute to the deterioration of shape memory behavior and lead to functional instability during actuation.

Functional stability of an SMA actuator has been characterized by the changes in its transformation temperatures and its cold and hot shapes during repeated actuation [20]. Hornbogen [21] listed several conditions to achieve improved functional stability in SMAs. Most of these conditions, such as the degree of order, interference of transformation by diffusion, and embrittlement of grain boundaries, are intrinsic material properties and overcoming these limitations is difficult, if not impossible and may require substantial changes in the constitution and composition of the alloy. However, one condition, i.e. maximizing the strength of the parent phase, is more practical and has been exploited frequently for conventional alloys such as TiNi and Cu-based SMAs. Yet, there is limited work in this area for HTSMAs. Within this framework, several methods have been proposed to improve the functional stability of TiNiPd HTSMAs through increasing the strength of the parent phase [12]. Some of these methods are solid solution strengthening through quaternary alloying [22-26], thermomechanical processing using severe plastic deformation (SPD) and post deformation annealing heat treatments [5, 7], and precipitation hardening [9]. All these possibilities are geared towards increasing the CSS for slip deformation of the material hindering the formation of additional defects. Therefore, the goal is to make sure that any strain generated within the material during the martensitic transformation would be reversibly accommodated, minimizing the chances of slip deformation and other defect generation mechanisms, leading to improved high-temperature shape memory properties.

With the exception of the works performed by Bigelow *et al.* [14, 15, 25] and Kumar *et al.* [27], the previously mentioned studies on the TiNiPd alloy system have primarily focused on the determination of transformation temperatures as a function of composition and the characterization of phase transformation and shape recovery under no-load conditions. However, for a new SMA to be used effectively in an actuator application, it is imperative to know the shape memory behavior of the material under constrained conditions, including its work output and functional stability under isobaric thermal cyclic loading. Functional stability is of utmost importance, since a permanent change in the shape of the material or a shift in transformation temperatures during cyclic loading may render the SMA inoperable and necessitate the replacement of the actuator. Among the very few works focusing on actuation characteristics of TiNiPd, Noebe *et al.* [14] have recently determined the strain-temperature response and work output of $Ti_{50.5}Ni_{19.5}Pd_{30}$ (at. %) under different stress levels both in tension and compression. Bigelow *et al.* [15] compared the transformation temperatures, work output and dimensional stability of different $Ti_{50.5}Ni_{49.5-x}Pd_x$ compositions containing 15 to 46 at.% Pd. From this limited number of investigations, it is clear that functional stability during isobaric thermal cycling is a major concern with this family of HTSMAs and any of the previously mentioned strengthening methods should be directed towards improving the functional stability of this alloy system for actuator applications.

Thermomechanical cycling, also known as “training”, is the most commonly used method in the SMA community to obtain stable material behavior [28]. It thus represents an alternate method to the aforementioned classical strengthening methods.

Through either stress cycling above the austenite finish (A_f) temperature, or thermal cycling through the martensitic transformation under a constant stress, structural defects (e.g. point defects, dislocations and internal interfaces) are created in the material to accommodate the strains generated during the transformation [29, 30]. Each subsequent cycle induces fewer defects until a saturation level is reached and eventually only minor changes are seen in the functional stability upon further cycling (i.e. a stable behavior is obtained). A training procedure may consist of as low as ten thermal cycles, or as high as thousands of cycles depending on the level of stability desired from the SMA. For the sake of clarity throughout this dissertation, the term "thermomechanical training" or simply "training" will be used for any thermomechanical cycling procedure involving a hundred or more cycles.

While there is a vast amount of information available for the training of conventional SMAs such as TiNi or Cu-based SMAs, there are only a limited number of studies on the training of TiNiPd HTSMA's. Early studies were conducted by Cai *et al.* [31] on $Ti_{50.6}Ni_{19.4}Pd_{30}$ (at. %) focusing on the evolution of shape memory characteristics during the course of a training procedure consisting of a hundred thermal cycles under different training stress levels, i.e. shift of transformation temperatures, evolution of transformation strain and total plastic strain. In a recent study by Bigelow *et al.* [32], the hundred cycle training response of $Ti_{50.5}Ni_{24.5}Pd_{25}$ (at. %) HTSMA was compared to that of equiatomic TiNi. The two materials illustrated very different evolutionary behaviors evidenced by the number of cycles to reach stable behavior and the level of stability at the end of training.

An ideal practical SMA should acquire a stable behavior in as few cycles as possible since the training itself is a long and costly process. The understanding of the SMA's response to training and the identification of microstructural parameters involved in this process is thus of critical importance. Ultimately, it would be very convenient for SMA designers, if it were possible to come up with simple microstructural parameters that are easily measurable and that will indicate whether an SMA would demonstrate good functional stability without actually testing for it. Essentially, strength of the parent phase, which could be increased by several strengthening methods as previously mentioned, is one of these parameters. Another parameter is the crystallographic compatibility between transforming phases, which was recently studied by Grossman *et al.* [33] on TiNi and TiNiCu spring actuators. The substitution of Cu in place of Ni changed the crystal structure of the martensite from monoclinic (B19') to orthorhombic (B19). TiNiCu actuators accumulated a smaller amount of total plastic strain during training and acquired a stable behavior in a fewer number of cycles compared to TiNi actuators, due to increased crystallographic compatibility between the transforming phases and solid-solution hardening effect of Cu addition.

To the author's best knowledge, the effects of microstructural parameters, such as crystal structure, grain size, dislocation density, existence of second-phase particles, on the evolutionary transformation response during training has not yet been studied in TiNiPd HTSMAs. For a better understanding of the actuation properties of the stable material, evolutionary response of TiNiPd HTSMAs during training should be assessed taking these microstructural effects into consideration. In addition, training parameters

such as the applied stress level and temperature interval should also be considered. The results of such a study will greatly benefit the SMA community in terms of materials selection, optimization of the parameters for less cumbersome and quick training processes and at the same time providing data for model development to predict actuator response.

The fact that the shape memory effect can be used to do work against a load has led to the development of SMAs as compact, solid-state actuators. Compared to D.C. motors or their pneumatic counterparts, these actuators have several advantages such as light weight, reduction in total part count, ease of inspection and higher energy densities. SMA actuators mostly operate based on the one-way shape memory effect (OWSME) combined with a biasing force to reset the SMA after each actuation cycle. However, it would be advantageous in terms of the simplicity of design to eliminate the need for resetting the actuator. In this respect, the two-way shape memory effect (TWSME) renders it possible for an actuator to remember both its low-temperature and high-temperature shapes without the need for a biasing force. Unlike OWSME, TWSME is not an inherent characteristic of SMAs, but rather it is obtained after thermomechanical treatments (training), such as stress or temperature cycling.

Early studies on TWSME mostly concentrated on conventional Cu-based [28, 34-41] and binary TiNi SMAs [42-59]. These studies mainly focused on the mechanism of TWSME, its generation using different training procedures, and the effects of training parameters on the magnitude and stability of the TWSME. Similar studies were also conducted on ternary TiNi based SMAs, such as TiNiCu [59-62], TiNiFe [56] and

TiNiNb [63, 64]. However, there is very limited data on the characterization of TWSME in HTSMAs. The only study in this field for TiNi based HTSMAs was performed for TiNiHf [65], which exhibited a poor TWSME with a small strain output and large degradations upon thermal cycling due to the low strength of the alloy.

To date, there has not been a systematic study on the TWSME characterization of TiNiPd HTSMAs. There is an urgent need to reveal the existence, methods of generation and cyclic stability of TWSME in these HTSMAs for actuator applications and investigate the methods to enhance the stability. Since most of the emerging actuator applications require SMAs to do work against a load, it is also essential to determine the work output of TWSME in HTSMAs and its stability during actuation.

1.2 Objectives

With this short background, the purpose of the present research can be summarized as an intensive thermomechanical processing and characterization study of a model HTMSA, $Ti_{50.5}Ni_{24.5}Pd_{25}$ (at.%), in an effort to obtain enhanced functional stability for high-temperature actuator applications and understand the influence of microstructural parameters on the functional stability. The selection of the TiNiPd HTMSA with 25 at.% Pd as the baseline model alloy is due to its intermediate transformation temperatures (near 200 °C) with relatively good shape memory characteristics.

The first focus of the study is on the enhancement of shape memory properties, in particular the functional stability during repeated thermomechanical cycles. Several

processing methods, such as solid-solution strengthening using a quaternary alloying element, severe plastic deformation (SPD) and thermomechanical cycling under a constant stress are undertaken to accomplish this goal. These methods have already been proven to work for conventional TiNi and Cu-based SMAs.

The second focus is to investigate the evolutionary response of the HTSMA during high-cycle training in an effort to understand how microstructural characteristics and training parameters influence the functional stability of the trained material. The feasibility of utilizing the TWSME for high-temperature actuator applications is also evaluated by characterizing its stability during thermal cycling and work production.

The overall objectives of the current study are:

1. Thermomechanical characterization of a base model $Ti_{50.5}Ni_{24.5}Pd_{25}$ (at.%) HTSMA through extensive thermomechanical testing, electron microscopy, and X-ray diffractometry.
2. Investigation of the effects of thermomechanical processing including
    a. solid-solution strengthening via Sc additions (0.5 and 3 at. %),
    b. work hardening and grain refinement through SPD using equal channel angular extrusion (ECAE) and
    c. thermomechanical cycling under constant stress levels

on the shape memory characteristics, particularly the functional stability of the $Ti_{50.5}Ni_{24.5}Pd_{25}$ (at.%) HTSMA using the above mentioned characterization techniques.

3. Understanding of the evolution of shape memory behavior through extensive experimentation and structural characterization to reveal correlations with functional

stability and to eventually define simple indications of functional stability. Specifically, the effects of microstructural parameters such as

a. crystallographic compatibility between transforming phases (by comparing HTSMA systems with different crystal structures and lattice parameters),
b. grain size and dislocation density (through ECAE processing)
c. differences in chemistry (using off-stoichiometric alloy systems, e.g. Ni-rich TiNiPd)

on the evolution of the shape memory behavior of $Ti_{50.5}Ni_{24.5}Pd_{25}$ HTSMA are investigated during training under various stress levels. In addition to $Ti_{50.5}Ni_{24.5}Pd_{25}$, a quaternary alloy with Sc addition, a slightly Ni-rich TiNiPd composition, TiNiPt (another HTSMA system), as well as binary TiNi SMA, which all have similar processing histories are subjected to training cycles for this purpose.

4. Characterization of the TWSME for these trained materials, in terms of stability and the magnitude of the TWSM strain during repeated thermal cycling. The effects of training parameters such as applied stress and upper cycle temperature on the stability of the TWSME are also investigated.

5. Characterization of the work output of the TWSME in HTSMAs and investigation of its stability during thermomechanical cycling. The influence of starting microstructure (i.e. dislocation density, grain size, etc.) on the work output stability is also studied.

It is believed that the outcomes of this study will be invaluable for the design of HTSMA actuators exploiting both the OWSME and the TWSME, while accelerating the

incorporation of these HTSMAs into high-temperature actuator applications. The results will also serve as background for model development for the design of actuators and predicting actuator responses. With these objectives, the outline of the dissertation is as follows:

Chapter II: A brief literature review related to the aforementioned objectives, mainly covering several different strengthening methods used to improve the functional stability of TiNiPd HTSMAs. Also included in this review is the significance of the crystallographic compatibility between transforming phases in SMAs and the utilization of different thermomechanical training procedures to obtain stable material behavior while generating the TWSME.

Chapter III: Experimental methods and materials that are used in this study.

Chapter IV: Investigation of the effects of different amounts of Sc, as a model solid-solution strengthener, on the shape memory characteristics and in particular the functional stability of $Ti_{50.5}Ni_{24.5}Pd_{25}$ HTSMA during repeated actuation.

Chapter V: Investigation of the effects of SPD via ECAE on the shape memory characteristics, in particular the functional stability of $Ti_{49.5}Ni_{25}Pd_{25}Sc_{0.5}$ HTSMA during repeated actuation.

Chapter VI: A comparison of the effects of SPD and a low-cycle thermomechanical cycling procedure on the functional stability of $Ti_{50.5}Ni_{24.5}Pd_{25}$ HTSMA.

Chapter VII: High-cycle thermomechanical training of TiNiPd HTSMAs along with other SMA and HTSMA compositions. Characterization of the TWSME, induced

by the training process, in terms of its magnitude and stability during stress-free thermal cycling.

Chapter VIII: An investigation of the work output of the TWSME induced by the high-cycle thermomechanical training procedure employed in Chapter VII and its stability during repeated work actuation.

Chapter IX: An investigation of the influence of microstructural parameters such as crystallographic compatibility, grain size and dislocation density on the evolutionary behavior of the $Ti_{50.5}Ni_{24.5}Pd_{25}$ HTSMA during thermomechanical training.

Chapter X: Main conclusions and future directions.

CHAPTER II

BACKGROUND

This chapter summarizes the previous literature related to the objectives of the present study. It thus provides background to the reader to better interpret the experimental results. In general, this literature review is presented in the same order as the objectives presented in Section 1.2.

2.1 Methods to Obtain Enhanced Functional Stability

2.1.1 Solid-solution Strengthening of TiNiPd Using Quaternary Additions

Tian *et al*. [24] found that the addition of 1 wt. % cerium (Ce) to $Ti_{51}Ni_{21}Pd_{28}$ improved mechanical properties through an increased elastic modulus and yield strength and delayed recrystallization times. However, the Ce addition deteriorated pseudoelasticity and depressed transformation temperatures by about 40 °C.

Bigelow *et al*. [25, 26] investigated the effects of quaternary additions of gold (Au, 5 at. %), platinum (Pt, 5 at. %) and hafnium (Hf, 3 at. %) on the load-biased shape memory response of different compositions of TiNiPd, i.e. dimensional stability, transformation temperatures, and monotonic tensile behavior. While additions of Au and Pt had relatively no effect on the transformation temperatures, Hf suppressed both the martensite finish (M_f) and A_f temperatures by 63 ºC and 70 ºC, respectively. As observed from the monotonic tensile test results, all three quaternary additions improved the yield strength of the austenite phase, which resulted in a more stable

thermomechanical response. The improvements in strength were attributed to solid solution hardening, since no change in microstructure, including the precipitation of any new phase, was observed between the ternary and quaternary alloys.

Other quaternary alloying studies included the addition of boron (B) primarily to improve the ductility of TiNiPd. Yang *et al*. [22] investigated the effects of 0.12 at. % B addition to $Ti_{50.7}Ni_{22.3}Pd_{27}$ and showed an improvement in the room-temperature ductility as a result of grain refinement due to the presence of TiB_2 particles. However, no change in shape memory behavior including the phase transformation temperatures was detected with this B addition. Suzuki *et al*. [23] confirmed the results of Yang *et al.* [22] using 0.2 at. % B addition to $Ti_{50}Ni_{20}Pd_{30}$, which resulted in improved high-temperature strength and ductility, again attributed to a decrease in grain size. As in the previous study, the addition of boron had no significant effect on shape memory behavior, since the resulting TiB_2 particles were too coarse for effective precipitation hardening.

2.1.2 Thermomechanical Processing Using Severe Plastic Deformation

While there is a substantial amount of work covering the effects of thermomechanical processing on the shape memory behavior of TiNi [66-71], data is quite limited for the TiNiPd system. Golberg *et al.* [5-7] studied the effects of cold rolling with different reductions and subsequent annealing at different temperatures on the shape memory behavior of $Ti_{50}Ni_xPd_{50-x}$ HTSMA (x = 10, 15, 20). They recorded 100 % recovery at a total strain of 5.3 % in $Ti_{50}Ni_{20}Pd_{30}$, which was cold rolled down to

a 24-25 % thickness reduction and subsequently annealed at 400 °C for 1 hour [5, 6]. The recovered strain level was more than twice that of the solutionized material, which was only about 2 %. They also demonstrated a partial superelastic effect at A_f + 10 °C in the same processed material for the first time in this alloy system.

Tian *et al.* [72] investigated the mechanical properties of an off-stoichiometric, cold-rolled and annealed $Ti_{50.6}Ni_{19.4}Pd_{30.}$ They recorded full recovery of up to 7.2 % strain and up to 95 % recovery at 11% applied strain after deformation at room temperature and subsequent heating above the A_f temperature. Wu *et al.* [73] recorded a 7 % recoverable superelastic strain in $Ti_{51}Ni_{19}Pd_{30}$ at 240 °C after the sample was trained with multiple superelastic cycles. However, the relatively large strain values recorded in both of these studies are considered to be a result of erroneous strain measurements. An elastic strain of about 5 % was reported for the superelastic loading, corresponding to an elastic modulus of 12 GPa for the austenite phase. On the other hand, the elastic strain of a similar composition, $Ti_{50.5}Ni_{19.5}Pd_{30}$, was found to be around 1 % at a testing temperature of 309 °C (A_f + 50 °C) by Bigelow *et. al* [74].

Kockar *et al.* [75] improved the functional stability of a $Ti_{50.3}Ni_{33.7}Pd_{16}$ HTSMA during thermo-mechanical cycling through the use of ECAE processing. The processed samples accumulated smaller amounts of plastic strains during isobaric cooling-heating experiments as compared to the as-received samples. The improvements in the functional stability levels were attributed to the increase in critical stress for dislocation slip due to the microstructural refinement during the ECAE process.

2.1.3 Precipitation Hardening

Although precipitation hardening is not utilized in the current study as a method to enhance the shape memory behavior of TiNiPd HTSMAs, there are a couple of studies showing its effects. Therefore, it is worth mentioning the past work on the precipitation hardening of TiNiPd HTSMAs for the sake of completeness.

Precipitation hardening has been successfully implemented for both Ti-rich [76] and Ni-rich [77] binary TiNi SMAs to improve the shape memory characteristics. Similarly, it is possible to produce fine precipitates in off-stoichiometric TiNiPd HTSMAs by aging treatments in order to increase the CSS for slip and thus improve shape memory characteristics as well as the functional stability. Within this framework, Shimizu *et al.* [9] improved the recoverability of a Ti-rich $Ti_{50.6}Ni_{19.4}Pd_{30}$ after an aging heat treatment at 500 °C for 3.6 ks. They obtained 10 % more strain recovery at a total strain of 6 % at 197 °C as compared to the stoichiometric $Ti_{50}Ni_{20}Pd_{30}$. The improvement in the shape memory characteristics was reported to be due to the fine, homogenously distributed Ti_2Ni type precipitates increasing the strength of the material.

TiNiHf alloy system is another attractive candidate for HTSMA applications due to its lower cost compared to TiNiX (X=Pd,Pt) HTSMAs and high transformation temperatures [78]. However, it exhibits small recoverable strains and large thermal hysteresis values due to its low CSS for slip and the formation of (001) compound twins instead of Type-I or Type-II twins [79]. Recently, Meng *et al.* [80] proposed a new method to use Ni-rich TiNiHf alloys as HTSMAs through similar aging heat treatments performed for Ni-rich TiNi SMAs. They showed that after an aging treatment at 550 °C

for 5 hrs, transformation temperatures of $Ti_{29.4}Ni_{50.6}Hf_{20}$ increased to the level of the stoichiometric alloy with added strength and enhanced stability of transformation temperature during stress-free thermal cycling. The depletion of Ni from the matrix due to the precipitation of $(Ti,Hf)_3Ni_4$ particles and the concomitant increase in CSS for slip were the reasons for the increase in transformation temperatures and thermal stability, respectively.

2.1.4 Thermomechanical Training

Cai *et al.* [31] studied the evolution of shape memory behavior in a $Ti_{50.6}Ni_{19.4}Pd_{30}$ HTSMA during a training procedure of 100 thermomechanical cycles under various stress levels. They found that shape memory characteristics, such as transformation temperatures, recovered transformation strain, and total irrecoverable strain evolved with the number of cycles and reached stability after about 40 cycles. While the magnitude of the training stress affected the amount of change in the shape memory characteristics, it did not affect the number of cycles required to reach stability.

Bigelow *et al.* [32] investigated the shape memory responses of $Ti_{50.5}Ni_{49.5-x}Pd_x$ (x = 15 to 46) HTSMAs during isobaric cooling-heating experiments under different stress levels. It was shown that with increasing Pd content, the amount of recovered transformation strain decreased while irrecoverable strain increased under a given stress level. It should be noted that transformations taking place at higher temperatures might be partially responsible for the high irrecoverable strain levels due to the reduced CSS for slip of the materials at elevated temperatures. However, continued thermal cycling

under the same stress level resulted in a reasonably stable material behavior after about 40 thermomechanical cycles, with almost the same transformation and irrecoverable strain values per cycle. At the end of 100 thermal cycles under 172 MPa applied stress, $Ti_{50.5}Ni_{24.5}Pd_{25}$ had a saturation value of 0.0087 % for the irrecoverable strain per cycle, which suggested that the material reached an almost dimensionally stable behavior.

2.2 Crystallographic Compatibility and the Evolution of Shape Memory Behavior during Training

Thermal hysteresis is an important criterion in the selection of SMAs for actuator applications. It dictates the amount of undercooling and superheating required to complete transformation. Thus, it is a measure of thermal efficiency. It is also correlated with the fatigue life of the actuator, since the energy lost due to the thermal hysteresis is an indirect indication of the creation of defects [81]. SMAs with low thermal hysteresis values are expected to generate fewer defects during thermomechanical cycling and thus exhibit longer thermomechanical fatigue life.

Recently, a theory called the “geometrically non-linear theory of martensitic transformations”, or geometric non-linear theory of martensite (GNLTM) has emerged on the origins of the reversibility of phase transformations [82, 83]. The theory explains how the shape memory effect is related to the symmetry of the crystal and crystallographic compatibilities. One critical statement of the theory is that the fundamental cause of the transformation hysteresis seen in SMAs arises from the crystallographic incompatibilities between the austenitic and martensitic phases and that

the hysteresis can be significantly reduced by the improvement of the compatibility. Thus, SMAs with improved crystallographic compatibilities are less prone to generation of defects during transformation and are expected to be more resistance to failure during repeated thermomechanical cycling.

The GNLTM postulates two criteria in order for an SMA to exhibit a small hysteresis. The first condition is det$\mathbf{U}$ = 1, where $\mathbf{U}$ is the transformation stretch matrix that maps the austenite lattice to martensite lattice during transformation. In geometric terms, det$\mathbf{U}$=1 represents the condition of no volume change. This condition has been widely considered as a prerequisite for the reversibility of martensitic transformations [84, 85]. If there is a volume change associated with the transformation, an island of martensite growing in austenite will impose stress to its surroundings. This would also happen during the reverse transformation. Thus, the free energy decreasing path between transformation phases would necessarily show a hysteretic behavior. The second condition is $\lambda_2 = 1$, where $\lambda_1 \leq \lambda_2 \leq \lambda_3$ are the ordered eigenvalues of $\mathbf{U}$. Eigenvalues represent the amount of elongation or contraction of the austenite lattice along the principal directions. $\lambda_2 = 1$ represents the presence of an invariant plane between austenite and martensite, which is a perfectly coherent interface. This means that austenite is directly compatible with a single variant of martensite, which seldom occurs in SMAs. For an SMA which does not satisfy the $\lambda_2 = 1$ requirement, the interface is usually comprised of alternating layers of martensite variants meeting a homogenous austenite region (Figure 2.1). Due to the incompatibility between the phases, there is both elastic and interfacial energy stored. This stored energy manifests itself as a barrier

against transformation which must be overcome by overheating-undercooling or by additional stress. Thermal hysteresis is caused by the dissipation of this stored energy due to lattice friction and generation of defects to accommodate transformation shear and volume change. In the case of full compatibility, there is no need for the elastic transition layer or the interfacial energy on the twin boundaries, which leads to the minimization of hysteresis.

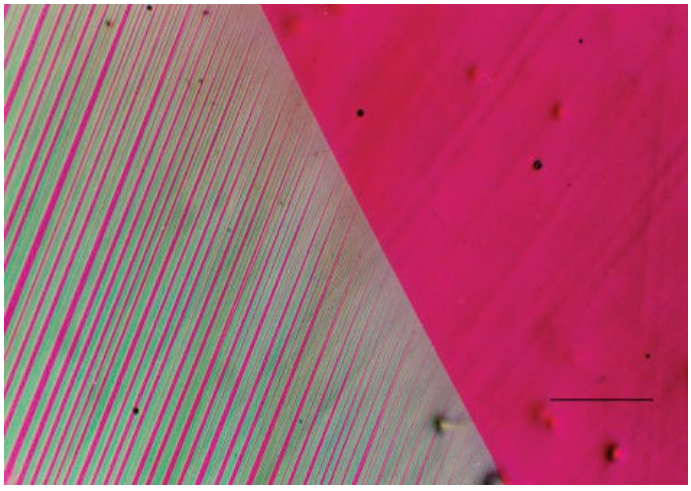

Figure 2.1 Austenite/martensite interface during martensitic transformation in CuAlNi SMA [81].

The form of the stretch matrix **U** can be derived if lattice parameters of both the austenite and the martensite phases and their symmetries are known. For example, there are six martensitic variants for a cubic-to-orthorhombic transformation [86]. The transformation stretch matrix for one of the variants can be described as U_1:

$$\mathbf{U_1} = \begin{pmatrix} \beta & 0 & 0 \\ 0 & \frac{\alpha-\gamma}{2} & \frac{\alpha+\gamma}{2} \\ 0 & \frac{\alpha+\gamma}{2} & \frac{\alpha-\gamma}{2} \end{pmatrix}$$

where $\beta=a/a_0$, $\alpha=b/\sqrt{2}a_0$, $\gamma= c/\sqrt{2}a_0$, a_0 is the lattice parameter of the cubic unit cell and a,b and c are the lattice parameters of the orthorhombic unit cell. The other five transformation stretch matrices have identical components and will yield the same eigenvalues.

Cui *et al.* [81] have investigated the validity of both det**U**=1 and $\lambda_2 = 1$ for the minimization of thermal hysteresis in $Ti_{50}Ni_{50-x}Cu_x$ alloy system over a broad range of compositions using combinatorial synthesis methods. They reported a weak correlation between the volume change during transformation and the thermal hysteresis. Alloys with det**U** values close to 1 exhibited either very large or very small hysteresis values. On the other hand, a strong correlation was found between λ_2 and the thermal hysteresis. Hysteresis values showed a decreasing trend as λ_2 got closer to 1. Stress and thermal hysteresis of 100 MPa and 20 °C were reported, respectively for $Ti_{49.5}Ni_{40.5}Cu_9$ which had $\lambda_2 = 0.9986$ and det**U** = 1.0002.

Delville *et al.* [87] conducted a similar study on the $Ti_{50}Ni_{50-x}Pd_x$ HTSMA system. In addition to displaying the same decreasing hysteresis trend as λ_2 got closer to 1, they also explained the underlying mechanisms of the reduction in hysteresis by investigating the evolution of the microstructure as the composition was systematically tuned. According to their results, as λ_2 approached 1, the fully twinned martensite plates

in the microstructure were replaced by twinless martensite plates, which resulted in a decrease in overall interfacial energy and an increase in compatibility. $Ti_{50}Ni_{39}Pd_{11}$ was found to have a λ_2=1.0001 and thermal hysteresis of 13 °C.

In a recent study by Zarnetta *et al.* [88], the compatibility levels of TiNiCu SMA were further increased through quaternary alloying with different amounts of Pd additions. The quaternary alloys, which had λ_2 values close to 1, were shown to exhibit very small thermal hysteresis values and exceptional stability of transformation temperatures during stress-free thermal cycling.

It has been long known that the M_s temperature of TiNi SMAs is strongly dependent on Ni concentration on the Ni-rich side of stoichiometry [1]. Frenzel *et al.* [89] have shown that increasing Ni content does not only affect the transformation temperatures of TiNi based SMAs but also the width of the thermal hysteresis and the transformation heats during stress-free thermal cycling. Increasing Ni contents were shown to result in a better crystallographic compatibility (λ_2 values closer to 1) and thus lower hysteresis widths.

All of the aforementioned studies correlated the compatibility in an SMA with the thermal hysteresis and stability under stress-free conditions. The functional stability of SMAs during thermal cycling under stress is equally important, especially for actuator applications. Thus, it is of interest to know if the compatibility has a similar influence on the shape memory behavior during repeated actuation cycles. This issue was recently addressed by Grossmann *et al.* [33], who studied the effects of cold-working and ternary alloying with Cu on the thermomechanical cyclic stability of TiNi spring actuators.

Addition of Cu reduced the width of the thermal hysteresis and improved the functional stability by resulting in a better crystallographic compatibility between the transforming phases. Unlike cold-working, the improvement in the functional stability with Cu addition (up to 10 at. %) was achieved without a compromise in the actuator stroke.

2.3 Two-Way Shape Memory Effect in High-Temperature Shape Memory Alloys

While there are several studies on the TWSME characterization of conventional TiNi and Cu-based SMAs, there are limited studies on the TWSME characterization of HTSMAs. The only study on the characterization of TWSME in an HTSMA was conducted by Meng *et al.* [65]. In this study, $Ni_{49}Ti_{36}Hf_{15}$ plates were trained via bending in martensite followed by unconstrained recovery for up to 30 cycles at different temperatures. The highest two-way shape memory (TWSM) strain of 0.88 % was achieved after a bending strain deformation of 7.1 % at room temperature. However, the stability of the TWSME was found to be poor due to the low strength of the martensite, which eased the introduction of dislocations during the TWSME cycles, relaxing the oriented stress fields. The TWSM strain decreased by almost 50 % in only 10 stress-free thermal cycles.

2.3.1 Origin of TWSME

Two mechanisms have been proposed in the literature as the mechanisms responsible for TWSME. The first mechanism attributes the TWSME to the oriented residual stress fields of the dislocation arrays generated during thermomechanical

training [34]. These residual stress fields are able to induce the same variants of martensite under no stress as the ones which are generated by the external training stress, thus causing the TWSME [28]. The magnitude and stability of the TWSME depends to a great extent on the magnitude of these stress fields and how they can be maintained through repeated thermal cycling. The same mechanism has also been explained from a thermodynamics point of view [37]. According to [37] , the dislocation arrays generated during thermomechanical training create low energy configurations in the repeatedly induced martensite variants, while a relatively higher energy configuration is induced in the less frequently induced variants. As a result, the growth of martensite variants with the low energy configuration is favored under no external stress, causing the TWSME.

The second mechanism is based on the local stabilization of martensite, retained above the A_f temperature. Similar to the residual stress fields in the first mechanism, retained martensite plates influence the growth and positioning of other variants, resulting in TWSME [34]. However, this mechanism has grown out of favor [36].

Common to these two mechanisms is the prerequisite for some amount of irreversible strain that should be imposed to the material during training cycles for the manifestation of the TWSME [34]. Thus, the approach for obtaining maximum TWSM strain is to induce enough plasticity that will yield the highest magnitude of oriented stress fields [49]. However, it has also been shown that irreversible strain in the form of true plastic deformation and retained martensite have undesirable effects on the TWSME [36].

2.3.2 Thermomechanical Training Procedures to Obtain TWSME

Different training techniques have successfully been implemented to obtain TWSME. The most common training techniques used so far are: deformation in martensite followed by constrained or unconstrained recovery (OWSME cycling) [45, 47, 58, 61, 63, 65]; stress cycling above the A_f temperature (pseudoelastic cycling) [34]; temperature cycling through the martensitic transformation under a constant stress level (thermal cycling) [28, 35, 36, 44-46, 48, 49, 53, 57] or a combination of the latter two methods [50]. Common to all these techniques is the repeated growth and shrinkage of particular martensitic variants, which is responsible for the generation of favorable dislocation arrays and defects. Another technique which is different in principle than the aforementioned techniques is aging heat treatment under constraint. This method has been used to obtain TWSME in Ni-rich TiNi SMAs. With this method, coherent precipitates are formed in preferred orientations under applied stress, resulting in oriented internal stress biasing the formation of single-variant martensite [51].

Among the training procedures mentioned above, thermal cycling through the martensitic transformation under a constant stress level has been shown to yield satisfactory results in terms of the magnitude and stability of the TWSME [28]. This method has been proven to be an efficient procedure, involving relatively low training stresses and generating a low amount of true plastic deformation compared to other training procedures. The high temperature shape at the end of training is close to the initial shape which is important for applications and design.

2.3.3 Work Output of the TWSME

TWSME has been considered as an unstable effect, which could easily be suppressed by applying an opposing force during transformation, thus having no capability of performing work [90]. However, Stalmans *et al.* [37] demonstrated that in a well-trained CuZnAl SMA, the TWSME was actually capable of resisting a significant amount of force. The TWSME was capable of performing 0.025 J/g of work and 52 MPa was required to suppress it completely. Fukuda *et al.* [91] investigated the work output of the TWSME in a $Ti_{49}Ni_{51}$ (at. %) SMA. The TWSME was induced by aging heat treatment under stress, which led to the formation of aligned Ni_4Ti_3 precipitates relative to the applied stress. The transformation took place under the influence of the coherency stress fields of these precipitates, resulting in specific martensitic variant selection and thus, shape change under no external stress. The aged specimens could perform around 0.040 J/g of work under opposing stress levels of 50 to 100 MPa. In addition, no deterioration was seen in the work output levels during repeated actuation up to 100 thermomechanical cycles.

CHAPTER III

EXPERIMENTAL METHODS

The aim of this chapter is to present details on the fabrication and processing of the materials as well as several thermomechanical testing and characterization methods used throughout the study.

3.1 Materials Fabrication

Ingots of different compositions were prepared by vacuum induction melting of high purity elemental constituents (99.98 wt. % Ni, 99.95 wt. % Ti, 99.995 wt. % Pd, 99.995 wt. %Pt and 99.95 wt. % Sc) using a graphite crucible. The induction unit was equipped with tilt-pour capability and the melts were cast into a copper chill mold, resulting in 25.4 mm diameter by 102 mm long cylindrical ingots. Each ingot was homogenized in a vacuum furnace at 1050 °C for 72 hours and allowed to furnace cool.

3.2 Thermomechanical Processing

Following the homogenization process, ingots were placed into mild steel extrusion cans and extruded at 900 °C with an area reduction ratio of 7:1. The extrusion can was used to prevent oxidation during the extrusion process and to reduce the friction between the extrusion die and the billet. For ECAE processing, 3” long samples were cut from these billets (so-called as-received billets) and encapsulated in square AISI 316

stainless steel cans to conform to the shape of the existing ECAE die. The ECAE die and thus, the stainless steel cans had a cross-section of 19.05 mm x 19.05 mm.

3.2.1 Equal Channel Angular Extrusion (ECAE) Processing

ECAE is an SPD process where the sample is pressed through a die in which two channels of equal cross section intersect at an angle of usually 90° [92] (Figure 3.1). Large amounts of strain can be imposed on the sample without a change in its cross section unlike in traditional metal forming processes such as rolling, forging and conventional area-reduction extrusion. Since the cross-section of the sample does not change after a single pass extrusion, the extruded sample can be reinserted into the die and reprocessed to achieve even more plastic strain. For instance, it is possible with a 4-pass ECAE to obtain an equivalent strain level of 99 % thickness reduction in cold-rolling [93]. ECAE processing followed by recovery and annealing can be used to obtain structures with sub-micron grain size, which show superior physical and mechanical properties [94, 95]. There is a considerable amount of work on the SPD of TiNi SMAs showing the effectiveness of ECAE on improving the shape memory behavior [66, 69, 79, 96-102]. The processed materials display better functional stability under cyclic loading due to increased resistance to slip and other defect formation mechanisms. An alternative SPD method used to enhance the shape memory properties of TiNi SMAs is the high pressure torsion (HPT), where nanocrystalline structures can be obtained after proper annealing of the processed samples [70, 99, 103, 104]. The advantages of ECAE over HPT are that there is no sample size limitation with ECAE and it is possible to

apply large uniform strains on bulk samples. In addition, better control on the final texture and microstructure of the product can be achieved through different extrusion routes in ECAE [92].

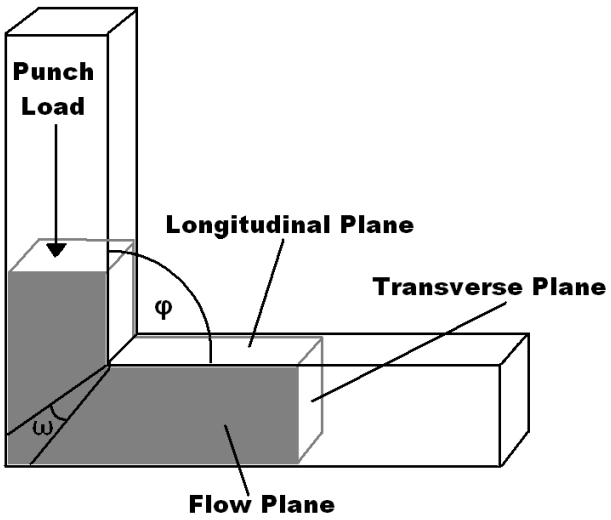

Figure 3.1 A schematic of the ECAE process showing different planes on the extruded billet.

Throughout this study, several ECAE processes were performed on $Ti_{50.5}Ni_{24.5}Pd_{25}$ and its quaternaries with Sc addition. Following ECAE, post-deformation annealing treatments were applied to selected samples to relieve internal stresses and recover some of the dislocation substructure. From our previous experience with the extrusion of TiNi [66] and TiNiPd SMAs [105], the thermomechanical behavior of the final product depends on the process variables such as extrusion rate, strain rotation

(processing route), processing temperature, number of passes and canning material. Table 3.1 lists the extrusions performed on the ternary and quaternary alloys to date.

Table 3.1 A summary of the ECAE processes conducted within the scope of this study.

Material	Processing Temperature (°C)	Processing Route	Post-processing treatment	Result
$Ti_{50.5}Ni_{24.5}Pd_{25}$	425	$4B_c$		Success
$Ti_{50.5}Ni_{24.5}Pd_{25}$	425	4E	Low-T Anneal	Success
$Ti_{49.5}Ni_{25}Pd_{25}Sc_{0.5}$	425	$4B_c$		Success
$Ti_{49.5}Ni_{25}Pd_{25}Sc_{0.5}$	425	4E	Low-T Anneal	Success
$Ti_{50}Ni_{24.5}Pd_{25}Sc_{0.5}$	425	$4B_c$		Failure
$Ti_{50}Ni_{24.5}Pd_{25}Sc_{0.5}$	425	4E		Success

ECAE was performed isothermally at 425 °C for 4 passes using route B_c or E at a rate of 0.127 mm/sec. 425 °C was the lowest processing temperature that gave a good level of microstructural refinement while minimizing recovery and recrystallization. Trials at lower processing temperatures were not successful due to the intense shear localization before the completion of 4 passes. Immediately after each pass, the billet was quenched in water to preserve the ECAE microstructure. Before each subsequent pass, the billet was held in the die for 15 minutes at extrusion temperature. Route B_c was selected as one of the processing routes, since it was shown to be the most effective

route for grain refinement [106]. It involves the rotation of the billet 90° after each pass. Route E was also preferred as a processing route since it required less punch pressure during extrusion as compared to other routes. In terms of the processing schedule, route E involves the rotation of the billet by 180° around the extrusion direction after the first pass, 90° after the second pass, and 180° again before the last pass. Our previous experience with equiatomic TiNi [66] and TiNiPd, with lower Pd contents than the current alloy [75], showed that route E yielded the best results in terms of shape memory characteristics. Furthermore, route E was shown to be the most effective route for achieving uniform, equiaxed, ultra-fine grain structure along with route B_c, but the uniformly deformed region in route E processed samples is significantly larger as compared to that of samples processed with route B_c [107]. In terms of the processing schedule, route E represents a hybrid pattern between route C and B, the sample being rotated 180° around the extrusion direction after the first pass, 90° after the second pass and 180° again before the last pass. Further information about the ECAE processing routes as well as the other fundamental parameters like shearing patterns and imposed strains can be found in [92].

3.3 Microstructural Characterization

3.3.1 Crystal Structures

Crystal structures of the transforming phases in as-received materials were determined using a Bruker-AXS D8 X-ray diffractometer with CuK_α (1.5406 Å) radiation. The X-ray diffraction (XRD) patterns of the specimens were measured in the

2θ range of 20-80° both in the martensite and austenite phases. Measurements in the austenite phase were performed in vacuum using a Pt heating-strip with an x-ray transparent beryllium dome. Heating and cooling of the samples was achieved at a rate of 30 °C/min. For the calculations of crystallographic compatibility between transforming phases, i.e. λ_2, the lattice parameters of martensite and austenite phases were measured at M_f – 30 °C and A_f + 30 °C, respectively, in order to achieve thermodynamically equivalent conditions for all materials. Before the start of the analyses, specimens were kept at the aforementioned temperatures for 15 minutes to ensure a homogeneous temperature distribution.

3.3.2 Microstructure and Compositional Analysis

Microstructural and chemical analyses were carried out on a Cameca SX50 (Gennevilliers Cedex, France) scanning electron microscope (SEM) equipped with four wavelength dispersive X-ray spectrometers (WDS) and an energy dispersive X-ray spectrometer (EDS) using standard microprobe imaging and microanalytical methods. As an alternative method to WDS, bulk compositional analyses were also conducted using inductively coupled plasma - atomic emission spectroscopy (ICP-AES) to assess the validity of the results. Electron imaging was performed using a six component backscattered electron (BSE) detector. X-ray elemental distribution images were acquired by scanning the beam in a 512 by 256 grid; dwell time at each step (pixel) was 6 ms. Each of the four WDS spectrometers was set to the major X-ray emission line of

an element. The brightness of each pixel in the image was proportional to the number of X-rays from that element detected at that point on the sample.

Transmission electron microscopy (TEM) studies were conducted using JEOL 2010 and Philips CM200 microscopes operated at an accelerating voltage of 200kV. For the ECAE processed samples, TEM images were taken from the flow plane which is parallel to the side face of the ECAE processed billet (Figure 3.1). TEM foils were prepared by mechanically grinding samples to 100μm, followed by punching out 3mm diameter disks from the thin foils. The disks were subsequently polished using a twin-jet electropolisher with a 20 vol. % H_2SO_4 and 80 vol. % methanol solution at -10 °C. The TEM was equipped with an in-situ heating stage for observation of the austenite microstructure.

3.3.3 Microhardness

Microhardness samples were extracted from both the as-received and ECAE processed billets (see the figure on p. 37). The transverse plane of the ECAE processed billets was used for the extraction of samples. ECAE processed samples were subsequently heat treated at various temperatures for 1 hour followed by a water quench. Room temperature Vickers microhardness values were determined using a Buehler Omnimet (Lake Bluff, IL) microhardness tester. Hardness values were recorded using 300 g load (i.e. $HV_{0.300}$) and a loading time of 15 s. While low temperature heat treatments (<400 °C) were conducted in air, higher temperature heat treatments were performed under a vacuum of 10^{-6} Pa. Heat treatment at 300 °C was selected as the

condition for further microstructural and thermomechanical investigations. Samples of this condition are referred to as "post-ECAE annealed" samples throughout the dissertation.

3.4 Calorimetry

Stress-free phase transformation temperatures (martensite finish, M_f; martensite start, M_s; austenite start, A_s; and austenite finish, A_f) were measured using a Perkin-Elmer Pyris I differential scanning calorimeter (DSC) at a heating-cooling rate of 10 °C min^{-1}. Sample preparation greatly affects the measured transformation temperatures due to residual stresses that can develop depending on how the samples are prepared. Thus, all DSC specimens were prepared as 5 mm x 1 mm discs using wire electrical discharge machining (EDM), which is a non-contact, stress-free machining technique. Transformation temperatures were determined from the DSC peaks using the slope line extension method [108]. The net amount of heat released during phase transformation (ΔH_{net}) was also calculated from the area under the transformation peaks. Specimens of different compositions were thermally cycled five times to assess the cyclic stability of the transformation temperatures.

3.5 Thermomechanical Characterization

Small dog-bone shaped tension specimens with gage dimensions of 8 mm x 3 mm x 1.5 mm and compression specimens of 4 mm x 4 mm x 8 mm were cut from the as-received and ECAE processed billets using wire EDM (Figure 3.2). Short-duration

thermomechanical experiments such as isobaric cooling-heating tests, thermal cyclic tests under constant stress consisting of relatively small number of cycles and isothermal monotonic loading tests were performed on a servo-hydraulic MTS test frame. For tensile tests, the axial strain was measured using an MTS high-temperature extensometer, which had a pair of ceramic rods, 3.5 mm in diameter with V-chisel ends exerting a 300 g force per rod on the sample. The extensometer had a gage length of 12.7 mm and a range of ± 20%, which means that the maximum extension and compression levels were ± 2.54 mm. Since the gage length of the tension specimens were only 8 mm, the extensometer had to be attached to the specimens in its fully compressed form, measuring an actual gage length of 10.5 mm. Therefore, the measured strain values were recalculated according to the gage length of the tension specimen (8mm) assuming that the inelastic deformation occurs only in the gage section. Obviously, this approach does not result in 100% accurate results in terms of strain levels but it should be very close to reality and the measurements are much more accurate than strains calculated using the crosshead displacement of the MTS test frame.

Prior to mechanical testing, one side of each sample was polished to remove the residual EDM layer. The polished side of the samples was used for thermocouple attachment, while the extensometer was placed on the other side. For compression tests, a miniature MTS extensometer with 3 mm gage length was used. Samples were heated through conduction from the grips with heating bands. Cooling of the samples was achieved again by conduction through flowing liquid nitrogen in copper tubes wrapped around the grips. The rate of heating and cooling during mechanical testing was 10 ± 2

°Cmin^{-1}. The temperature was measured using a K-type thermocouple, directly attached to the gage section of the sample.

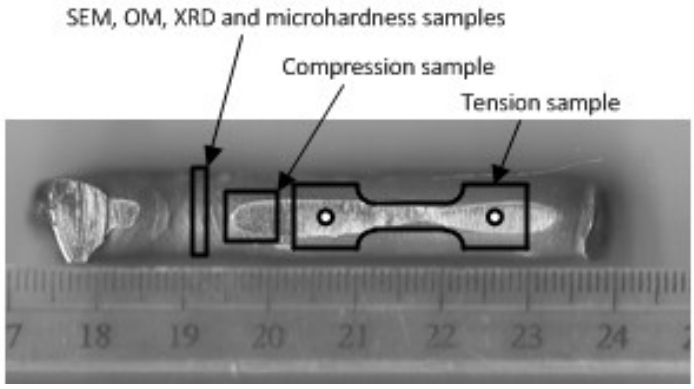

Figure 3.2 A schematic showing how several different samples for microstructural and thermomechanical characterization were extracted from ECAE processed (and as-received) billets. The visible surface of the ECAE processed billet is the longitudinal plane and the horizontal direction is the extrusion direction.

Thermal cycling tests involving relatively higher number of cycles (thermomechanical training tests) were conducted on a custom-built constant-stress testing frame, which did not rely on liquid nitrogen as the cooling agent. On this test setup, heating and cooling was achieved at a rate of 5 ± 1 °C/min. Samples were heated by conduction from the grips which were in turn heated by radiation through the use of an environmental furnace equipped with four 1kW halogen lamps. For cooling, water was circulated around the grips flowing through copper tubing. Temperature was controlled with a K-Type thermocouple attached to the middle of the sample gage section with a copper wire. To minimize the radiation heat transfer on the sample surface

(which will lead to erroneous temperature readings that are not representative of the bulk of the specimen), the sample was shielded with a 1 mm thick reflective aluminum foil. A capacitive displacement probe (Capacitec® HPC-75) with a linear range of 0-1.5 mm was attached to the grips to measure the displacements during the training process. Axial strain was calculated by dividing the change in length to the initial gage length.

3.5.1 Isobaric Cooling-Heating Experiments

The principal anticipated application for most HTSMAs, including those in this investigation, is in the field of actuation. Consequently, one of the main focuses should be on the thermomechanical response of these alloys under the loading conditions that real actuators would experience. In this study, the primary thermo-mechanical characterization technique that was utilized consisted of a series of isobaric cooling-heating experiments to characterize the transformation behavior of the materials, including the evolution of transformation temperatures, recovered transformation strain (ε_{rec}), irrecoverable strain (ε_{irr}), and thermal hysteresis as a function of externally applied stress. In these experiments, the specimen is incrementally loaded to predefined stress levels (i.e., 50,100,150, ... MPa) starting from the lowest stress and working up. At each stress level, the sample is thermally cycled through full transformation between a temperature below M_f^σ and a temperature above A_f^σ (where M_f^σ and A_f^σ are the respective transformation temperatures under stress) while the strain response is recorded as a function of temperature. Load changes take place at the upper temperature

limit of the thermal cycle when the sample is completely austenite and then the sample is cooled under the new load level and reheated.

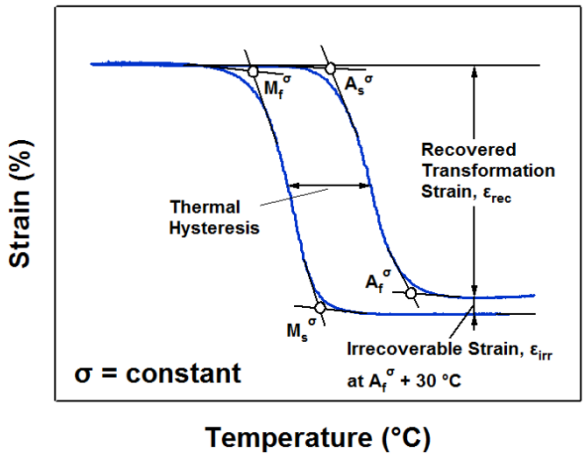

Figure 3.3 A schematic illustration showing the determination of thermal hysteresis, recovered transformation strain (ε_{rec}), irrecoverable strain (ε_{irr}) and transformation temperatures from a constant-stress thermal cycle.

Figure 3.3 shows how the relevant shape memory characteristics are determined from a single thermomechanical cycle. ε_{rec} was measured as the strain recovered during the reverse transformation, which is also a measure of actuation strain. ε_{irr} was defined as the amount of open-loop strain at the end of each cycle measured at $A_f^\sigma + 30^\circ C$. Thermal hysteresis was defined as the width of the strain-temperature curve measured at half the reverse transformation strain. Transformation temperatures M_f^σ, M_s^σ, A_s^σ and

A_f^{σ} were determined in a similar fashion to the slope line extension method used in [108].

3.5.2 Thermal Cycling Experiments under Constant Stress

The objective of thermomechanical training experiments was to investigate the evolution of the shape memory response under a constant stress level. Experiments consisting of 10 thermal cycles were performed for a quick assessment of the evolutionary behavior during the first few cycles. Experiments with 100 thermal cycles were primarily aimed at investigating the response of the material during the course of achieving stable shape memory behavior and secondarily observe the concomitant TWSME effect. These high-cycle experiments will also be called thermomechanical training experiments throughout the study.

Similar to the isobaric cooling-heating tests, transformation temperatures, ε_{rec}, ε_{irr} and thermal hysteresis values were calculated for each thermal cycle (Figure 3.1) and were plotted as a function of cycle number.

3.5.3 Isothermal Monotonic Loading Tests

In addition to the thermomechanical tests described in the previous two sections, isothermal monotonic loading experiments were conducted to assess the strength levels of materials. Critical parameters such as σ_{SIM}, the critical stress to induce martensite, and σ_y^M, the yield strength of the stress-induced martensite, were extracted from these experiments. Since some of the samples experienced premature failure under tension

before reaching the plastic deformation of martensite and therefore not allowing for the detection of σ_y^M, these experiments were mainly conducted under compression.

The compression samples were initially heated above their A_f temperatures to ensure a completely austenitic structure. They were then cooled to a temperature of M_s + 15 °C while still in austenite and subsequently loaded at a strain rate of -10^{-4} sec^{-1}. The selection of the testing temperature with respect to the M_s temperature as opposed to testing at a fixed temperature was to ensure equal thermodynamic conditions for all materials investigated.

CHAPTER IV

EFFECTS OF SC ADDITIONS ON THE SHAPE MEMORY CHARACTERISTICS OF $Ti_{50.5}Ni_{24.5}Pd_{25}$*

This chapter investigates the effects of different amounts of scandium (Sc) additions on the shape memory behavior, in particular, the functional stability, of $Ti_{50.5}Ni_{24.5}Pd_{25}$ (at. %). The research started with the characterization of the ternary $Ti_{50.5}Ni_{24.5}Pd_{25}$ and its quaternary with 0.5 at. % Sc addition. After initial microstructural and thermomechanical characterization studies were conducted and a solid knowledge base was established on the quaternary alloy, addition of 3 at. % Sc was attempted.

0.5 at. % Sc addition proved to be useful in enhancing the functional stability of $Ti_{50.5}Ni_{24.5}Pd_{25}$. The improvements came in the form of smaller thermal hysteresis, smaller irrecoverable strains and smaller shifts in transformation temperatures during both stress-free and isobaric thermal cycling. Larger additions of Sc further improved the functional stability of $Ti_{50.5}Ni_{24.5}Pd_{25}$, however, severely depressed its transformation temperatures (140 °C drop in M_s with 3 at. % addition), making it no longer qualify as an HTSMA. As a result, most of the characterization and the processing work focused on the 0.5 at. % Sc microalloyed $Ti_{50.5}Ni_{24.5}Pd_{25}$ HTSMA.

---

* Reprinted with permission from "Improvement in the shape memory response of $Ti_{50.5}Ni_{24.5}Pd_{25}$ high-temperature shape memory alloy with scandium microalloying" by Atli KC, Karaman I, Noebe RD, Garg A, Chumlyakov Y, Kireeva I, 2010. Metallurgical and Materials Transactions A, 41, pp. 2485-2497, Copyright 2010 by The Minerals, Metals & Materials Society and ASM International.

4.1 Sc as the Choice of Quaternary Alloying Addition

The selection of Sc as a quaternary alloying addition to $Ti_{50.5}Ni_{24.5}Pd_{25}$ is due to multiple reasons:

1. Sc is expected to have a strong site preference for Ti (similar to Hf and Zr). However, unlike Hf and Zr, it is expected to have a wide range of solubility in TiNi because it also forms B2 compounds with Ni. Therefore, a wide range of Sc solubility is expected in TiNiPd without second-phase formation.

2. According to currently unpublished atomistic simulations for quaternary additions to TiNiPd by Bozzolo, performed in a similar manner to the ternary additions studied by Bozzolo *et al.* in TiNi [109] and TiPd and TiPt [110], Sc was found to have a significant effect on the formation energy of TiNiPd, increasing the formation energy for a given unit of alloying addition more than any other element studied. Therefore, it can be inferred that Sc affects the bond strength in the alloy, which may affect both the transformation and slip behavior.

3. In the same unpublished study by Bozzolo, Sc was found to have a moderate effect on the lattice strain in B2-TiNiPd as determined by its influence on lattice parameters. Thus, it should have potent solid-solution strengthening effects.

4.2 Initial Alloying Trials with 0.5 at. % Sc Addition

4.2.1 Microstructure

For the $Ti_{50}Ni_{50-x}Pd_x$ (at. %) system, when $x \geq 10$, the martensitic transformation occurs between the B2 (cubic) high temperature austenite and B19 (orthorhombic) low

temperature martensite phases [111-114]. Figure 4.1a is a comparison of the XRD spectra at room temperature for $Ti_{50.5}Ni_{24.5}Pd_{25}$ and $Ti_{50}Ni_{24.5}Pd_{25}Sc_{0.5}$, which confirms the B19 structure of the martensite for both alloys. Figure 4.1b shows the XRD spectra at 225 °C which is above the A_f temperature of both alloys. The structure of austenite for both alloys was confirmed to be B2. The small Sc addition did not change the structure of either the martensite or austenite.

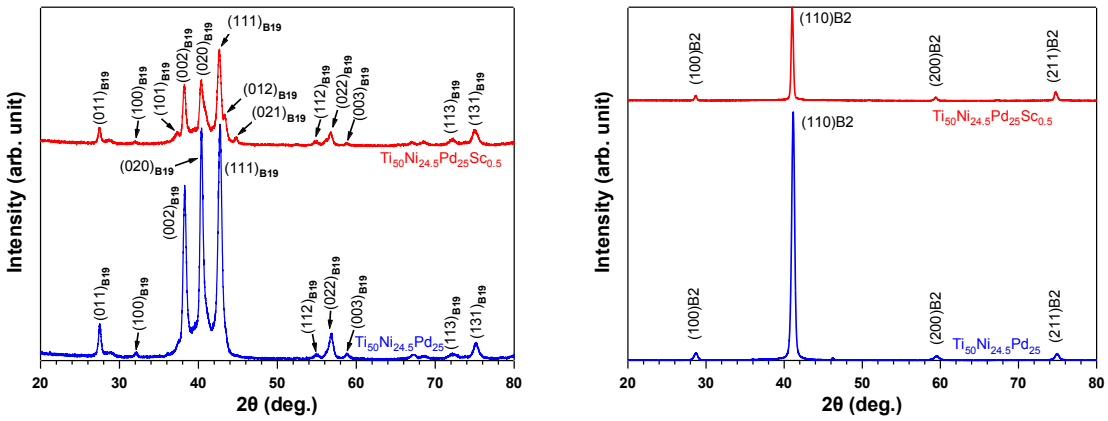

Figure 4.1 A comparison of the XRD spectra for $Ti_{50.5}Ni_{24.5}Pd_{25}$ and $Ti_{50}Ni_{24.5}Pd_{25}Sc_{0.5}$ alloys. (a) At room temperature (below M_f) XRD patterns show that both materials have a B19 orthorhombic martensite structure and (b) at 225 °C (above A_f) both materials exhibit a B2 crystal structure.

Lattice parameters were calculated from the observed peaks and are listed in Table 4.1. Microalloying $Ti_{50.5}Ni_{24.5}Pd_{25}$ with Sc slightly increased the lattice parameters, as expected from the atomistic simulations. The volume of the B2 austenite

phase increased by 0.6 %, while the volume of the B19 martensite phase increased by 0.5 % due to the Sc addition.

Table 4.1 Lattice parameters of $Ti_{50.5}Ni_{24.5}Pd_{25}$ before and after microalloying with 0.5 at. % Sc. Errors reported are the standard deviations of the measurements taken.

Lattice Parameters	**$Ti_{50.5}Ni_{24.5}Pd_{25}$ (Å)**	**$Ti_{50}Ni_{24.5}Pd_{25}Sc_{0.5}$ (Å)**
a_0 (B2)	3.102 ± 0.002	3.108 ± 0.001
a (B19)	2.788 ± 0.001	2.796 ± 0.001
b (B19)	4.462 ± 0.001	4.465 ± 0.001
c (B19)	4.700 ± 0.001	4.706 ± 0.001

From the lattice parameters in Table 4.1, λ_2 for $Ti_{50.5}Ni_{24.5}Pd_{25}$ was calculated as 1.0171, while for $Ti_{50}Ni_{24.5}Pd_{25}Sc_{0.5}$, λ_2 was 1.0158. Both values are very similar and resulted in alloys with low thermal hysteresis around 15°C, as further mentioned in Section 4.2.2. However, at some larger Sc addition it may be possible to drive the value of λ_2 closer to 1 and produce an alloy with even smaller thermal hysteresis.

Grain sizes were relatively smaller in the quaternary alloy, ranging from 5 μm to 10 μm with an average size of 7 μm, while for the ternary alloy the range was 5 μm to 15 μm with an average of 10 μm. Scanning electron micrographs of both materials in back-scattered electron mode revealed a martensitic structure with a fine precipitate distribution. For $Ti_{50.5}Ni_{24.5}Pd_{25}$, the average size of the particles was 1.5 ± 0.6 μm,

whereas for $Ti_{50}Ni_{24.5}Pd_{25}Sc_{0.5}$, the average was 0.9 ± 0.4 μm (Figures 4.2a and 4.2b, respectively).

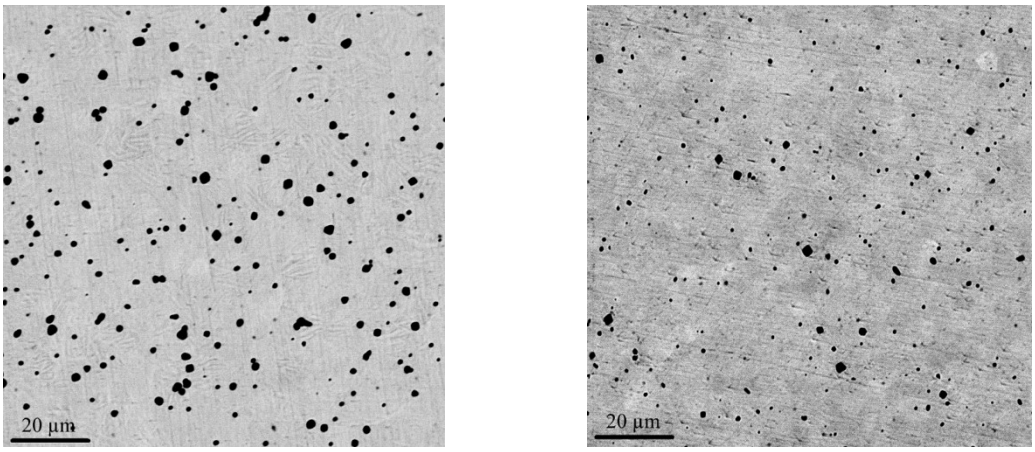

(a) (b)

Figure 4.2 Backscattered electron images of (a) $Ti_{50.5}Ni_{24.5}Pd_{25}$ with predominant Ti(C,O) type precipitates and, (b) $Ti_{50}Ni_{24.5}Pd_{25}Sc_{0.5}$ with relatively finer Ti(C,O) type precipitates.

EDS analysis indicated that these particles were predominantly Ti(C,O). The volume fraction of particles in the ternary alloy was found to be more than twice that in the quaternary alloy: 3.4 % as compared to 1.4 %. This significant difference may have resulted from possible variations in the melting conditions for the two alloys, such as the amount of superheat and time molten before casting, which would affect the amount of carbon pickup from the crucible.

Ti_2(Ni,Pd) type precipitates, which are usually observed in Ti-rich compositions of TiNiPd, were not detected in either material. EDS analyses on relatively small (<1μm) particles, which were suspected to be Ti_2(Ni,Pd), were not conclusive due to the

large errors associated with trying to do EDS on such a small volume because of overwhelming contributions from the matrix. Finally a few Sc_2O_3 type precipitates were observed in the $Ti_{50}Ni_{24.5}Pd_{25}Sc_{0.5}$ alloy as illustrated in x-ray elemental distribution images (Figures 4.3a and 4.3b). The formation of these oxides are a consequence of the strong affinity of Sc for oxygen, similar to the formation of Ti(C,O) during melting.

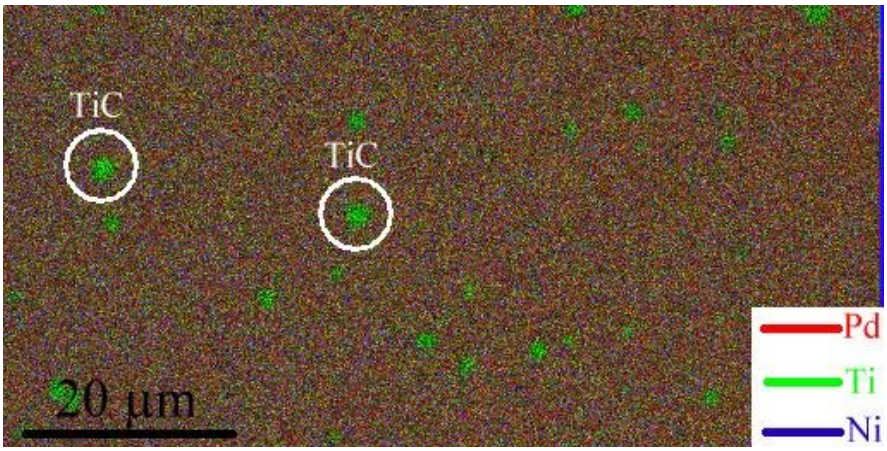

(a)

Figure 4.3 (a) X-ray elemental mapping of $Ti_{50.5}Ni_{24.5}Pd_{25}$. Different colors indicate different constituent elements. Precipitates are predominantly TiC. (b) X-ray elemental distribution image of $Ti_{50}Ni_{24..5}Pd_{25}Sc_{0.5}$. A small percentage of Sc_2O_3 precipitates is present besides the TiC.

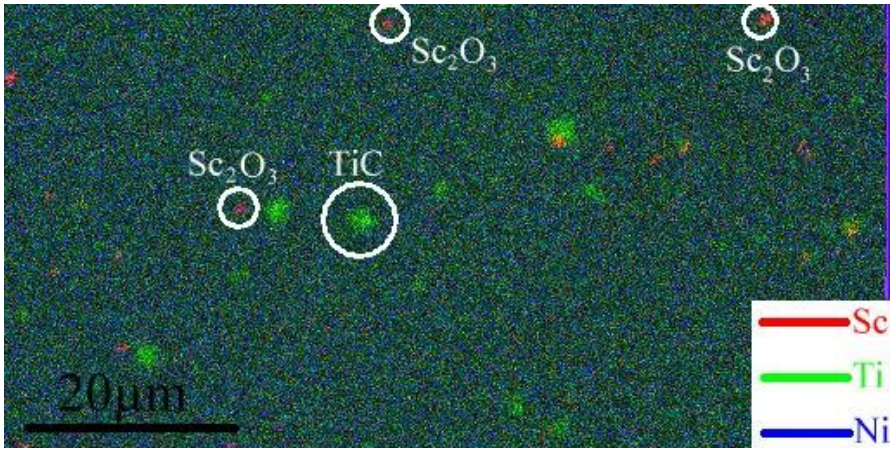

(b)

Figure 4.3 Continued.

WDS analyses were also performed on both samples to quantify the composition of the matrix. A total of 6 measurements were taken at random spots. Table 4.2 lists the averages of these measurements along with the ICP-AES results. The measured values were essentially indistinguishable from the nominal target compositions given the tolerances and uncertainties (±1 % of the absolute level of the element being analyzed) in using WDS and ICP-AES as bulk chemical analysis techniques. The measurement trends were consistent with the fact that Ti values are less than the nominal composition values due to the formation of Ti(C,O) precipitates. Sc levels in the solid solution were found to be comparable with both measurement techniques. Clearly, the drop in transformation temperatures of the $Ti_{50}Ni_{24.5}Pd_{25}Sc_{0.5}$ alloy is due to the addition of 0.5 at. % Sc.

Table 4.2 Compositional analysis results for $Ti_{50.5}Ni_{24.5}Pd_{25}$ and $Ti_{50}Ni_{24.5}Pd_{25}Sc_{0.5}$ as determined using WDS and ICP-AES. Errors reported for the WDS analysis are the standard deviations from the six measurements. ICP-AES errors represent the deviation from the average of two measurements.

	Ti (at. %)	**Ni (at. %)**	**Pd (at. %)**	**Sc (at. %)**
$Ti_{50.5}Ni_{24.5}Pd_{25}$ (WDS)	49.18 ± 0.12	25.07 ± 0.14	25.75 ± 0.09	-
$Ti_{50.5}Ni_{24.5}Pd_{25}$ (ICP-AES)	48.87 ± 0.10	24.32 ± 0.02	25.82 ± 0.12	-
$Ti_{50}Ni_{24.5}Pd_{25}Sc_{0.5}$ (WDS)	49.00 ± 0.11	24.77 ± 0.14	25.75 ± 0.08	0.48 ± 0.01
$Ti_{50}Ni_{24.5}Pd_{25}Sc_{0.5}$ (ICP-AES)	48.65 ± 0.04	24.37± 0.04	25.97± 0.07	0.47± 0.01

Figure 4.4 includes typical bright-field TEM images for the $Ti_{50.5}Ni_{24.5}Pd_{25}$ and $Ti_{50}Ni_{24.5}Pd_{25}Sc_{0.5}$. Corresponding selected area diffraction (SAD) patterns are also shown. Both images show a twinned martensitic structure with {111} type I twins. The SAD pattern for $Ti_{50.5}Ni_{24.5}Pd_{25}$ in Figure 4.5a was recorded in the [110] zone axis and an orthorhombic structure is revealed with the expected 125° angle between the (002) and (1-1-1) reflections. Figure 4.4b shows the martensite variants in $Ti_{50}Ni_{24.5}Pd_{25}Sc_{0.5}$ with fine internal twins. The martensite structure remains orthorhombic after the 0.5 at. % Sc addition, consistent with the XRD analyses. Also, (11-1) type I twins observed from the SAD patterns in Figure 4.4b were predominant in this microstructure.

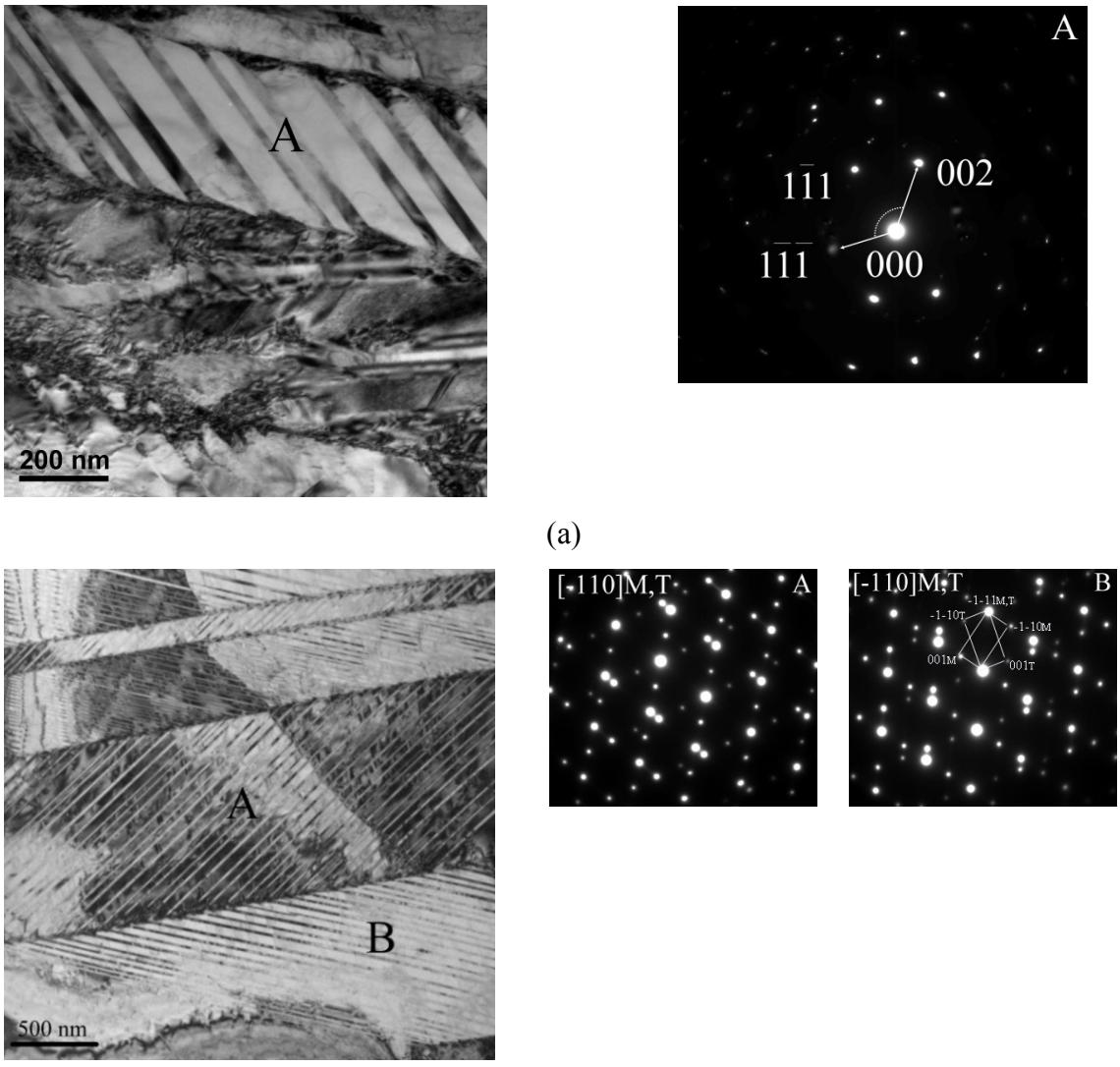

Figure 4.4 Bright field TEM images of (a) $Ti_{50.5}Ni_{24.5}Pd_{25}$ at room temperature together with the electron diffraction pattern taken from region A showing an orthorhombic martensite structure with {111} type I twinning mode, (b) $Ti_{50}Ni_{24.5}Pd_{25}Sc_{0.5}$ at room temperature showing martensite variants with very thin internal twins and corresponding electron diffraction patterns of (11-1) type I twins.

4.2.2 Stress-free Phase Transformation Temperatures

DSC results for the $Ti_{50.5}Ni_{24.5}Pd_{25}$ and $Ti_{50}Ni_{24.5}Pd_{25}Sc_{0.5}$ alloys are shown in Figure 4.5. Five heating and cooling cycles were conducted on each material. Figure 4.5a shows the second DSC cycle for each alloy and illustrates how the stress-free phase transformation temperatures and ΔH_{net} were determined from these curves. The reason why first cycle results were not taken into account is due to the so-called martensite "stabilization effect" [115]. Figures 4.5b and 4.5c demonstrates the evolution of transformation temperatures during thermal cycling for both materials. The first heating cycle usually results in higher reverse transformation temperatures since residual dislocations in the as-extruded material, especially at the martensite and internal twin boundaries, create extra resistance during the reverse transformation. This extra resistance requires overheating of the material to complete the reverse transformation, resulting in an unusually high, first cycle A_s temperature. However, after the first reverse transformation, this "stabilization effect" vanishes [97]. The results of the DSC analyses are summarized in Table 4.3.

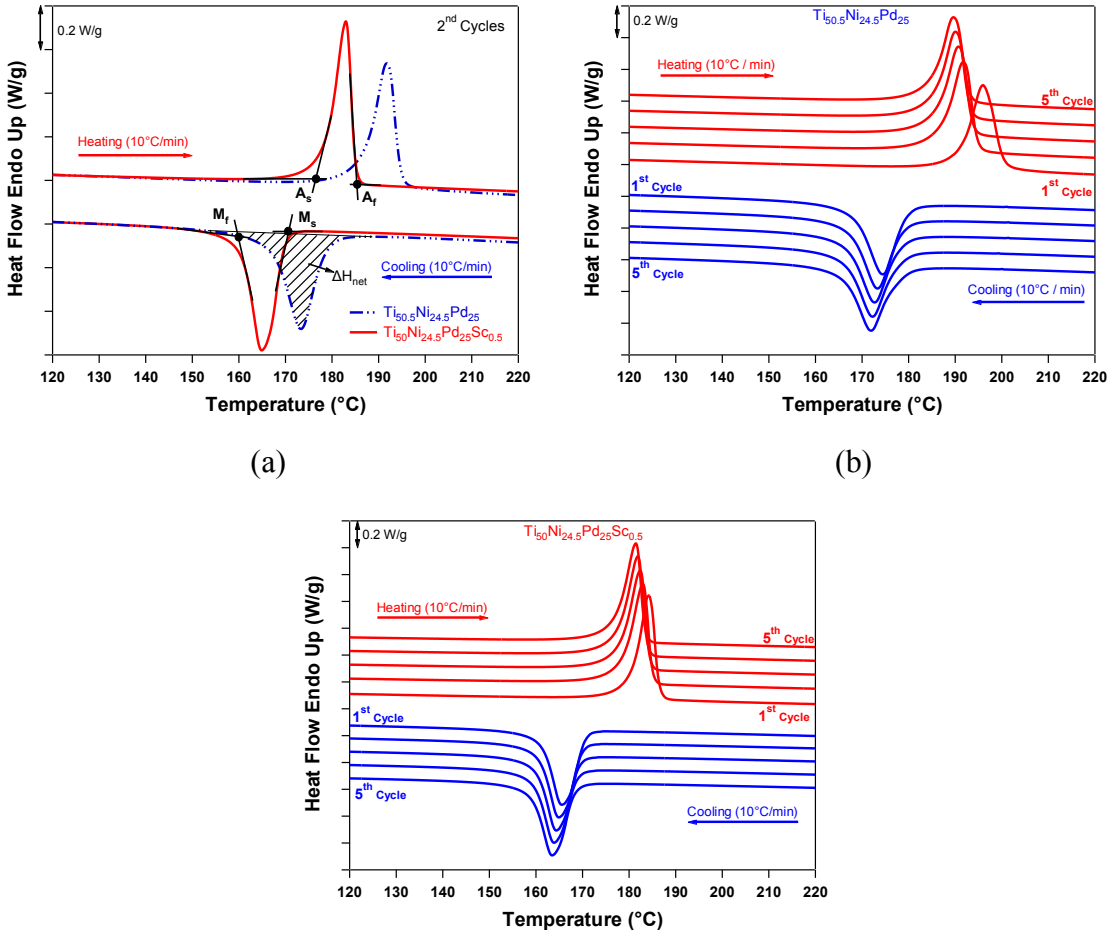

Figure 4.5 (a) Second cycle DSC responses for $Ti_{50.5}Ni_{24.5}Pd_{25}$ and $Ti_{50}Ni_{24.5}Pd_{25}Sc_{0.5}$ indicating how transformation temperatures and ΔH_{net} were determined. Evolution of transformation temperatures during five thermal cycles between 100 °C and 260 °C for (b) $Ti_{50.5}Ni_{24.5}Pd_{25}$ and (c) $Ti_{50}Ni_{24.5}Pd_{25}Sc_{0.5}$.

Both materials exhibited very similar, single stage martensitic transformations with nearly identical thermal hysteresis. According to the second cycle data in Table 4.3, the absolute transformation temperatures for the Sc-doped alloy are 6 - 10 °C lower than the respective transformation temperatures for the ternary $Ti_{50.5}Ni_{24.5}Pd_{25}$ alloy. The

change in transformation temperatures with thermal cycling occurs due to the repetitive motion of the transformation interface and the accommodation of the transformation shape change with dislocations and other defects [2]. For $Ti_{50.5}Ni_{24.5}Pd_{25}$, there is a drop of 2.6 °C in M_s temperature after five thermal cycles, whereas for $Ti_{50}Ni_{24.5}Pd_{25}Sc_{0.5}$, the same value is 2.3 °C. The difference between these values is negligible, especially considering that the uncertainty levels associated with the DSC measurements are ± 0.2 °C. Consequently, the change in transformation temperatures with thermal cycling is basically unaffected by the Sc addition, and overall the change in transformation temperature is relatively small. To put these cyclic changes into perspective, equiatomic hot-rolled TiNi with a similar microstructure to these alloys, exhibits a shift of 9 °C in M_s temperature [66] after five thermal cycles.

Table 4.3 Transformation temperatures, thermal hysteresis, and total amount of heat released during the transformation (ΔH_{net}, observed enthalpy change) for $Ti_{50.5}Ni_{24.5}Pd_{25}$ and $Ti_{50}Ni_{24.5}Pd_{25}Sc_{0.5}$ determined from the DSC results in Figure 4.5c.

Material	M_f (°C)	M_s (°C)	A_s (°C)	A_f (°C)	ΔH_{net} (J/g)	M_s^{5th}-M_s^{1st} (°C)	Thermal Hysteresis (A_f-M_s) (°C)
$Ti_{50.5}Ni_{24.5}Pd_{25}$	166.5	179.4	184.1	195.1	22.4	2.6	15.7
$Ti_{50}Ni_{24.5}Pd_{25}Sc_{0.5}$	160.3	170.1	177.6	185.1	17.9	2.3	15.0

For a thermoelastic martensitic transformation induced by cooling from the parent phase, ΔH_{net} can be approximated as [116]

$$-\Delta H_{net}^{P\to M} = -\Delta H_{ch}^{P\to M} + \Delta H_{el}^{P\to M}$$

where $\Delta H_{ch}^{P\to M}$ is the change in the chemical enthalpy and $\Delta H_{el}^{P\to M}$ is the change in the stored elastic energy. According to the sign convention used in this equation, heat given to the system is positive and work done on the system is negative. The subscript 'net' is used to differentiate between the chemical enthalpy change during forward transformation, ΔH_{ch}, and the total amount of heat released during the transformation, ΔH_{net}. It is known that for multiple-interface and polycrystalline transformations, part of the chemical enthalpy is stored as elastic strain enthalpy [117]. Thus, the area under the transformation peak is not necessarily equal to ΔH_{ch}. In Table 4.3, it is noted that $Ti_{50}Ni_{24.5}Pd_{25}Sc_{0.5}$ has a slightly lower ΔH_{net} (as measured from the area under the cooling curve of the second cycle) as compared to $Ti_{50.5}Ni_{24.5}Pd_{25}$. Increased stored elastic strain energy might be one of the factors that contribute to this behavior, since $Ti_{50}Ni_{24.5}Pd_{25}Sc_{0.5}$ had a smaller grain size.

4.2.3 Isobaric Cooling-Heating Experiments

Figure 4.6 shows the strain vs. temperature response of both $Ti_{50.5}Ni_{24.5}Pd_{25}$ and $Ti_{50}Ni_{24.5}Pd_{25}Sc_{0.5}$ at selected stress levels. ε_{rec} and ε_{irr} levels for both materials, determined from the complete set of strain-temperature curves, as well as thermal hysteresis values as a function of bias stress are presented in Figures 4.7a and 4.7b, respectively. For comparison, the results for a hot-rolled binary near-equiatomic TiNi

alloy, with a similar microstructure to the present alloys, are also included in Figures 4.7a and 4.7b. It should be emphasized that ε_{rec} values as measured from the heating curves do not necessarily reflect the exact level of transformation strain in the material. In addition to macroscopic plasticity, a part of ε_{irr} might also originate from the retained martensite which may require higher levels of overheating to transform back to austenite.

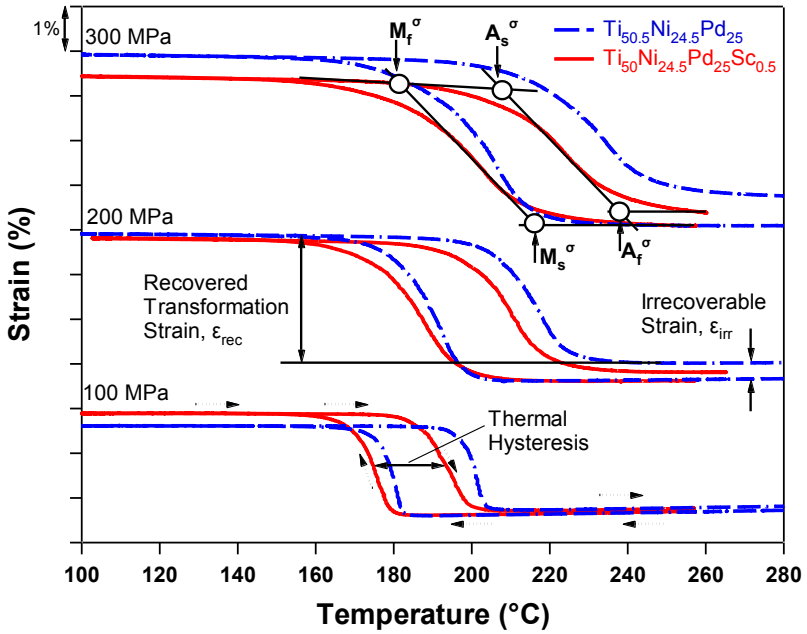

Figure 4.6 Strain vs. temperature responses of $Ti_{50.5}Ni_{24.5}Pd_{25}$ and $Ti_{50}Ni_{24.5}Pd_{25}Sc_{0.5}$ alloys at selected tensile bias stress levels.

4.2.3.1 Effect of Sc Addition on Recovered Transformation Strain and Irrecoverable Strain

During cooling through the forward transformation, the amount of strain generated increases with increasing stress in the present ternary and quaternary HTSMAs indicating the growth of a single or a few preferred variants of martensite favored by the external stress. While almost full recovery of this strain is seen at low stress levels upon heating above the A_f^{σ} temperature, only partial recovery is recorded at high stress levels (Figures 4.6 and 4.7). The amount of ε_{rec} reaches a saturation value above a certain stress level even though ε_{irr} continues to increase with increasing bias stress. ε_{rec} levels are essentially the same for both ternary and quaternary alloys, however, they have smaller ε_{rec} as compared to binary TiNi, due to the B2 → B19 (orthorhombic) transformation path, which represents a smaller change in symmetry as opposed to the B2 → B19' (monoclinic) transformation in binary TiNi. ε_{irr} levels are much smaller in the TiNiPd alloy than that for binary TiNi. The $Ti_{50}Ni_{24.5}Pd_{25}Sc_{0.5}$ alloy exhibits a much smaller ε_{irr} at stresses greater than 150 MPa compared to $Ti_{50.5}Ni_{24.5}Pd_{25}$, which is a consequence of solid solution hardening due to the Sc addition or the relatively smaller grain size, both resulting in a matrix more resistant to dislocation slip or other irreversible processes.

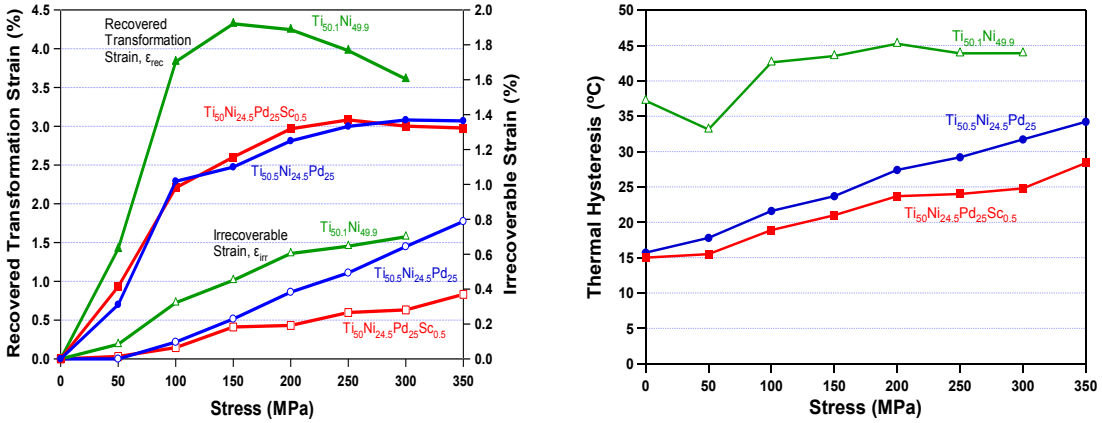

Figure 4.7 (a) Recovered transformation strain (ε_{rec}) and irrecoverable strain (ε_{irr}) responses of $Ti_{50.5}Ni_{24.5}Pd_{25}$ and $Ti_{50}Ni_{24.5}Pd_{25}Sc_{0.5}$ alloys and (b) corresponding thermal hysteresis levels as a function of bias stress determined from the isobaric cooling-heating experiments and DSC. The results from an equiatomic binary TiNi in the hot-rolled condition are also included for comparison.

4.2.3.2 Effect of Sc Addition on Thermal Hysteresis

Thermal hysteresis is caused by the dissipation of the energy input to the system through undercooling or applied stress. It arises due to the frictional losses against lattice friction and the generation of new interfaces or point and line defects, such as vacancies, self-interstitials, or dislocation formation to accommodate transformation shear and volume change [18, 117, 118]. If a material is strengthened due to solid solution hardening or precipitation hardening, defect generation and accommodation of transformation shear by defect formation becomes more difficult, and the shear is accommodated mainly in an elastic manner, resulting in a relatively lower thermal hysteresis [119]. Compatibility of the transforming phases also plays a major role in the

manifestation of thermal hysteresis. If the phases are very compatible, transformation shear and small volume change can be accommodated by only elastic distortion instead of twin formation or slip dislocations [81]. As discussed previously, λ_2, the second eigenvalue of the transformation stretch tensor, is an indicator of the compatibility between the austenite and martensite phases. Since λ_2 is essentially the same in both the ternary and quaternary TiNiPd alloys, the two materials display essentially the same thermal hysteresis under stress-free conditions, as would be expected. Also, as Figure 4.7b indicates, thermal hysteresis for both TiNiPd alloys increases with increasing stress levels. This is because of the fact that the accommodation of the transformation shear and volume change proceeds with increasing buildup in internal strain due to the aforementioned defect generation mechanisms under increasing applied stress levels. However, with exception of the stress-free condition, the $Ti_{50}Ni_{24.5}Pd_{25}Sc_{0.5}$ alloy exhibits slightly less thermal hysteresis at all stress levels than $Ti_{50.5}Ni_{24.5}Pd_{25}$. This infers that the $Ti_{50}Ni_{24.5}Pd_{25}Sc_{0.5}$ alloy has a stronger matrix which resists the formation of defects better than the ternary alloy at equivalent stress levels, due to solid solution hardening by Sc. So less internal strain develops at each stress level.

Both TiNiPd alloys exhibit significantly smaller thermal hysteresis than near-equiatomic binary TiNi. This is, in part, due to the fact that λ_2 for TiNi is 0.9663 [120], notably different as compared to λ_2 values for the TiNiPd alloys which are closer to 1. Additionally, Pd improves the lattice compatibility between the transforming phases, due to the change in martensite symmetry, (i.e., TiNiPd austenite transforming to

orthorhombic martensite and TiNi austenite transforming to monoclinic martensite), contributing to the significant reduction in thermal hysteresis in the TiNiPd alloys.

4.2.3.3 Effect of Sc Addition on Transformation Temperatures

Figures 4.8a and 4.8b are the stress vs. temperature phase diagrams for $Ti_{50.5}Ni_{24.5}Pd_{25}$ and $Ti_{50}Ni_{24.5}Pd_{25}Sc_{0.5}$, respectively. Transformation temperatures M_s^σ, M_f^σ, A_s^σ, A_f^σ, as determined from the isobaric cooling-heating experiments, are plotted as a function of the bias stress levels. Least square lines are fit through these data points and the slope of each line is presented in the figures. For the zero stress level, the temperatures obtained from the second thermal cycle of the DSC analyses are used. Clearly, transformation temperatures change almost linearly with stress, though in some cases a bilinear relationship is observed.

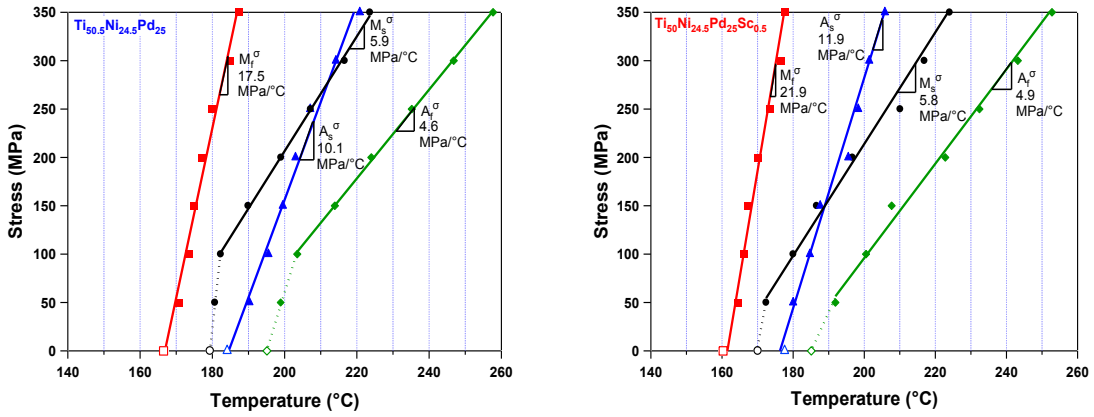

Figure 4.8 Stress vs. temperature phase diagram of (a) $Ti_{50.5}Ni_{24.5}Pd_{25}$ and (b) $Ti_{50}Ni_{24.5}Pd_{25}Sc_{0.5}$.

It is immediately obvious that the stress-transformation temperature linear fits for each transformation temperature are not parallel to each other for both alloys, indicating changes in stored elastic energy and dissipated energy as a function of stress [119]. To better understand these changes, we discuss how the different energy contributions affect the shape of the strain-temperature responses in Figure 4.6 from which the stress vs. transformation temperature data points were extracted. According to Hamilton *et al.* [119], the slope of the strain vs. temperature response during the forward and reverse transformations under each stress (Figure 4.6) is mainly dictated by evolution of stored elastic strain energy with stress. Higher the stored elastic strain energy is, shallower the slope of the curve becomes [119]. Clearly, these slopes become shallower with increasing bias stress, as seen in Figure 4.6, since the escalating transformation strain with stress (Figure 4.7a) leads to a rise in stored elastic strain energy. Thus, the ramification of such rise is the increase in $M_s^\sigma - M_f^\sigma$ and $A_f^\sigma - A_s^\sigma$ with stress, as observed in Figures 4.8a and 4.8b. It can be concluded, from the difference between the slopes of the stress-M_f^σ (or stress-A_s^σ) fit lines for the two alloys (while they have similar slopes for the stress-M_s^σ (or stress-A_f^σ) fit lines), that $Ti_{50}Ni_{24.5}Pd_{25}Sc_{0.5}$ has a larger stored elastic energy under stress as compared to $Ti_{50.5}Ni_{24.5}Pd_{25}$. Since the recovered transformation strains of both alloys are about the same (Figure 4.7), then the difference in stored elastic energies should arise from more pronounced dissipation of stored elastic energy in the ternary alloy due to the relaxation of the coherency strains of martensite–austenite interfaces [121, 122]. Plastic accommodation of transformation volume change and transformation shear causes the relaxation of the coherency strains. Thus, plastic

accommodation in the quaternary alloy should be less, pointing out the solid-solution hardening effect of Sc.

The stress-A_s^σ and stress-M_s^σ lines cross for both alloys but at significantly different stress levels. At stresses above the intersection, the elastic strain energy stored during the forward transformation is enough to start the reverse transformation at a temperature equal to or lower than M_s^σ. $Ti_{50}Ni_{24.5}Pd_{25}Sc_{0.5}$ has a lower cross-over stress compared to $Ti_{50.5}Ni_{24.5}Pd_{25}$, which implies higher elastic strain energy storage at a given stress level for $Ti_{50}Ni_{24.5}Pd_{25}Sc_{0.5}$.

It is interesting to note that the linear fits in Figure 4.8, especially for the stress-M_s^σ and stress-A_f^σ lines, do not extrapolate well to the transformation temperatures at zero stress level determined from the DSC analyses. For $Ti_{50.5}Ni_{24.5}Pd_{25}$, within the 0-100 MPa applied stress range, M_s^σ and A_f^σ shift 1 °C per 34.5 MPa and per 11.9 MPa stress increase, respectively. At higher stress levels, M_s^σ increases at a rate of 5.9 MPa/°C, whereas A_f^σ increases at 4.6 MPa/°C. On the other hand, for $Ti_{50}Ni_{24.5}Pd_{25}Sc_{0.5}$ the discrepancy is less pronounced. Within the 0-50MPa applied stress range, M_s^σ and A_f^σ temperatures shift 1 °C per 21.7 MPa and 7.4 MPa stress increases, respectively. At higher stress levels, M_s^σ increases at a rate of 5.8 MPa/°C, whereas A_f^σ increases at 4.9 MPa/°C.

Kockar *et al.* [66] explained this two slope stress-transformation temperature relationship by a large elastic modulus mismatch between the transforming phases

especially at close proximity to M_s^{σ} due to lattice softening, and by the inelastic accommodation of this mismatch. As the accommodation proceeds, the defect density is expected to increase leading to a need for larger undercooling to grow martensite. However, once the amount of single variant martensite increases and the transformation temperatures move significantly above the M_s temperature due to stress, the extent of the mismatch decreases resulting in the stress-temperature response with shallower slopes.

4.2.4 Thermal Cycling Experiments under Constant Stress

Both alloys were thermally cycled ten times between 100 °C and 280 °C, the same temperature range used in the isobaric cooling-heating experiments, under a constant stress of 200 MPa. This is an intermediate stress level, which is expected to provide a good representation of the evolution of thermal hysteresis, ε_{rec} and ε_{irr} levels as a function of cycle count. Similar to isobaric cooling-heating experiments, the samples were first heated to the upper temperature of the cycle under no load and then the stress was applied at this temperature while the material was fully austenitic and then thermally cycled repeatedly. The strain vs. temperature responses of both materials are shown in Figures 4.9a and 4.9b.

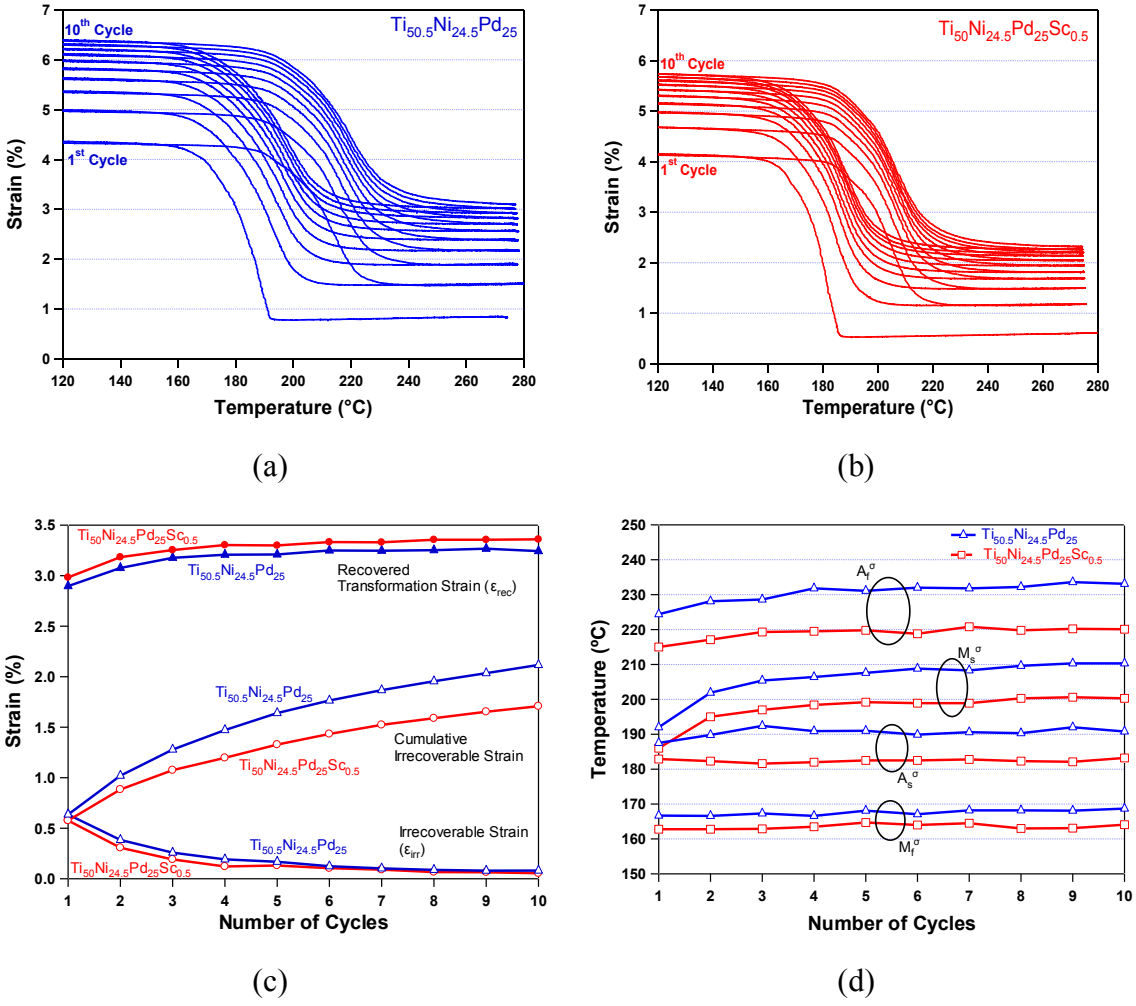

Figure 4.9 Cyclic strain vs. temperature response of (a) $Ti_{50.5}Ni_{24.5}Pd_{25}$ and (b) $Ti_{50}Ni_{24.5}Pd_{25}Sc_{0.5}$ at 200 MPa for 10 cycles. (c) The evolution of recovered transformation strain, ε_{rec}, irrecoverable strain, ε_{irr}, (d) transformation temperatures and (e) thermal hysteresis as a function of the number of cycles during thermal cycling under 200 MPa.

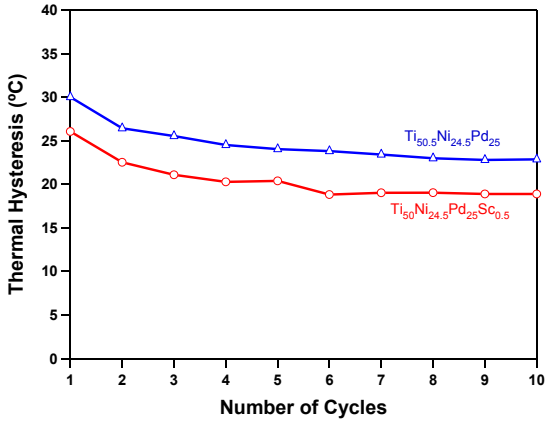

Figure 4.9 Continued.

At the end of ten cycles, $Ti_{50}Ni_{24.5}Pd_{25}Sc_{0.5}$ has a significantly lower accumulated ε_{irr} of 1.7 % as compared to the 2.1 % ε_{irr} for $Ti_{50.5}Ni_{24.5}Pd_{25}$ (Figure 4.9c). Both materials display a decrease in ε_{irr} with increasing cycle count, with $Ti_{50}Ni_{24.5}Pd_{25}Sc_{0.5}$ exhibiting lower values at each cycle. At the end of ten cycles, ε_{irr} per cycle stabilizes, yet still continues to accumulate. $Ti_{50.5}Ni_{24.5}Pd_{25}$ has an ε_{irr} of 0.08 %, while ε_{irr} of $Ti_{50}Ni_{24.5}Pd_{25}Sc_{0.5}$ is 0.05 % for the tenth cycle. The reason for ε_{irr} accumulation might be due to the build-up of dislocations and other defects, or retained martensite during repeated phase transformations. Cycling appears to have little effect on ε_{rec}, since both materials show similar ε_{rec} values throughout the cycling process. For example, ε_{rec} is approximately 2.9 % in the first cycle and stabilizes at 3.3 % for $Ti_{50.5}Ni_{24.5}Pd_{25}$ while it is initially 3.0 % for $Ti_{50}Ni_{24.5}Pd_{25}Sc_{0.5}$ and saturates at 3.4 %.

In contrast to the slightly depressed transformation temperatures observed during thermal cycling under no load in the DSC (Figure 4.1), transformation temperatures of

both materials remain constant or actually increase with cycling while under load (Figure 4.9d). The M_s^σ temperature for $Ti_{50.5}Ni_{24.5}Pd_{25}$ is 192 °C for the first cycle and stabilizes at 210 °C at the end of the ninth cycle, whereas the M_s^σ temperature for $Ti_{50}Ni_{24.5}Pd_{25}Sc_{0.5}$ is initially 186 °C and stabilizes at 200 °C at the end of the eighth cycle. The A_f^σ temperature follows a similar trend to that of M_s^σ temperature. It is initially 224 °C for $Ti_{50.5}Ni_{24.5}Pd_{25}$ and stabilizes at the end of the fourth cycle at 232 °C. For $Ti_{50}Ni_{24.5}Pd_{25}Sc_{0.5}$, A_f^σ is 215 °C for the first cycle and stabilizes at the end of the fourth cycle at 220 °C. On the other hand, M_f^σ and A_s^σ temperatures are almost unaffected by thermal cycling under load. Thermal hysteresis values for $Ti_{50}Ni_{24.5}Pd_{25}Sc_{0.5}$ are on average 4 °C lower than those of $Ti_{50.5}Ni_{24.5}Pd_{25}$ throughout the cycling process (Figure 4.9e).

Any retained martensite and local internal stresses associated with defects, which should have preferred directions due to the cycling under stress and reoriented/detwinned martensite formation, assist the nucleation of the same martensite variants that are biased by the external stress during cycling, thus raising the M_s^σ temperature. Similarly, an increased dislocation or defect density with the number of thermal cycles may reduce energy dissipation caused through additional plastic deformation, especially at the onset of transformation, leading to a decrease in thermal hysteresis (Figure 4.9e) [123]. It is important to note here that the increase in M_s^σ temperature with thermal cycling under stress is just the opposite of the effect seen during thermal cycling without stress in Section 4.2.1. This is mainly due to the local

oriented internal stress in the former case. The defects created during thermal cycling in DSC should lead to randomly distributed internal stresses, due to the self-accommodated structure of thermally-induced martensite, and thus, impede the nucleation of martensite variants in the subsequent cycles, resulting in a decrease in M_s temperature.

Overall, the observations, especially in Sections 4.2.3 and 4.2.4, support the positive influence of a dilute Sc addition on the reversibility of the martensitic transformation and functional stability of TiNiPd alloys due to solid solution hardening, enhancing the material strength against irrecoverable deformation processes. Yet, the measured effects are relatively small, probably due to the small amount of Sc addition. However, as the thermal cycling results show, the cumulative effect can be quite significant, especially with long-term thermal cycling. Furthermore, larger Sc additions may enhance these benefits as well as improve lattice compatibility, reducing the amount of inelastic/plastic accommodation of the transformation shear and shape change, and will be the subject of the following section.

4.3 Furher Alloying Trials with 3 at. % Sc Addition

Once successful results were obtained with 0.5 at. %Sc microalloying, billets with 3 at. % Sc were fabricated to analyze the effects of larger Sc additions. 3 at. % Sc addition decreased the transformation temperatures of the ternary $Ti_{50.5}Ni_{24.5}Pd_{25}$ by more than 100 °C causing this material no longer to qualify as an HTSMA. In addition, except for a reduction in the thermal hysteresis, there was not a significant improvement in the functional stability compared to the 0.5 at. % Sc doped alloy. Therefore, a full

characterization study was not conducted for $Ti_{47.5}Ni_{24.5}Pd_{25}Sc_3$ as was done for $Ti_{50}Ni_{24.5}Pd_{25}Sc_{0.5}$.

4.3.1 Isobaric Cooling-Heating Experiments

Figure 4.10a compares the strain vs. temperature response of $Ti_{50.5}Ni_{24.5}Pd_{25}$ and its quaternaries with 0.5 and 3 at. % Sc additions at selected stress levels. ε_{rec} values slightly decrease after the addition of 3 at. % Sc while ε_{irr} levels remain unchanged as compared to those of 0.5 at. % Sc doped alloy (Figure 4.10b). Thermal hysteresis values are improved upon the addition of 3 at. % Sc additions (Figure 4.10c), however, as mentioned above, transformation temperatures are severely suppressed. Attempts of recovering the transformation temperatures of $Ti_{47.5}Ni_{24.5}Pd_{25}Sc_3$ through annealing heat treatments did not prove to be very useful, resulting in an increase of only 15-20 °C (Figure 4.10d). It is yet unknown whether most of the added Sc precipitated out leaving a Ni-rich matrix or Sc was in the solution and led to a change in the chemical energy balance of the material. Further characterization studies were abandoned after the attempts to increase the transformation temperatures.

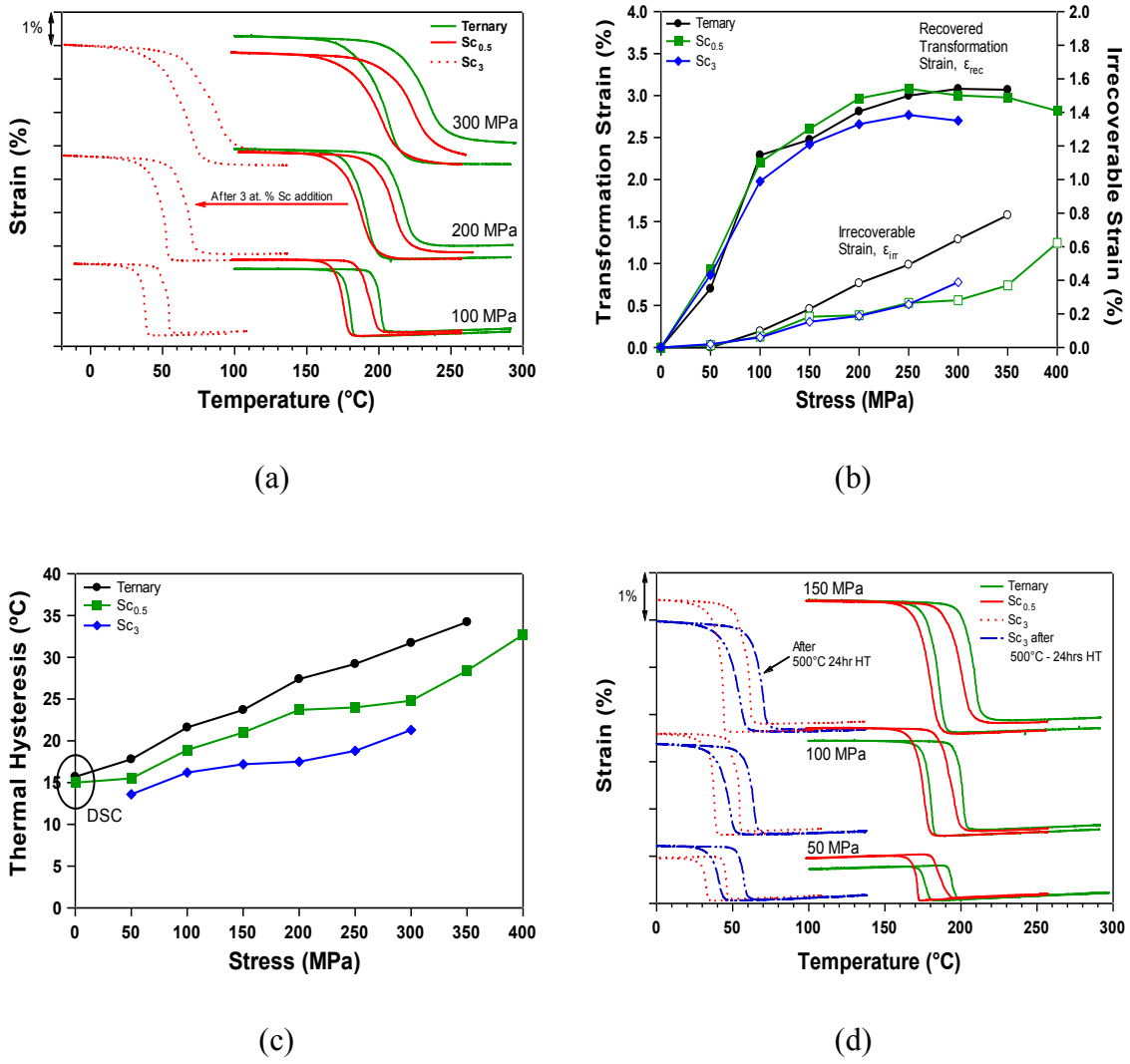

Figure 4.10 (a) Strain vs. temperature responses of $Ti_{50.5}Ni_{24.5}Pd_{25}$ alloyed with different amounts of Sc. Sc was shown to decrease the transformation temperatures of $Ti_{50.5}Ni_{24.5}Pd_{25}$. (b) The evolution of recovered transformation strain, ε_{rec}, irrecoverable strain, ε_{irr} and (c) thermal hysteresis as a function of applied stress. (d) The change in transformation temperatures after an annealing heat treatment at 500 °C for 24 hours.

4.4 Summary and Conclusions

In this chapter, the effect of Sc microalloying on the microstructure and shape memory behavior of $Ti_{50.5}Ni_{24.5}Pd_{25}$ HTSMA was investigated. The following results were observed:

1. Under stress-free conditions, the $Ti_{50}Ni_{24.5}Pd_{25}Sc_{0.5}$ alloy exhibited slightly lower transformation temperatures, by 6-10 °C, compared to $Ti_{50.5}Ni_{24.5}Pd_{25}$. For example, the M_f temperature decreased from 166 °C to 160 °C, while the A_f temperature decreased by 10 °C from 195 °C to 185 °C upon the addition of 0.5 at. % Sc. The reason for the actual decrease in transformation temperatures was attributed to the presence of the Sc.
2. The Sc addition was beneficial for increasing the strength of $Ti_{50.5}Ni_{24.5}Pd_{25}$ against irreversible deformation processes. As compared to $Ti_{50.5}Ni_{24.5}Pd_{25}$, $Ti_{50}Ni_{24.5}Pd_{25}Sc_{0.5}$ demonstrated lower irrecoverable strain and thermal hysteresis when thermally cycled over a range of constant bias stresses. These benefits were attributed to solid-solution hardening effects.
3. Both ternary and quaternary TiNiPd alloys exhibited significantly smaller thermal hysteresis than equiatomic binary TiNi due to the enhancement in the lattice compatibility between austenite and martensite, and the change in martensite crystal structure due to the Pd addition. As a result, ε_{rec} of the ternary and quaternary alloys were lower than that of the binary alloy.
4. The 0.5 at. % Sc substitution for 0.5 at. % Ti in the $Ti_{50.5}Ni_{24.5}Pd_{25}$ alloy seems to have no significant effect on ε_{rec} levels.

5. Lower thermal hysteresis and ε_{irr} accumulation in $Ti_{50}Ni_{24.5}Pd_{25}Sc_{0.5}$ during constant stress thermal cyclic experiments indicate the effectiveness of alloying $Ti_{50.5}Ni_{24.5}Pd_{25}$ with Sc. The quaternary alloy responds to training more efficiently by reaching a given ε_{irr} value in a smaller number of cycles as compared to the ternary alloy.
6. The overall results indicate the effectiveness of alloying $Ti_{50.5}Ni_{24.5}Pd_{25}$ with Sc. The alloyed material has shown a trend towards enhanced functional stability as compared to the base ternary material.
7. Higher Sc contents further improved the shape memory characteristics as evidenced by smaller irrecoverable strains and thermal hysteresis widths in isobaric cooling-heating experiments. However, the transformation temperatures were severely suppressed at the same time, rendering this material no more feasible to be used as an actuator in high-temperature applications.

CHAPTER V

SHAPE MEMORY CHARACTERISTICS OF $Ti_{49.5}Ni_{25}Pd_{25}Sc_{0.5}$ HIGH-TEMPERATURE SHAPE MEMORY ALLOY AFTER SEVERE PLASTIC DEFORMATION*

In this chapter, the viability of using severe plastic deformation (SPD) combined with annealing heat treatments was investigated in an effort to enhance the functional stability of a $Ti_{49.5}Ni_{25}Pd_{25}Sc_{0.5}$ HTSMA during repeated thermal cycles under constant loads. Equal channel angular extrusion (ECAE) was selected as the method of the SPD process. The processed materials displayed enhanced shape memory response, exhibiting higher recoverable transformation and reduced irrecoverable strain levels upon thermal cycling as compared to the unprocessed material. This improvement was attributed to the increased strength and resistance of the material against defect generation upon phase transformation as a result of the microstructural refinement due to the ECAE process.

5.2 Microstructural Characterization

5.2.1 Microstructure

Figure 5.1a is a scanning electron micrograph of the as-received $Ti_{49.5}Ni_{25}Pd_{25}Sc_{0.5}$ in back-scattered electron mode recorded at room temperature. This

---

* Reprinted with permission from "Shape memory characteristics of $Ti_{49.5}Ni_{25}Pd_{25}Sc_{0.5}$ high-temperature shape memory alloy after severe plastic deformation" by Atli KC, Karaman I, Noebe RD, Garg A, Chumlyakov Y, Kireeva I, 2011. Acta Materialia, 59, pp. 4747-4760, Copyright 2011 by Acta Materialia Inc. published by Elsevier Ltd.

material was found to have a very similar microstructure to that of $Ti_{50}Ni_{24.5}Pd_{25}Sc_{0.5}$ studied in the previous chapter. A homogeneous distribution of coarse second-phase particles, found out to be TiC and Sc_2O_3 from WDS analyses, was observed throughout the structure. The total volume percentage of TiC and Sc_2O_3 particles was 4.7 ± 0.2 %., while their average size was 1.7 ± 0.7 µm. Grain sizes ranged from 8 µm to 16 µm, the average being about 12 µm. The matrix composition was slightly Ti lean at 49.0 ± 0.1 (at. %) according to the WDS measurements (Table 5.1).

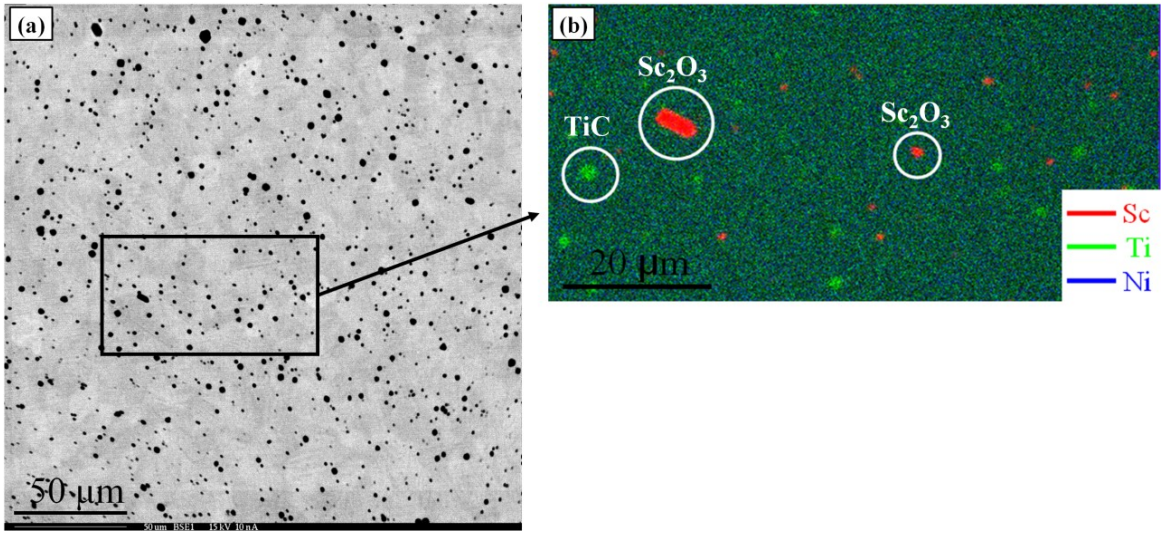

Figure 5.1 (a) Backscattered electron micrograph of the as-received $Ti_{49.5}Ni_{25}Pd_{25}Sc_{0.5}$ showing the distribution of coarse second phase particles. (b) X-ray elemental mapping showing the types of second phase particles present in the microstructure.

Table 5.1 WDS analysis results for $Ti_{49.5}Ni_{25}Pd_{25}Sc_{0.5}$. Reported errors are the standard deviations from three measurements randomly taken on the matrix.

Material	Ti (at. %.)	Ni (at. %.)	Pd (at. %.)	Sc (at. %.)
$Ti_{49.5}Ni_{25}Pd_{25}Sc_{0.5}$	49.0 ± 0.1	25.1 ± 0.2	25.4 ± 0.1	0.49 ± 0.02

Figure 5.2a is a transmission electron micrograph of the as-received material taken at room temperature. $(1\bar{1}1)$ type I twins with sizes ranging from 50 to 100 nm were observed, which were also reported in [11] for the same alloy. The selected area diffraction patterns show the presence of a B19 orthorhombic structure. X-ray diffraction analysis also confirmed this finding, indicating a B19 martensite structure with lattice parameters of a = 2.79 Å, b = 4.44 Å c = 4.69 Å, and B2 austenite with a_0 = 3.09 Å (Figure 5.3). These values are comparable to the lattice parameters of $Ti_{50}Ni_{24.5}Pd_{25}Sc_{0.5}$ studied in the previous section.

Figure 5.2b is a transmission electron micrograph showing the heavily deformed microstructure of the ECAE processed sample at room temperature. The image was taken from the flow plane which is parallel to the side face of the ECAE processed billet. Martensite plates with much finer (on the order of 20 to 30 nm) $(1\bar{1}1)$ type I twins were observed in this condition. Figure 5.2c is the same location of the thin foil as shown in Fig. 5.2b when heated above the A_f temperature, to 380 °C. The pronounced grain refinement after ECAE processing can easily be seen in this micrograph and in the

attached selected area diffraction pattern: the latter also confirms the B2 austenite structure. The nano-sized austenite grains, some of which are indicated by dashed circles, are on the order of 100-200 nm.

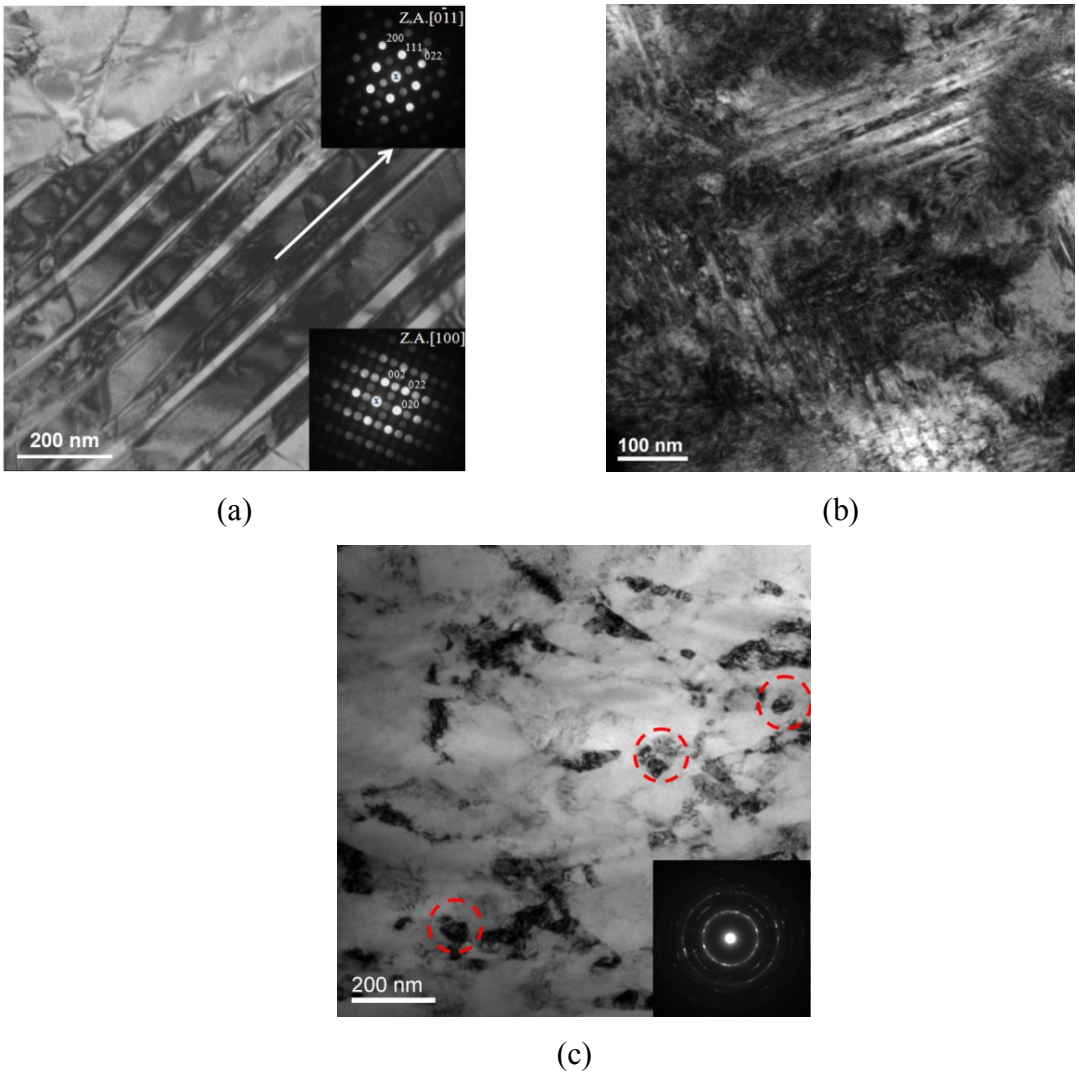

(a) (b)

(c)

Figure 5.2 Transmission electron micrographs for the (a) as-received $Ti_{49.5}Ni_{25}Pd_{25}Sc_{0.5}$ with the corresponding selected area diffraction patterns showing a B19 orthorhombic structure, (b) the flow plane of the ECAE processed $Ti_{49.5}Ni_{25}Pd_{25}Sc_{0.5}$ at room temperature, (c) the same area in (b) when heated to 380 °C, demonstrating the austenitic structure with

sub-micron sized grains marked by dashed circles.

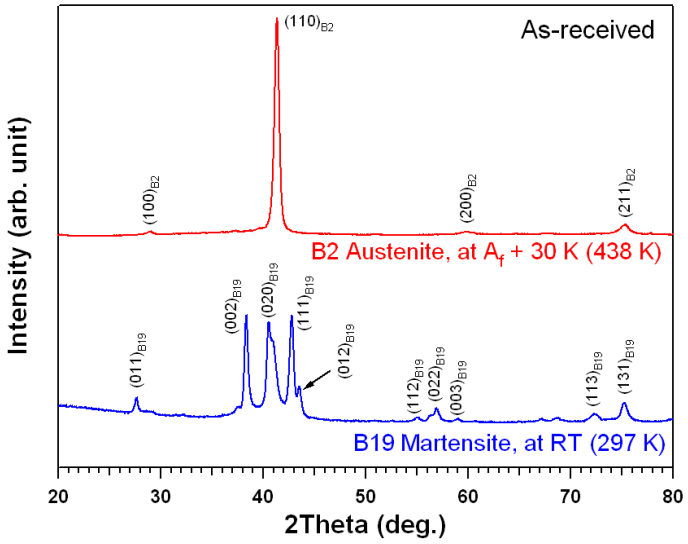

Figure 5.3 XRD analyses confirming the low temperature B19 orthorhombic structure and high-temperature B2 cubic structure of the as-received $Ti_{49.5}Ni_{25}Pd_{25}Sc_{0.5}$.

5.2.2 Microhardness

It is a common practice to apply post-deformation annealing treatments to cold-worked materials to relieve internal stresses and recover some of the dislocation substructure. For example, a post-ECAE low temperature annealing procedure was shown to result in improved functional stability in ECAE processed TiNiHf HTSMAs [79]. Similarly, for binary TiNi, it is essential to recover the microstructure to a certain extent and annihilate the undesired stored dislocations in the grain/subgrain interiors. These dislocations are believed to act as barriers to phase front motion and cause nucleation of additional martensite nuclei with further undercooling instead of the

propagation of existing phase fronts. Annihilation of these dislocations without recrystallization and the presence of a higher density of grain/subgrain boundaries are expected to improve the shape memory characteristics such as transformation temperatures and transformation strain as compared to those of the ECAE processed samples. These characteristics are, however, very sensitive to the temperature and duration of the heat treatment. Therefore, an annealing study was conducted to characterize the change in hardness in the ECAE processed material after heat treatments at various temperatures. The duration of the heat treatments was kept at 1hr.

As observed in Figure 5.4, there is a non-linear decrease in hardness with increasing annealing temperature. A dramatic decrease in hardness can be seen after heat treatment above 400 °C. At lower annealing temperatures the change in hardness is much less significant, and the corresponding change in microstructure should be minimal with some rearrangement and annihilation of less stable dislocations induced by the ECAE process. At higher temperatures above 500 °C, recrystallization is expected to occur with a decrease in the stored energy of the deformed structure, re-arranged or annihilated dislocations, and formation of new grains. It should be noted that the hardness value at 600 °C is still higher than the hardness of the as-received material.

From the hardness profile in Figure 5.4, 300 °C was selected as the temperature for the annealing heat treatment of the ECAE processed material for further thermomechanical characterization. At this specific annealing temperature, the microstructure should be slightly recovered with less stable dislocations annealed out and more stable ones at the grain/subgrain boundaries while maintaining most of the

beneficial effects of SPD on shape memory characteristics. To prove this hypothesis, a series of isobaric cooling-heating experiments were conducted on both ECAE processed and post-ECAE 300 °C annealed samples.

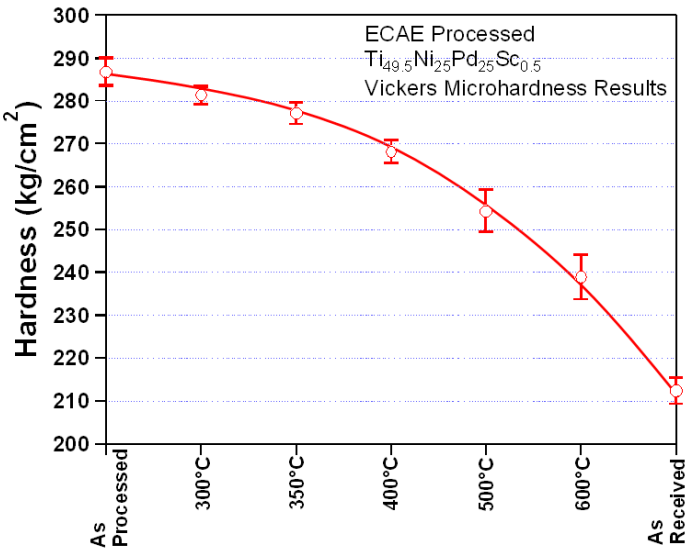

Figure 5.4 Vickers microhardness of the ECAE processed $Ti_{49.5}Ni_{25}Pd_{25}Sc_{0.5}$ before and after annealing heat treatments at various temperatures for 1 hr. The hardness of the as-received material is included as the reference. The circles represent the average of five tests and the bars one standard deviation.

5.3 Stress-Free Phase Transformation Temperatures

As-received, ECAE processed and post-ECAE annealed materials were cycled 5 times in the DSC within a temperature range of 40 °C to 180 °C. DSC responses for the as-received and ECAE processed materials are shown in Figure 5.5a and 5.5b, respectively. Stress-free transformation temperatures M_f, M_s, A_s and A_f along with ΔH_{net} values for the second cycle of each condition were measured from these results (see the

table on p.80). Transformation temperatures for the ECAE processed sample were found to be lower than the as-received material (Figure 5.5c). M_s temperatures differ by 18 °C, while there is a difference of 16 °C between the A_f temperatures (Table 5.2). The decrease in the transformation temperatures upon ECAE results mainly from the high density of dislocations making the phase front motion difficult. The thermal hysteresis values, as defined by the difference between A_f and M_s temperatures, are comparable: thermal hysteresis is 18.4 °C for the as-received material, while it is 21 °C after the ECAE processing. In terms of cyclic stability, the ECAE processed material shows a superior behavior having only a total shift of 0.9 °C in the M_s temperature after 5 thermal cycles. On the other hand, the M_s temperature for the as-received material drops by 4.8 °C. ΔH_{net} values differ significantly before and after ECAE processing. The ECAE processed material has a ΔH_{net} of 9.5 J/g, which is nearly half of the ΔH_{net} value of the as-received material, 18.0 J/g. The post ECAE annealing heat treatment (300 °C for 1 hr.) hardly affected the transformation temperatures, thermal hysteresis and ΔH_{net} values of the ECAE processed material. A pronounced effect could only be seen in cyclic stability, from a change after 5 thermal cycles of 0.9 °C in the ECAE processed material to 2.7 °C in the post ECAE-annealed sample (Table 5.2).

The decrease in ΔH_{net} after ECAE processing is due to the introduction of elastic constraints and refinement of the microstructure that results in a higher magnitude of stored elastic energy during transformation, which would otherwise be released as latent heat [117]. The transformation characteristics of the ECAE processed sample observed in the isobaric cooling-heating experiments (Section 5.5.1) also support this rationale.

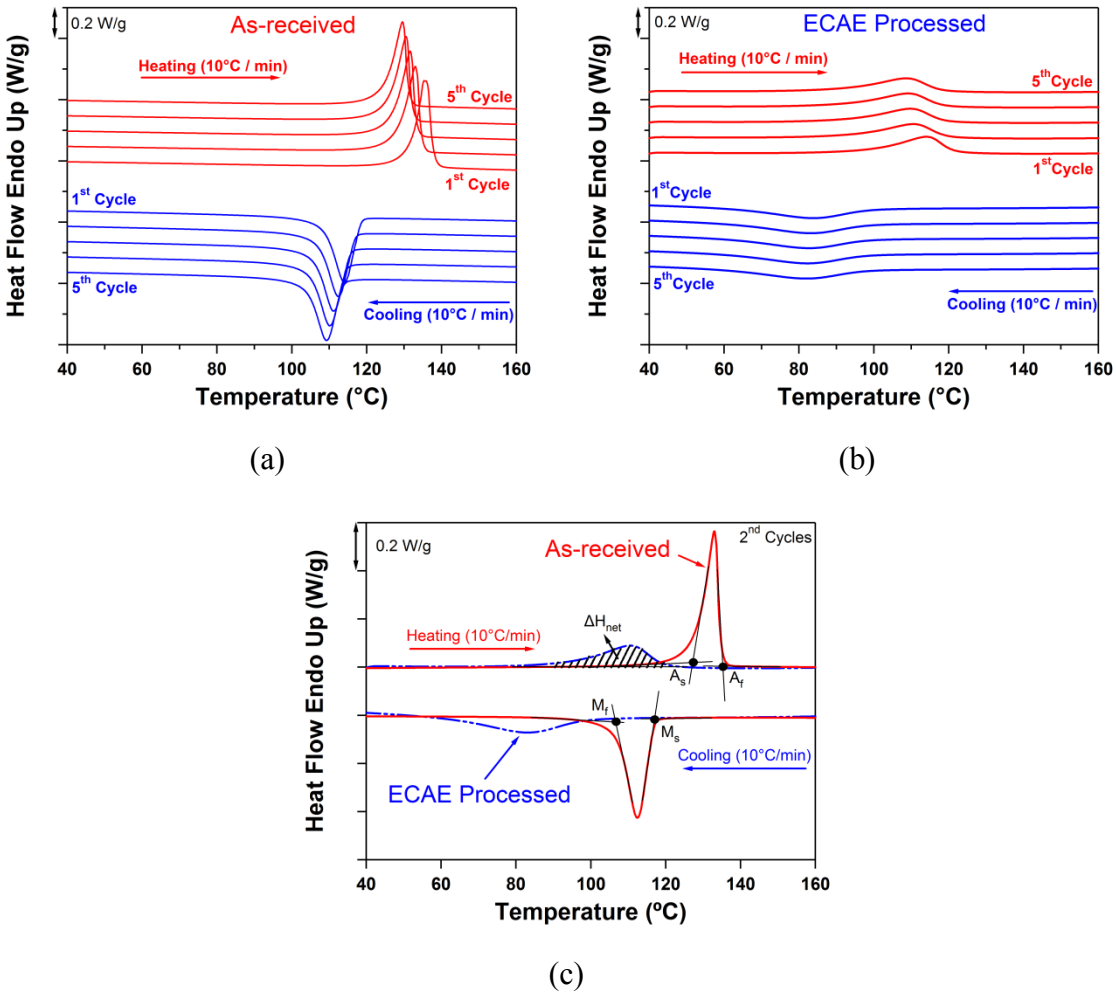

Figure 5.5 The change in stress-free transformation temperatures over five thermal cycles for (a) as-received $Ti_{49.5}Ni_{25}Pd_{25}Sc_{0.5}$ and (b) ECAE processed $Ti_{49.5}Ni_{25}Pd_{25}Sc_{0.5}$. (c) Comparison of the second heating-cooling cycles for the as-received (solid lines) and ECAE processed (dashed lines) material illustrating the effects of ECAE processing on the transformation behavior.

It is also possible that the amount of transforming volume is smaller in the ECAE processed samples due to retained austenite, which would also reduce $\Delta H_{net}^{P\rightarrow M}$. This

might be due to nano-sized grains and the associated large elastic mismatch across their boundaries [66] or to the high dislocation density induced by the ECAE process, which generates an internal stress state impeding the transformation. A similar decrease in ΔH_{net} has been reported for TiNi wires after cold-rolling [124].

Table 5.2 Transformation temperatures (M_f, M_s, A_s, A_f), net heat evolved during the transformation (ΔH_{net}), shift in the M_s temperature between the first and the fifth thermal cycles (M_s^{5th}-M_s^{1st}), and thermal hysteresis (A_f-M_s) of the as-received, 4E-425 °C ECAE processed, and 300 °C-1hr post-ECAE annealed $Ti_{49.5}Ni_{25}Pd_{25}Sc_{0.5}$. M_f, M_s, A_s, A_f, ΔH_{net} and thermal hysteresis values were calculated from the second cycle of the DSC analyses.

Material	M_f (°C)	M_s (°C)	A_s (°C)	A_f (°C)	ΔH_{net} (J/g)	M_s^{5th}-M_s^{1st} (°C)	Thermal Hysteresis (A_f-M_s) (°C)
As-received	105.8	117.3	126.3	135.7	18.0	4.8	18.4
ECAE processed	62.1	99.1	93.7	120.1	9.5	0.9	21.0
Post-ECAE Annealed	65.3	94.6	99.4	115.7	9.0	2.7	21.1

5.4 Thermomechanical Characterization

5.4.1 Isobaric Cooling-Heating Experiments

Figure 5.6a shows the strain vs. temperature response of the as-received $Ti_{49.5}Ni_{25}Pd_{25}Sc_{0.5}$ at increasing stress levels. The material was loaded up to a stress of 400 MPa, at which the ε_{rec} level started to decline as illustrated in Figure 5.6c. Figure 5.6b illustrates the strain vs. temperature behavior of samples with different processing

conditions under an applied stress of 200 MPa. ECAE processing leads to a reduction in the ε_{rec} and transformation temperatures, but also resulted in a decrease in ε_{irr}, leading to a more stabilized thermomechanical response. As shown in Figure 5.6c, the annealing heat treatment improved the shape memory characteristics of the ECAE processed material. The post-ECAE annealed material exhibited both higher ε_{rec} levels and better dimensional stability (lower ε_{irr} levels) than those of the as-received material up to an applied stress of at least 200 MPa. It should be noted that the post-ECAE annealed material failed at 250 MPa due to a brittle fracture outside the gage section. A maximum ε_{rec} of about 3 % was achieved for both the post-ECAE annealed and the as-received material, but these were reached at different stress levels: the former at 200 MPa and the latter at 350 MPa.

The change in thermal hysteresis with increasing stress is shown in Figure 5.6d. The as-received material has an initial no-load thermal hysteresis of 10.7 °C, which increases with the applied stress reaching 27.7 °C at 400 MPa. It should be noted that thermal hysteresis of the as-received material as determined by DSC does not correlate well with the value measured during thermal cycling (Figure 5.6d). According to the DSC results, as-received material has a thermal hysteresis of 18.4 °C, which is nearly twice the value determined from the no-load thermal cycling result. A possible reason of this discrepancy might be that DSC directly measures the enthalpy of transformation, while it is the strain associated with the transformation that is measured during no-load thermal cycling. In other words, the indicators for the temperatures at which thermal hysteresis is measured are different; for example, the sample may transform notably,

forming self-accommodated martensite variants and releasing latent heat without showing significant external strain.

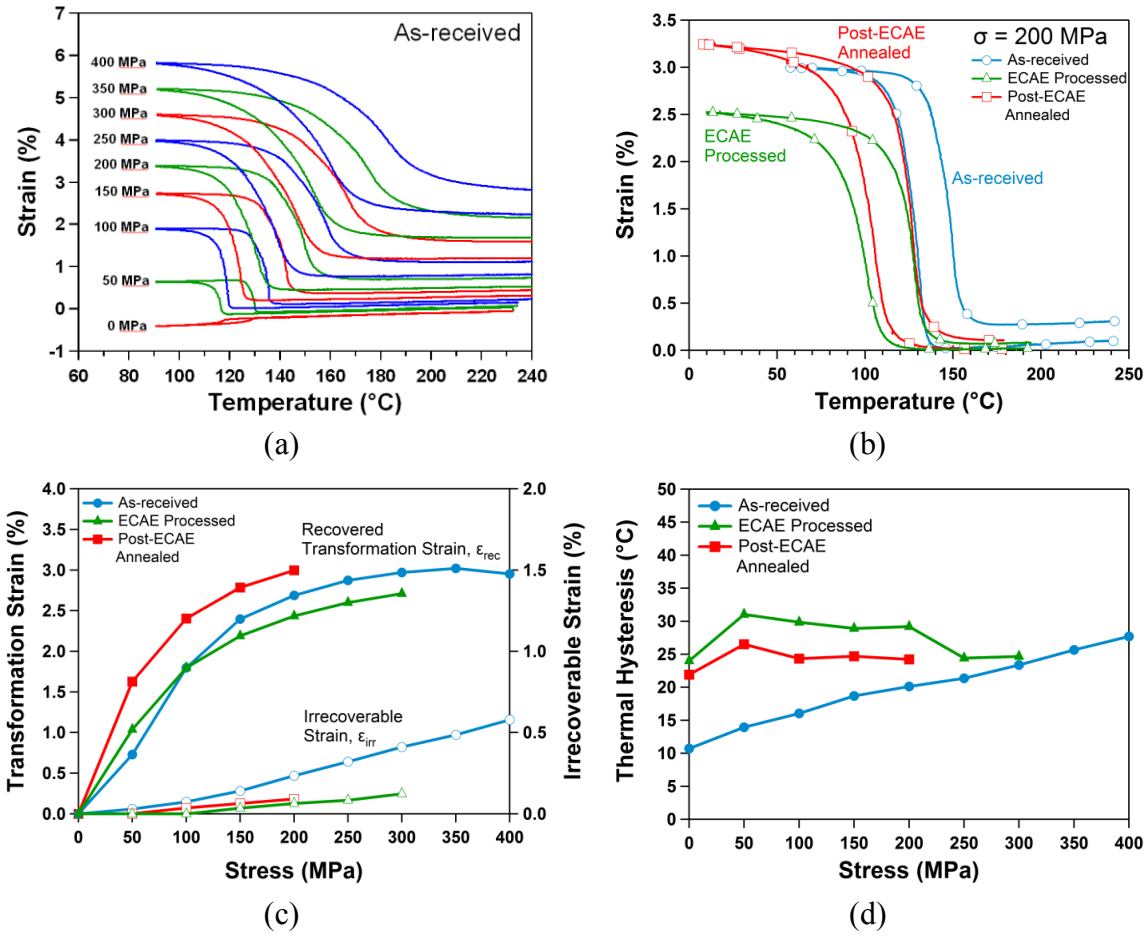

Figure 5.6 (a) Strain vs. temperature response of the as-received $Ti_{49.5}Ni_{25}Pd_{25}Sc_{0.5}$ at various stress levels. (b) Comparison of the strain vs. temperature responses of the as-received, 4E-425 °C ECAE processed, and post-ECAE annealed material under 200 MPa. (c) Recovered transformation strain (ε_{rec}) and irrecoverable strain (ε_{irr}) values at each stress level, (d) evolution of the thermal hysteresis with successive stress levels and (e) change in M_s and A_f temperatures as a function of applied stress for the as-received, ECAE processed and post-ECAE annealed materials.

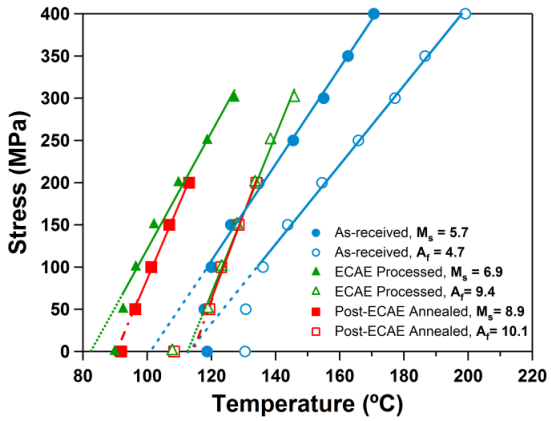

(e)

Figure 5.6 Continued.

Both the ECAE processed and post-ECAE annealed materials have initially higher thermal hysteresis values as compared to the as-received material. The ECAE processed material has an initial thermal hysteresis of 24.0 °C at 0 MPa, increasing to 31.0 °C at 50 MPa and finally decreasing to 24.6 °C at 300 MPa. The post-ECAE annealed material has a slightly lower initial thermal hysteresis due to the partial recovery of the microstructure after heat treatment. It starts with an initial thermal hysteresis of 21.9 °C at 0 MPa, increasing to 26.5 °C at 50 MPa, and dropping to 24.2 °C at 200 MPa.

Figure 5.6e is the stress vs. temperature phase diagrams showing the variation of M_s^σ and A_f^σ temperatures with respect to applied stress. Transformation temperatures were determined from the strain vs. temperature curves at each stress level per Figure 5.6. It is clear from the Figure 5.7e. that ECAE processed materials exhibit steeper slopes than the as-received material for both M_s^σ and A_f^σ, probably due to the lower ε_{rec},

since according to the Clausius-Clapeyron relation for the first order phase transformations under stress, lower transformation strain leads to a higher stress vs. temperature slope [49]. In addition, according to Wollants *et al.* [49], the transformation enthalpy under stress may be different in these two materials due to the difference in the reversible elastic work of transformation, which again affects the stress vs. temperature slope through the Clausius-Clapeyron relation.

5.4.2 Thermal Cycling Experiments under Constant Stress

The objective of thermal cyclic experiments was to investigate the evolution of the shape memory response of the materials under a constant stress. Tests were conducted for ten cycles under a tensile stress of 200 MPa for both the as-received and ECAE processed materials. As shown in the previous section, 200 MPa was an intermediate stress level, which was expected to provide a good representation of the evolution of ε_{rec}, ε_{irr} and thermal hysteresis. Repeated strain recovery vs. temperature behavior of the as-received and ECAE processed materials are shown in Figures 5.7a and 5.7b, respectively.

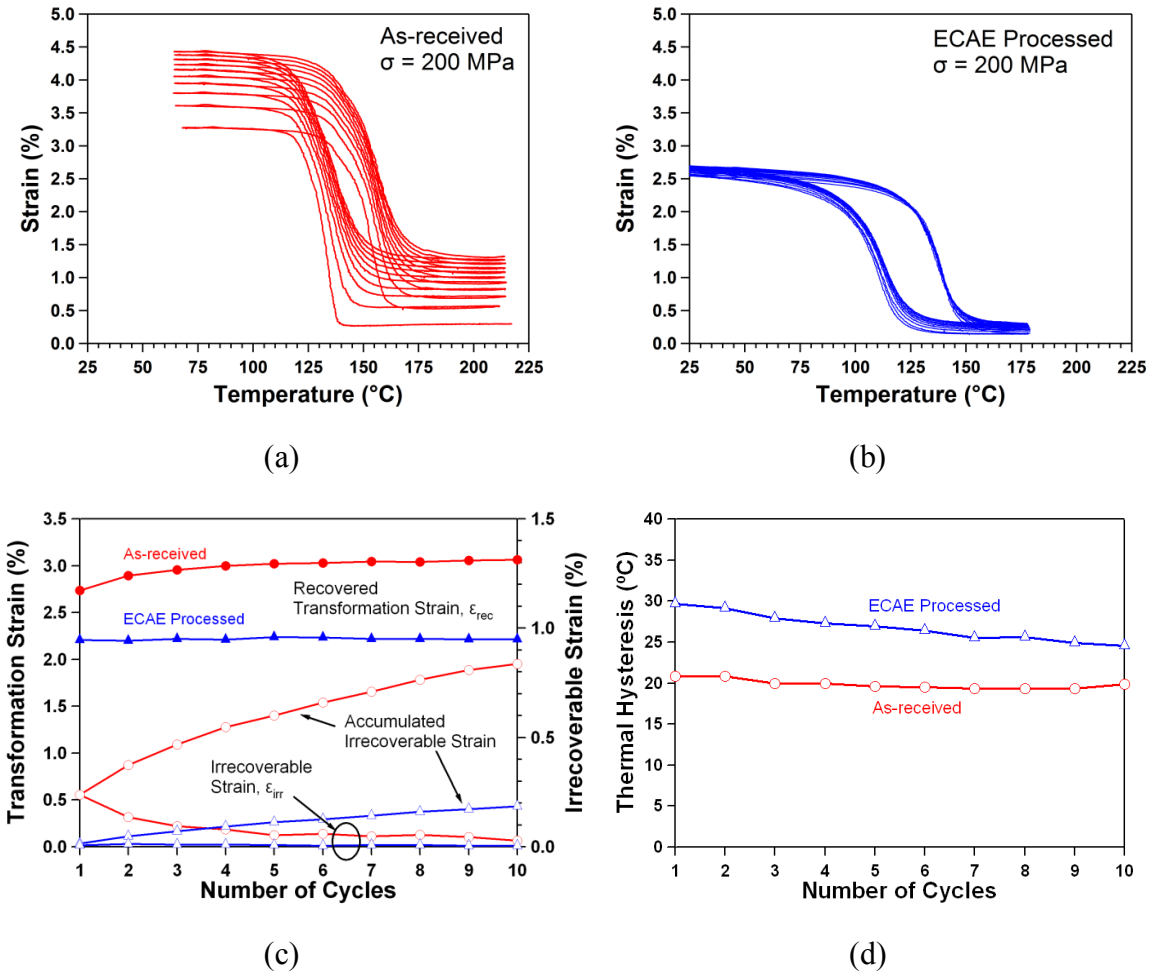

Figure 5.7 A comparison of the strain vs. temperature response for ten cycles at 200 MPa for both the (a) as-received $Ti_{49.5}Ni_{25}Pd_{25}Sc_{0.5}$ and (b) 4E-425 °C ECAE processed material. Comparisons of (c) ε_{rec} and ε_{irr}, (d) thermal hysteresis and (e) M_s^{σ} and A_f^{σ} temperatures as a function of the number of cycles for the as-received material (circles), and ECAE processed material (triangles).

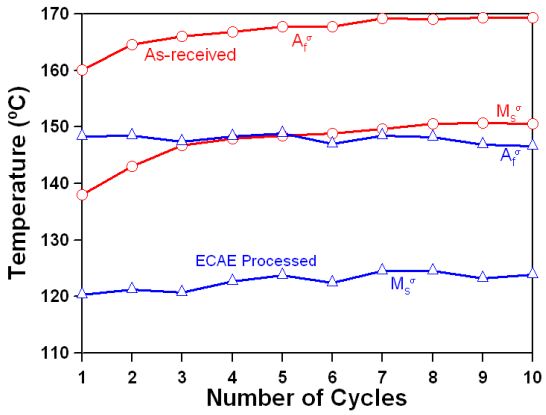

(e)

Figure 5.7 Continued.

The as-received material shows a total accumulated ε_{irr} of 0.83 % while this value is only 0.18 % for the ECAE processed material at the end of the ten thermal cycles (Figure 5.7c). The ε_{irr} shows a decreasing trend with cycling for the as-received material. On the other hand, it is almost stable for the ECAE processed material, not evolving with the number of cycles. Even at the tenth thermal cycle, ε_{irr} for the as-received material is still higher than the ε_{irr} value for the ECAE processed material at the first cycle. ε_{rec} saturates quickly for both materials during cycling (Figure 5.7c). ε_{rec} of the as-received material is initially 2.73 % and saturates at 3.05 % at the end of the sixth cycle. ε_{rec} of the ECAE processed material is lower than that of the as-received material, having an average of 2.22 % and does not evolve with cycle count, showing a stable response. The lower ε_{rec} levels with the ECAE processed material are expected, since similar results have already been observed during isobaric cooling-heating tests under an applied stress

of 200 MPa (Figure 5.6b). This is likely a result of grain size and crystallographic texture difference between the as-received and ECAE processed materials, and difficulty in detwinning and martensite reorientation due to intergranular constraints introduced by ECAE processing.

Thermal hysteresis of the as-received material is nearly constant at 20 °C throughout the 10 thermal cycles (Figure 5.7d). This level of thermal hysteresis is quite low compared to binary TiNi, which is on the order of 40 °C [66] and other ternary alloys such as TiNiHf (60 °C) [79] under the same externally applied stress level. ECAE processed material, on the other hand, shows a decreasing hysteresis with cycle count, initially starting at 30 °C, and reaching a value of 24.5 °C at the end of the tenth cycle.

Figure 5.7e shows the evolution of transformation temperatures M_s^σ and A_f^σ as a function of the number of cycles. Transformation temperatures of the as-received material initially increase and then level off at the end of the seventh cycle. M_s^σ is 138.0 °C at the beginning and reaches 150.6 °C at the end of the 10 cycles, while A_f^σ starts from 160.1 °C and saturates at 169.4 °C. The ECAE processed material has lower transformation temperatures under stress and displays a more stable behavior: M_s^σ increases by only 3.6 °C from 120.3 °C to 123.9 °C, while A_f^σ actually decreases from 148.3 °C to 146.6 °C.

5.4.3 Isothermal Monotonic Loading Tests

In the previous sections, SPD via ECAE has been shown to be an effective method to improve the shape memory response of $Ti_{49.5}Ni_{25}Pd_{25}Sc_{0.5}$. The improvements in performance demonstrated thus far should be a result of the strengthening due to microstructural refinement and increased dislocation density as seen in Figures 5.2b and 5.2c. To demonstrate this strength increase, isothermal monotonic loading experiments were conducted. It is well known that $\sigma_y^M - \sigma_{SIM}$, the difference between the critical stress to induce martensite, σ_{SIM}, and the yield strength of the stress-induced martensite, σ_y^M, is an indicator of enhanced shape memory response [66, 125]. A larger difference is a sign of superior shape memory behavior, due to the increased resistance of the material to plastic deformation. Monotonic experiments were carried out under compression for both the as-received and ECAE processed samples to determine $\sigma_y^M - \sigma_{SIM}$. Initial tests under tension resulted in premature failure of the samples, not allowing for the detection of σ_y^M. Instead, compression experiments were conducted to quantify the strengthening due to SPD.

Figure 5.8 shows the stress-strain behavior of the as-received and ECAE processed material. It is seen that σ_{SIM} remains almost the same, around 480 MPa, for the onset of stress-induced martensite after ECAE processing in a nearly equivalent thermodynamic condition. However, the value of σ_y^M is considerably higher for the ECAE processed material, which could not actually be detected during the test since the

load cell limit was reached at 1800 MPa before the specimen plastically deformed macroscopically. σ_y^M of the as-received material was found to be around 1350 MPa. Consequently, $\sigma_y^M - \sigma_{SIM}$ is noticeably larger for the ECAE processed material, consistent with the more stable shape memory response displayed by this material compared to the as-received condition.

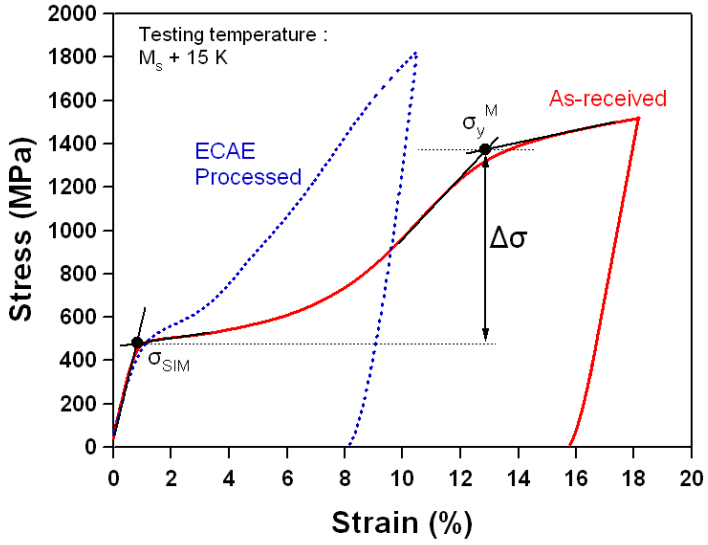

Figure 5.8 Isothermal monotonic compressive behavior of the as-received and 4E-425 °C ECAE processed $Ti_{49.5}Ni_{25}Pd_{25}Sc_{0.5}$ at M_s+15 °C so that the initial loading is performed in the fully austenitic condition. It should be noted that M_s temperatures are different for the two materials but the experiments were conducted under nearly equivalent thermodynamic conditions with respect to the martensitic transformation. The method for determining the critical stress to induce martensite, σ_{SIM}, and yield stress for martensite, σ_y^M, is illustrated on the stress-strain curves.

5.5 Discussion

In this section, a microstructural scenario is suggested for the interpretation of the thermomechanical characterization results. The schematic illustration of the possible changes in the microstructure of both the as-received and ECAE processed material during thermal cycling under different stress levels is shown in Figure 5.9 to better understand the differences observed in the ε_{rec}, ε_{irr} and thermal hysteresis levels.

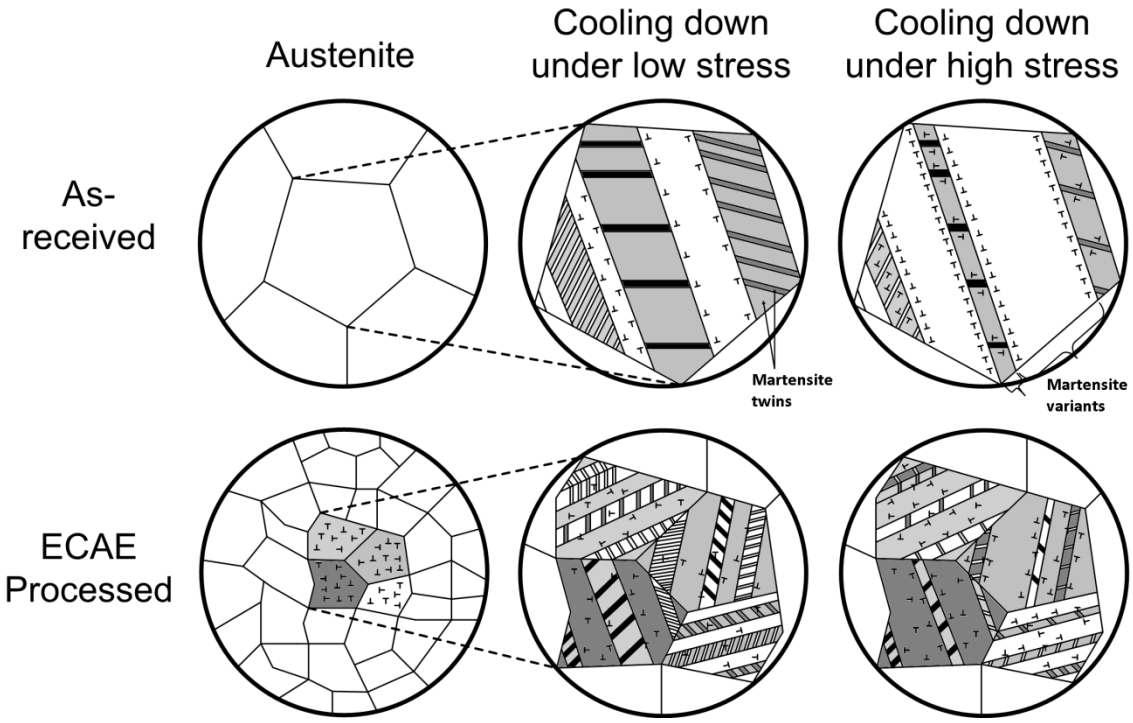

Figure 5.9 Representation of the microstructural evolution for both the as-received and 4E-425 °C ECAE processed material during thermomechanical cycling. ECAE processed material has a microstructure with relatively finer grains and higher dislocation density as compared to the as-received material. The formation of martensite variants and the generation of dislocations during phase front motion under different stress levels are illustrated.

The initial as-received material has a relatively low dislocation density with coarse grains. At low actuation stresses, the transformation on cooling proceeds with a mixture of self-accommodated and single variant martensite. Phase front motion is easy due to the soft parent phase structure and the transformation is mainly nucleation controlled. Motion of these phase fronts result in the storage of elastic strain energy, increasing the amount of undercooling, i.e. M_s-M_f, required to complete the transformation. At higher stress levels, the structure is dominated by a larger fraction of single variant martensite that is most favored by the applied stress. In this case, most of the transformation shear and volume change is accommodated by dislocations due to the low strength of the material.

ECAE processing introduces a high density of dislocations and refined grain size. At low actuation stresses, there is a mixture of self-accommodated and single variant martensite, as in the as-received case. However, the size scale of the variants is smaller. Due to the higher strength of the material, resulting from the refined grain size and higher dislocation density, the movement of the phase fronts is now harder. In addition, due to the smaller grain size and the necessity to accommodate the mismatch across the grain boundaries, the martensitic transformation is expected to be more propagation controlled, leading to a larger fraction of self-accommodated martensite variants, and finer variant and twin structures. Indeed, the larger M_s^σ - M_f^σ values in the ECAE case (Figure 5.6a and 5.6b) and much higher hardening during the stress-induced martensitic transformation in Figure 5.8 support this argument. Under an increased applied stress, the volume percentage of single variant martensite increases. In contrast to the as-

received material, the transformation shear and volume change in the ECAE processed material is mostly accommodated elastically due to the higher strength of the material rendering additional defect generation difficult.

The annealing heat treatment after ECAE processing partially recovers the structure through rearrangement and annihilation of dislocations. This type of change in the microstructure is expected to result in the formation of a larger volume percentage of single variant martensite at a given stress level, which can more easily propagate in the relatively softer annealed material as opposed to that of the ECAE processed material.

5.5.1 Mechanisms Responsible for the Differences in ε_{rec} and ε_{irr} Levels

ECAE processing increases the strength of the as-received material due to microstructural refinement and increased dislocation density. As mentioned in Section 5.2, while ECAE induced dislocations impede the phase front motion, they also cause the nucleation of more martensite nuclei instead of the propagation of existing phase fronts [20] . Thus, the ECAE processed sample has lower transformation strain as compared to the as-received sample because of lower fractions of reoriented/detwinned martensite. To obtain a specific level of ε_{rec}, higher external stresses are needed for the ECAE processed material as compared to the as-received material to obtain an equivalent volume fraction of single variant martensite, which would generate that level of ε_{rec}. Even at very high stress levels, ε_{rec} of the ECAE processed samples may not be as high as coarse-grained counterparts due to the intergranular constraints, assuming crystallographic textures to be the same. To satisfy the compatibility across the grain

boundaries in ultrafine grained SMAs, there should still exist martensite variants near the grain boundaries that are different than the ones favored by the externally applied stress. Since the volume fractions of these self-accommodated structures would be substantial in ultrafine grained samples, externally measured transformation strains should be smaller than those of the coarse grained samples. After annealing, the dislocations in the grain/subgrain interiors are likely to relax, and thus, ε_{rec} returns to levels typical of the as-received material.

ECAE processed material exhibits a more stable thermal cyclic response compared to the as-received material. Higher ε_{irr} levels for the as-received material should be related to plasticity with the introduction of dislocations or other defects during repeated transformations under stress. These defects can also stabilize martensite variants and prevent reverse transformation to the parent phase upon heating. Regardless, the ECAE processed material displays more stable behavior with less plasticity and/or less change in the amount of stabilized martensite. In this case, post-ECAE annealing had little effect on ε_{irr} values of the ECAE processed material due to the limited recovery of the material. And in both cases, the ε_{irr} values were considerably smaller than those of the as-received material due to the increased strength.

5.5.2 Mechanisms Responsible for the Difference in Thermal Hysteresis

In Chapter IV, it was shown that the Sc addition decreased the energy dissipation, and thus the thermal hysteresis, in TiNiPd alloys through its solid solution hardening effect and by improving the compatibility between the transforming phases.

Still, the steady increase in the thermal hysteresis values of the as-received material during isobaric cooling-heating tests can be attributed to the relatively low strength of the material, which accommodates transformation shape change more plastically, generating additional defects and dissipating more energy. This is also evidenced by the continuous increase in the ε_{irr} with increasing stress levels.

Due to the increased strength of the ECAE processed material, from a higher density of forest dislocations in the grain/subgrain interiors and more severe variant-variant interaction, the movement of the phase fronts is harder, resulting in relatively higher energy dissipation and thus higher thermal hysteresis values under low stress levels. At increased stress levels, variant-variant interaction decreases leading to a drop in the dissipated energy during transformation (Figure 5.7d). Moreover, with the repeated passage of phase fronts, the existing defects in the ECAE processed sample are favorably rearranged such that they cause less lattice friction and energy dissipation in subsequent cycles, leading to a drop in thermal hysteresis values, as demonstrated in Figure 8.d.

5.5.3 Anomaly in Stress vs. Temperature Phase Diagrams at Low Stress Levels

The two-slope stress-transformation temperature relationship explained previously in Section 4.2.3.3 will be revisited here. In Figure 5.6e, it was shown that the linear fits did not extrapolate well to data below 100 MPa for the as-received and ECAE processed material, while they did extrapolate quite closely for the post-ECAE annealed material down to 0 MPa. This anomaly was explained by Kockar *et al.* [66] for as-

annealed equiatomic TiNi in terms of elastic modulus mismatch between the transforming phases and the inelastic accommodation of this mismatch and transformation shape change under stress. They suggested that for the as-received material, the accommodation proceeds with defect generation leading to a need for larger undercooling to grow martensite. On the other hand, according to Kockar *et al.* [66], the ECAE processed material accommodates the mismatch elastically due to the increased slip resistance requiring the same amount of undercooling to grow martensite nuclei throughout the entire applied stress range. This is contrary to the present results for the ECAE processed quaternary TiNiPdSc, which shows a similar behavior to the as-received material. There are three main factors that should be taken into account to better understand this behavior. Firstly, the main difference between the present case and that of Kockar *et al.* [17] is the differences in the martensite structures (and thus, elastic properties) and transformation temperatures. Secondly, the additional undercooling, which is the result of energy dissipation during the nucleation and growth of martensite nuclei to reach the critical size, is a consequence of both inelastic accommodation of the elastic mismatch and transformation shape change, and the frictional work to grow the nuclei. In the present case, the inelastic accommodation should have been suppressed due to the increase in the materials strength after ECAE, which is supported by the reduction in ε_{irr}. However, the frictional work required to grow the nuclei seems to increase as well, probably due to the high dislocation density and unstable dislocation structure. This, in turn, causes additional dissipation during the nucleation and further undercooling under stress. The noticeable difference in the transformation hysteresis of

as-received and ECAE processed materials in Figure 5.6d demonstrates the increase in the frictional work and support this hypothesis. At this point, it is reasonable to conclude that post-ECAE annealing recovers the structure enough, resulting in less unstable dislocations and dissipation during martensite nucleation, while still preserving sufficient strength to accommodate the transformation mismatch elastically. Therefore, no additional undercooling is required for the transformation at low stress levels resulting in better extrapolation of the data from high stress levels to the low-stress regime.

5.6 Summary and Conclusions

In this chapter, a $Ti_{49.5}Ni_{25}Pd_{25}Sc_{0.5}$ HTSMA was processed using SPD via ECAE. ECAE was selected as opposed to more conventional processing techniques such as rolling to obtain large cross-section HTSMAs with uniform microstructures and stable shape memory response under repeated thermomechanical loading. Post deformation annealing heat treatments were also performed on the ECAE processed samples to further improve the shape memory characteristics. The major findings of this study can be summarized as follows in the light of electron microscopy, x-ray diffraction, microhardness, and thermo-mechanical characterization results.

1. ECAE led to an overall increase in the strength of $Ti_{49.5}Ni_{25}Pd_{25}Sc_{0.5}$ against plasticity. While there was not a detectable change in the critical stress to initiate stress-induced martensite under nearly equivalent thermodynamic conditions, ECAE processing significantly increased the value of the yield strength of the

stress-induced martensite from 1350 MPa to a level above 1800 MPa. Such a significant increase in the yield strength of martensite is due to the high dislocation density and microstructural refinement upon ECAE, creating ultrafine austenite grains on the order of 100-200 nm.

2. Stress-free transformation temperatures of the as-received $Ti_{49.5}Ni_{25}Pd_{25}Sc_{0.5}$ decreased by almost 20 °C after ECAE processing. On the other hand, ECAE improved the thermal cyclic stability, resulting in a shift of transformation temperatures by only 0.9 °C after 5 thermal cycles in DSC as compared to the 4.8 °C shift in the as-received material. The most beneficial result of the ECAE was the achievement of high stability in repeated thermal cycling tests under a constant stress.
3. ECAE led to a decrease in recovered transformation strain, ε_{rec}, and irrecoverable strain, ε_{irr}, levels during thermal cycling tests under constant stress. Both observations were attributed to the increased strength of the material after ECAE processing and suppression of the plastic accommodation of transformation shear and volume change. ε_{rec} for a given stress level declined since higher stresses were required in the ECAE processed sample for the formation of the same amount of single variant martensite as in the as-received material.
4. Post deformation annealing heat treatments at low temperature improved the shape memory characteristics of the ECAE processed material, particularly ε_{rec}. Also, the post-ECAE annealed material exhibited higher ε_{rec} and lower ε_{irr} levels as compared to those of the as-received material.

5. Overall, ECAE improved the thermal cyclic stability of $Ti_{49.5}Ni_{25}Pd_{25}Sc_{0.5}$, while suppressing the transformation temperatures and ε_{rec}. The problem with a depressed ε_{rec} for the ECAE processed samples can be remedied by partially recovering the deformed structure with post-processing annealing treatments. The resulting material can be a good candidate for high-temperature actuator applications.

CHAPTER VI

SEVERE PLASTIC DEFORMATION OR THERMOMECHANICAL TRAINING? A COMPARATIVE ANALYSIS ON FUNCTIONAL STABILITY OF $Ti_{50.5}Ni_{24.5}Pd_{25}$*

Thermal cycling tests under a constant stress level, which were covered in Chapters IV and V, were primarily aimed at studying the evolution of shape memory behavior during repeated actuation. Later in the research, when the functional stability levels were investigated, as-received $Ti_{50.5}Ni_{24.5}Pd_{25}$ exhibited irrecoverable strain levels comparable to those of the ECAE-processed material after only 10 thermal cycles under 200 MPa. In addition, it also exhibited a relatively large amount of two-way shape memory strain (TWSM). In the previous chapter, the effects of ECAE followed by post-deformation annealing heat treatments on the functional stability of $Ti_{49.5}Ni_{25}Pd_{25}Sc_{0.5}$ HTSMA have been covered. This chapter compares the effectiveness of 10 thermal cycles under a constant stress level to the ECAE process in terms of achieving improved functional stability in a $Ti_{50.5}Ni_{24.5}Pd_{25}$ HTSMA. Thermomechanical testing indicated that both methods resulted in enhanced shape memory characteristics, such as reduced irrecoverable strain and thermal hysteresis during actuation.

---

* Reprinted with permission from "Comparative analysis of the effects of severe plastic deformation and thermomechanical training on the functional stability of $Ti_{50.5}Ni_{24.5}Pd_{25}$ high-temperature shape memory alloy" by Atli KC, Karaman I, Noebe RD, Maier HJ, 2011. Scripta Materialia, 64, pp. 315-318, Copyright 2011 by Acta Materialia Inc. published by Elsevier Ltd.

6.1 Experimental Methods

ECAE processing of the as-received $Ti_{50.5}Ni_{24.5}Pd_{25}$ was performed isothermally at 425 °C for 4 passes using route B_c. Further details concerning the ECAE processing were previously described in Section 3.2. Thermal cycling was conducted under an applied stress of 200 MPa for 10 cycles. The rationale behind the selection of the stress level as well as the number of cycles was explained in Section 4.2.4. The evolution of shape memory behavior during thermal cycling was illustrated in Figure 4.9a.

6.2 Microstructure

Figure 6.1a shows the microstructure of the as-received material. This material condition is taken as the reference state to explain how the functional behavior changes after different thermomechanical treatments. Martensite variants in several different orientations with fine internal twins can be observed. The structure developed after 10 thermal cycles is illustrated in Figure 6.1b. The microstructure of the thermally cycled material appears to have a higher degree of directionality as compared to the as-received material. Grossmann *et al.* [33] observed the same behavior in a TiNi actuator spring after 500 thermomechanical cycles.

Figure 6.1c shows the heavily deformed microstructure of the ECAE processed material. Noting the higher magnification level, it is observed that the microstructure has a finer twin and variant structure. On the other hand, no preferred orientations of the variants can be seen as in the thermally cycled material in Figure 6.1b. Figure 6.1d is an

even higher magnification image of the ECAE processed sample, showing sub-micron grains on the order of 100 – 150 nm.

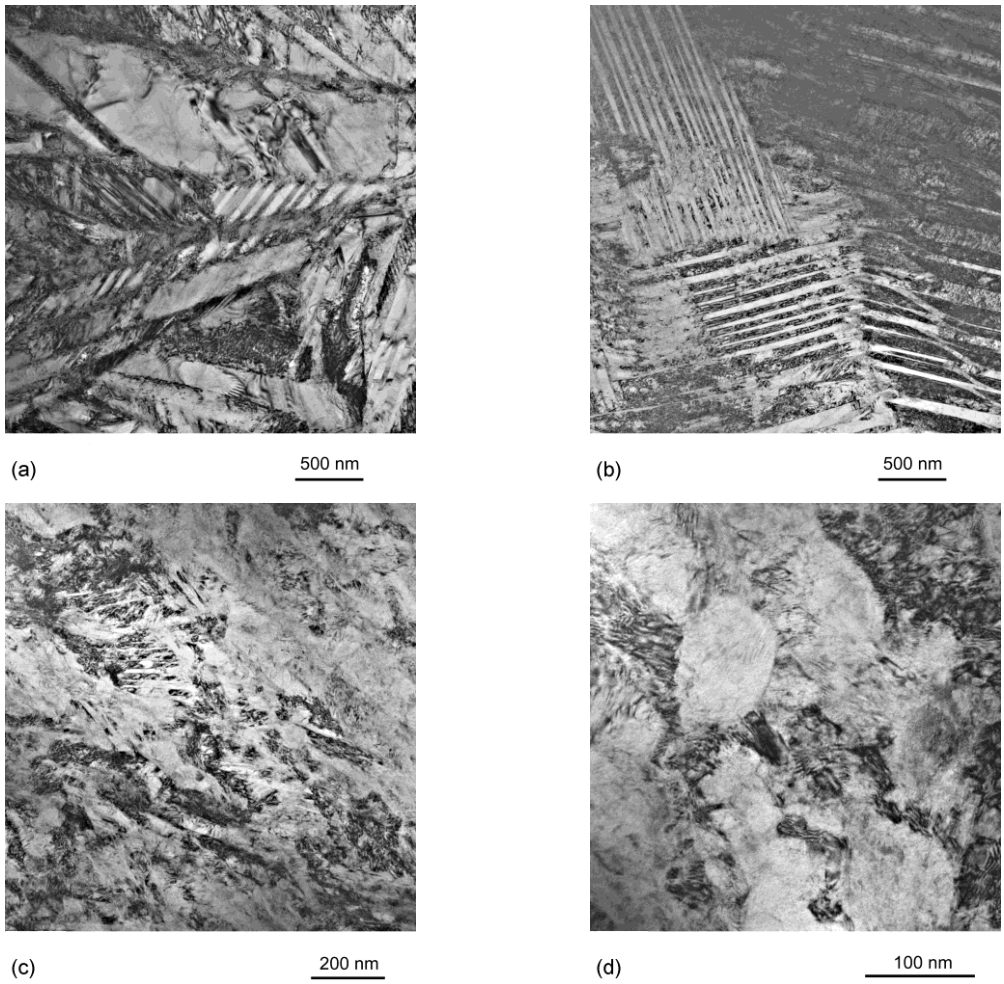

Figure 6.1 Microstructure of the (a) as-received $Ti_{50.5}Ni_{24.5}Pd_{25}$ showing multiple martensite variants with random orientations, (b) thermally cycled material showing a much more highly oriented microstructure. (c) Heavily deformed microstructure of the ECAE processed material having randomly oriented, finer variant and twin structures as compared to the as-received or the thermally cycled material and (d) high magnification image showing the sub-micron size grains in the ECAE processed material.

6.3 Thermomechanical Characterization

6.3.1 Stress-free Phase Transformation Temperatures

Stress-free transformation temperatures of the as-received, ECAE processed, and thermally cycled $Ti_{50.5}Ni_{24.5}Pd_{25}$ samples from the DSC analyses are listed in Table 6.1. Transformation temperatures of the ECAE processed sample are about 30 °C lower than those of the as-received material. The decrease in transformation temperatures is due to the high dislocation density and reduced grain size induced by ECAE processing, which both act as obstacles against lattice shear processes, rendering martensite nucleation and propagation more difficult [103]. ECAE processing also resulted in an increase in the thermal hysteresis. This indicates that transformation proceeds with increased energy dissipation in the ECAE processed material as a result of the increased strength of the material through grain refinement and higher dislocation density, more interaction of finer martensite variants, and intergranular constraints.

Table 6.1 Stress-free transformation temperatures of the as-received, ECAE processed and thermally cycled $Ti_{50.5}Ni_{24.5}Pd_{25}$ HTSMA.

	M_f (°C)	M_s (°C)	A_s (°C)	A_f (°C)	Thermal Hysteresis (A_f - M_s) (°C)
As-received	166.5	179.4	184.1	195.3	15.9
ECAE processed	118.3	147.2	147.4	167.7	20.5
Thermally Cycled	171.5	189.7	185.4	202.5	12.8

On the other hand, thermal cycling decreased the thermal hysteresis and increased the transformation temperatures, though only by a few degrees compared to the as-received material. Unlike the randomly oriented residual stress fields, which impede the transformation in the ECAE processed sample, stress fields remaining after thermal cycling assist the growth of preferential martensite variants in the thermally cycled sample, thereby resulting in an increase in transformation temperatures. Similarly, since each successive thermal cycle introduces a smaller amount of defects, transformation proceeds with less energy dissipation in the thermally cycled material yielding a lower thermal hysteresis. This behavior is analogous to the decrease in the stress required for triggering martensite formation and the width of the stress-strain hysteresis during repeated superelastic loading [126].

6.3.2 Isobaric Cooling-Heating Experiments

Isobaric cooling-heating experiments at different stress levels were conducted to characterize the strain-temperature response of the $Ti_{50.5}Ni_{24.5}Pd_{25}$ after the different processing conditions. Figure 6.2a is a comparison plot of the strain - temperature responses of the as-received, ECAE processed, and the thermally cycled materials at an applied stress of 200 MPa.

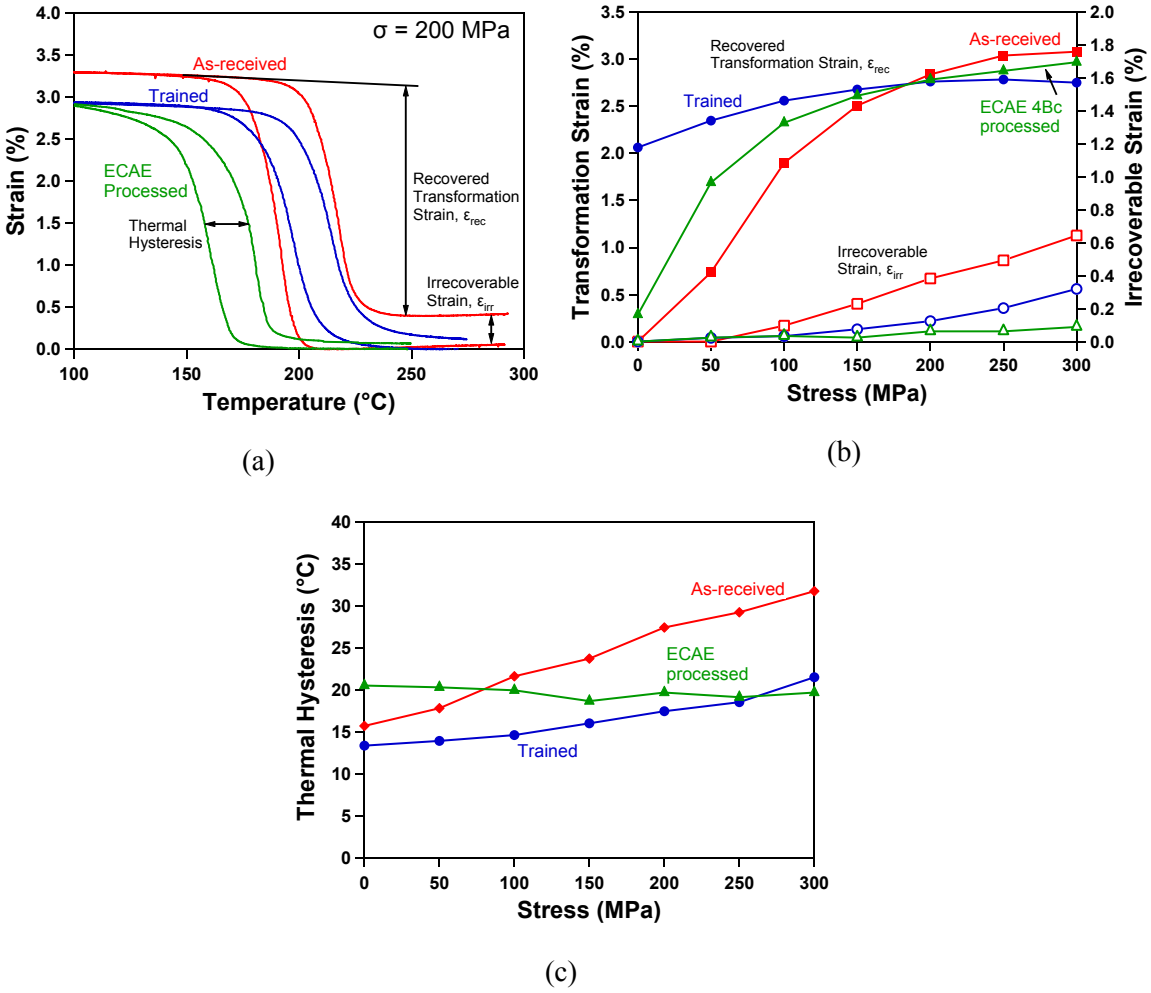

Figure 6.2 (a) Comparison of the strain vs. temperature responses under an applied stress of 200 MPa for $Ti_{50.5}Ni_{24.5}Pd_{25}$ after different processing treatments. (b) Evolution of the recovered transformation, ε_{rec}, irrecoverable strain, ε_{irr}, and (c) thermal hysteresis as a function of the applied stress for the as-received (diamonds), ECAE processed (triangles), and thermally cycled (circles) materials.

Figure 6.2b shows the evolution of ε_{rec} and ε_{irr} as a function of the applied stress. Poor performance of the as-received material, as indicated by the highest ε_{irr} levels, is probably related to plasticity with the introduction of dislocations or other defects during

repeated transformation under stress. The development of stabilized martensite variants, also known as retained martensite, which cannot revert to the parent phase upon heating to the upper temperature chosen in this study, might also constitute a part of these high ε_{irr} levels and is a serious concern particularly for TiNiPd alloys [127]. The ECAE processed sample displays the best functional stability with the lowest ε_{irr} values at each stress level. As illustrated in Figures 6.1c and 6.1d, ECAE processing induces a high dislocation density and refines the microstructure of the as-received material, increasing its strength against the generation of additional defects or the evolution of additional stabilized martensite, especially at stresses below the thermal cycling stress. The major question is how much retained martensite is actually present in the ECAE processed material and whether ECAE processing actually stabilizes this fraction of retained martensite, so that it doesn't continue to evolve during subsequent thermomechanical testing.

The thermally cycled sample also displays enhanced functional stability as compared to the as-received material at all stresses and comparable ε_{irr} values to the ECAE processed sample at low stresses. The improvement over the as-received material can be explained with a similar dislocation-based scenario, i.e. the existence of dislocations induced by thermal cycling impedes further plasticity or the formation of additional stabilized martensite. Although this limited strength increase through thermal cycling gives an adequate functional stability at low stresses, ε_{irr} values start to increase at the same rate as those of the as-received sample at higher stresses, especially above the thermal cycling stress.

The ECAE processed material and the thermally cycled material exhibit higher ε_{rec} values as compared to the as-received material at low applied stresses. In addition, the thermally cycled material has a 2 % two-way shape memory (TWSM) strain, which results from the development of stabilized variants of martensite due to the stress fields associated with the defects induced by thermal cycling. This was previously illustrated in Figure 6.1b, where the thermally cycled sample had a large fraction of favorably oriented martensite variants. The ε_{rec} increased only slightly with increasing stress in the thermally cycled material, saturating at about 200 MPa (thermal cycling stress). In contrast, the ε_{rec} values for the as-received and ECAE processed material started out lower than that for the thermally cycled material but eventually surpassed the thermally cycled material at stresses greater than 200 MPa. The maximum ε_{rec} values are similar for the as-received and ECAE processed material and occurred at an applied stress of 300 MPa, while the thermally cycled material was relatively insensitive to stress level saturating at a 0.4 % lower ε_{rec}. It is likely that a fraction of the martensite variants was stabilized during the thermal cycling process, which decreased the maximum ε_{rec} that could be obtained in this material. However, below 200 MPa the thermally cycled material exhibited superior ε_{rec} levels.

Thermal hystereses of the as-received and thermally cycled samples increase steadily with applied stress, reaching 32 °C and 22 °C, respectively, at 300 MPa (Figure 6.2c). This increase can be attributed to the relatively low strength of the material against defect generation, accommodating more transformation shape change plastically and dissipating more energy. In contrast, the thermal hysteresis associated with the ECAE

processed sample stays almost constant around 20 °C regardless of stress level, again demonstrating the resistance of this material against defect generation.

6.4 Summary and Conclusions

In this chapter, thermal cycling for multiple cycles under a constant stress level was applied to a $Ti_{50.5}Ni_{24.5}Pd_{25}$ high-temperature shape memory alloy to improve its functional stability for actuator applications. For comparison purposes, the same material was severe plastically deformed using the ECAE process. Major findings and conclusions that can be drawn from this chapter are as follows:

1. A low cycle thermomechanical cycling process improved the shape memory properties of the as-received $Ti_{50.5}Ni_{24.5}Pd_{25}$ resulting in a 2 % TWSM strain, improved dimensional stability, and greater ε_{rec} at stresses below the training stress (200 MPa). However, compared to the ECAE processed material, the thermally cycled material still had inferior functional stability at stress levels in excess of the training stress.
2. Due to a high dislocation density and nano-sized grain structure, ECAE processed $Ti_{50.5}Ni_{24.5}Pd_{25}$ exhibited increased strength leading to improved dimensional and thermal stability, at the expense of decreased transformation temperatures.
3. The selection of the right process to get enhanced functional stability for an actuator application depends on the design requirements. ECAE increases the strength of the material. Therefore, smaller cross-sections may be used to

perform the same work output without compromising functional stability. Thermal cycling gives adequate functional stability, especially under actuation stresses below the stress at which the thermal cycling took place. In addition, thermal cycling might also be utilized for applications requiring higher transformation temperatures. However thermal cycling should be performed at stresses equal or greater than the anticipated use stress.

CHAPTER VII

TRAINING AND TWO-WAY SHAPE MEMORY EFFECT OF TiNi AND TiNi BASED HIGH-TEMPERATURE SHAPE MEMORY ALLOYS

Motivated by the large TWSM strain in $Ti_{50.5}Ni_{24.5}Pd_{25}$ after a thermal cycling procedure of only 10 cycles in the previous chapter, a systematic investigation of different SMA systems was undertaken. Thermomechanical training in the form of 100 thermal cycles under various constant stress levels was employed to induce the TWSME in binary $Ti_{50.1}Ni_{49.9}$ (at. %), $Ti_{50}Ni_{29}Pt_{21}$ (at. %), $Ti_{50.5}Ni_{24.5}Pd_{25}$ (at. %) and $Ti_{50}Ni_{24.5}Pd_{25}Sc_{0.5}$ (at. %) HTSMAs. The resulting TWSME in each material was characterized in terms of its magnitude and stability.

The total residual strain generated during training was found to be indirectly related to the magnitude and the stability of the TWSME, by dictating the amount of transformable volume in the trained material, part of which was comprised of oriented martensite responsible for the TWSME. For TiNi, a negative correlation was found between the training stress and the magnitude of the resulting TWSM strain, while a positive correlation was observed for the TiNiPd based HTSMAs. The stability of the TWSME, measured by the strain changes of cold (martensitic) and hot (austenitic) shapes upon stress-free thermal cycling, was found to depend to a great extent on the temperature interval of the stress-free cycle, which would be expected to change the post-training microstructure including retained martensite and dislocation density. TiNi exhibited large degradations in cold and hot shapes, while $Ti_{50.5}Ni_{24.5}Pd_{25}$ and

$Ti_{50}Ni_{24.5}Pd_{25}Sc_{0.5}$ HTSMAs had excellent TWSME stability attractive for actuator applications. No TWSME was seen in TiNiPt due to thermal cycling at elevated temperatures, which relaxed out the favorable dislocation structures generated during training.

7.1 Experimental Methods

7.1.1 Materials

Four different material compositions were chosen for this study: conventional binary $Ti_{50.1}Ni_{49.9}$, $Ti_{50.5}Ni_{24.5}Pd_{25}$, $Ti_{50}Ni_{24.5}Pd_{25}Sc_{0.5}$ and $Ti_{50.5}Ni_{28.5}Pt_{21}$. It should be reminded that all compositions fall on the Ti-rich side of the stoichiometry so that precipitate strengthening is not an issue. TiNi was chosen to represent the baseline behavior of a conventional SMA without complications from off-stoichiometry strengthening and precipitation. $Ti_{50.5}Ni_{24.5}Pd_{25}$ was selected as an HTSMA appealing to applications requiring intermediate transformation temperatures around 200 °C. $Ti_{50}Ni_{24.5}Pd_{25}Sc_{0.5}$ has transformation temperatures about 10 °C lower compared to the ternary alloy. However, as shown in Chapter IV, this HTSMA displays an improved shape memory in the form of better dimensional stability and enhanced thermal hysteresis during isobaric cooling-heating tests. It is of interest whether these improvements will also reflect to the TWSME response. $Ti_{50.5}Ni_{29}Pt_{21}$ was chosen as the HTSMA for high-temperature applications, capable of actuation around 350 °C. Constant stress thermal cycling behavior of a similar composition, $Ti_{50}Ni_{30}Pt_{20}$ has

previously been studied by Noebe et *al.* [128] and this material exhibited good work output and dimensional stability with transformation temperatures around 300 °C.

7.1.2 Thermomechanical Training and TWSME Characterization

The choice of training procedure in order to obtain the TWSME in the currently studied materials was thermal cycling under constant stress for 100 cycles. For the TiNiPd and TiNiPdSc HTSMAs, training was carried out under tensile stresses of 80, 150 and 200 MPa on a custom-built constant-stress testing frame. 100 was selected as the number of thermal cycles, since it was expected to yield a reasonably stabilized material response with minimal changes in shape and transformation temperatures upon further thermal cycling. The three training stresses were selected as low, intermediate and high stress levels under which the samples were anticipated to successfully endure 100 cycles. Heating and cooling was done at a rate of 5 ± 1 °C/min. Samples were heated by conduction from the grips which were in turn heated by radiation through the use of an environmental furnace equipped with four 1kW halogen lamps. For cooling, water was circulated around the grips flowing through copper tubing. Temperature was controlled with a K-Type thermocouple attached to the middle of the sample gage section with a copper wire. To minimize the radiation heat transfer on the sample surface (which will lead to erroneous temperature readings that are not representative of the bulk of the specimen), the sample was shielded with a 1 mm thick reflective aluminum foil. A capacitive displacement probe (Capacitec® HPC-75) with a linear range of 0-1.5 mm

was attached to the grips to measure the displacements during the training process. Axial strain was calculated by dividing the change in length to the initial gage section length.

Following thermomechanical training, samples were unloaded and TWSME was characterized on a separate MTS testing frame for 10 stress-free cycles to assess its magnitude and stability. Strain was measured using an MTS high-temperature extensometer with a gage length of 12.7 mm and a -20/+20 % strain range. Samples were heated through conduction from the grips with heating bands. Cooling was achieved again by conduction through flowing liquid nitrogen in copper tubes wrapped around the grips. Heating and cooling rate of the samples was 10 ± 2 °C/min. Similar to the custom-built testing frame, temperature was measured using a K-type thermocouple attached to the middle of the sample gage section.

For the TiNi and TiNiPt samples, both training and TWSME characterization were performed on a MTS servohydraulic load frame. Strain was measured using an MTS high-temperature extensometer with a gage-length of 12.7 mm and a strain range of -10/20 %. Heating of the samples was achieved through the use of a 7.5 kW induction heater, while cooling was performed with a muffin fan attached to one side of the load frame. Temperature was measured with a K-type thermocouple which was spot-welded to the middle of the gage section. Samples were heated and cooled at rates of 30 ± 2 °C/min and 20 ± 2 °C/min, respectively.

7.2 Thermomechanical Training and the Evolution of Shape Memory Behavior

Figure 7.1a illustrates the typical strain vs. temperature evolution during the 100-cycle thermomechanical training procedure employed in this study. The results are for binary TiNi trained under 150 MPa. Training was initiated by loading the sample at room temperature in martensite and subsequently heating above the A_f temperature to obtain full austenite under the applied load. One thermal cycle is comprised of cooling and heating the sample through forward and reverse transformations, respectively. As a common characteristic for all trained materials, the 1^{st} cycle of the training was completed with a relatively high value of irrecoverable strain, ε_{irr}. As the number of cycles increased, the material obtained an almost stable shape memory response, demonstrating a completely different strain vs. temperature curve at the end of the 100^{th} cycle with negligible ε_{irr} per cycle. During the course of training, the material accumulated a total residual strain denoted by ε_{total}. Following training, the sample was unloaded and heated above the stress-free A_f temperature before the 1^{st} stress-free TWSME cycle, recovering the strain associated with the detwinned post-training microstructure. During TWSME cycling, a degradation in TWSME was encountered evidenced by a decrease in cold (martensitic) and hot (austenitic) shape strains (Figure 7.1b). The TWSM strain was calculated as the strain difference between the cold and hot shapes for a given stress-free cycle. The stability of the TWSME was defined as the stability of TWSM strain as well as the stability of cold and hot-shape strain values during stress-free cycling.

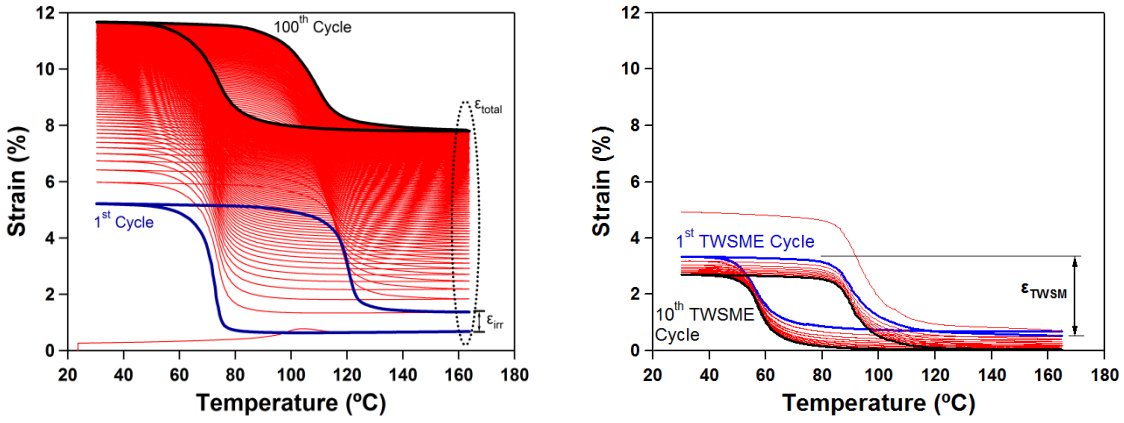

(a) (b)

Figure 7.1 (a) The illustration of the thermomechanical training procedure used in the study. The 1st and the 100th cycles are highlighted. Total irrecoverable strain, ε_{total} was measured as the sum of the irrecoverable strain per cycle, ε_{irr} of all cycles.(b) 10 stress-free TWSME cycles following training. TWSM strain, ε_{TWSM} was calculated as the the strain difference between the cold and hot shapes for a given thermal cycle.

Figure 7.2 is a compilation of the strain vs. temperature evolution curves for binary TiNi, TiNiPd, TiNiPdSc and TiNiPt during 100-cycle training under 80 MPa. In order to be able to better interpret the TWSME response of each trained material, pertinent information such as ε_{total}, recovered transformation strain (ε_{rec}) of the 1st and 100th training cycles was extracted from these results along with 150 and 200 MPa training results and tabulated in Table 7.1. (See Appendix for the strain vs. temperature evolution curves for different materials trained under 200 MPa) An investigation of 80 MPa training results showed that all materials exhibited a relatively small value of ε_{rec} at the first thermomechanical cycle, which increased by a large margin during the course of training. Highest ε_{rec} values were seen in binary TiNi throughout the training, while

TiNiPt had the lowest values. As mentioned previously, all tested materials accumulated a certain amount of ε_{total} at the end of the 100-cycle training procedure. Lowest plasticity levels were found in TiNiPd and TiNiPdSc HTSMAs, while binary TiNi showed the highest value of ε_{total}.

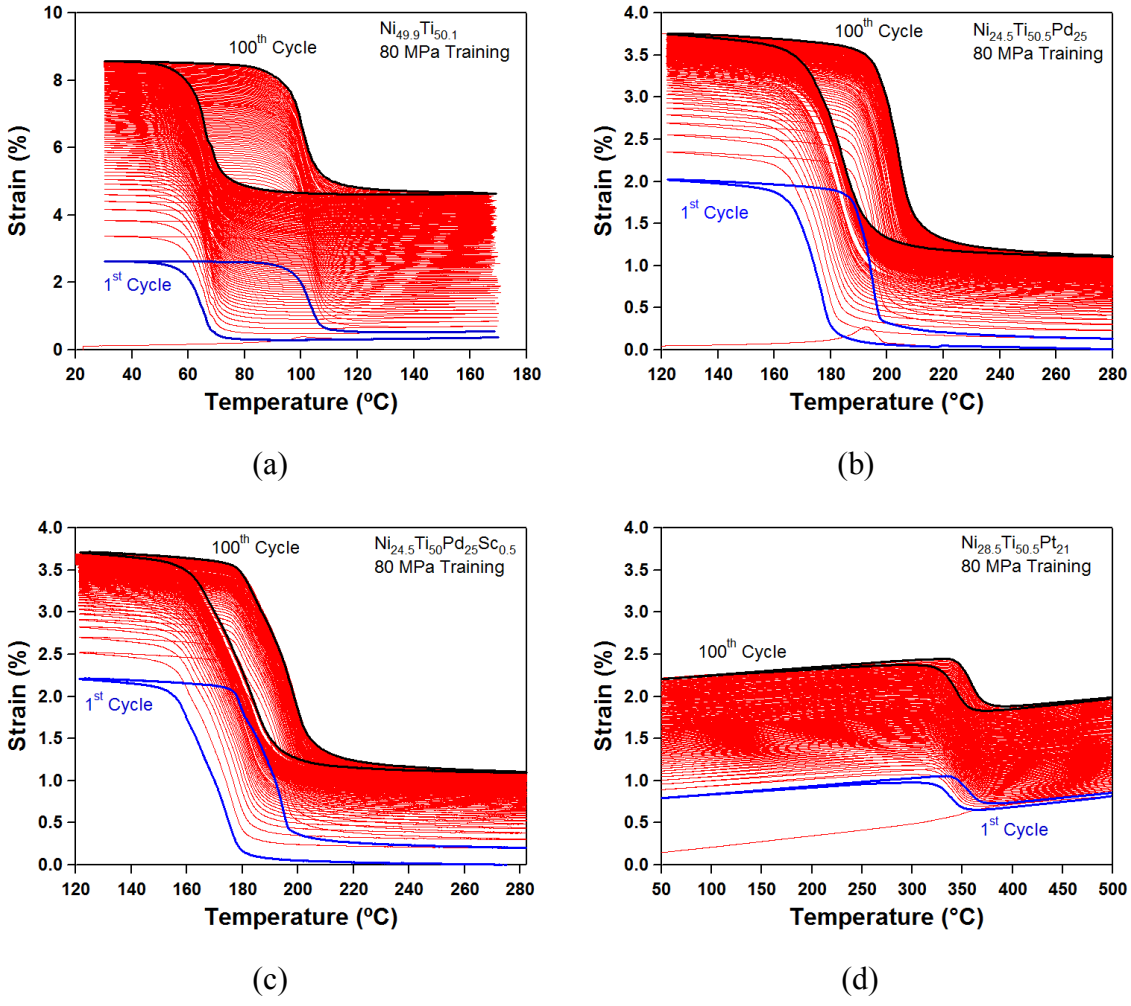

Figure 7.2 100-cycle thermomechanical training results for (a) TiNi, (b) TiNiPd, (c) TiNiPdSc and (d) TiNiPt under 80 MPa.

Table 7.1 A summary of recovered transformation strain, ε_{rec} and total irrecoverable strain, ε_{rec} levels extracted from thermomechanical training tests conducted under different stress values and using different upper cycle temperatures.

Material	Training Stress (MPa)	Training UCT (°C)	Rec Strain (ε_{rec}) 1st Cycle (%)	Rec Strain (ε_{rec}) 100th Cycle (%)	Total Irr Strain (ε_{tot}) (%)
$Ti_{50.1}$ $Ni_{49.9}$	80	165	2.04	3.68	4.29
	150	165	3.62	3.39	7.15
	150	200	3.82	3.76	12.38
	200	165	3.76	3.44	10.11
$Ti_{50.5}$ $Ni_{24.5}Pd_{25}$	80	280	1.68	2.40	1.10
	150	280	2.28	2.55	2.26
	150	320	2.43	2.73	2.36
	200	280	2.71	2.69	3.00
$Ti_{50.5}$ $Ni_{28.5}Pt_{21}$	80	500	0.32	0.55	1.17
	150	500	1.34	2.24	4.53
	200	500			
$Ti_{50}Ni_{24.5}Pd_{25}Sc_{0.5}$	80	280	1.8	2.41	1.12
	150	280	2.49	2.74	1.74
	200	280	2.73	2.75	2.80

As expected, an increasing amount of training stress led to an increased value of ε_{total} for all materials, though for a given stress, the values were larger for binary TiNi (Figure 7.3). It is also interesting to see that TiNiPt accumulated a relatively higher value of ε_{total} under 150 MPa compared to TiNiPd and TiNiPdSc, while it had almost the same ε_{total} under 80 MPa. This is most likely due to the creep deformation the material experienced under a combination of increased stress and thermal cycling at elevated temperatures. For the same reasons, this material could not endure 100 thermal cycles under 200 MPa and failed at the 60th cycle generating a ε_{total} of 8.3%.

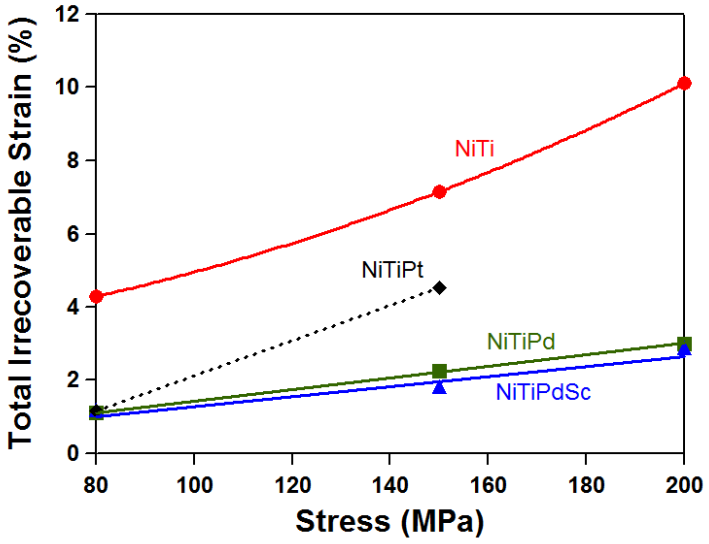

Figure 7.3 Total irrecoverable strain (ε_{total}) levels generated during thermomechanical cycling for different SMA systems studied as a function of training stress.

Figure 7.4 illustrates the evolution of the TWSME during subsequent 10 stress-free cycles (Figures 7.4a, 7.4c, 7.4e and 7.4g), as well as the changes in TWSM strain with number of cycles under different training stress levels (Figures 7.4b, 7.4d, 7.4f and 7.4h). Table 7.2 lists 1st and 10th cycle TWSM strain values; efficiency factor for each trained material, defined as the ratio between the 1st cycle TWSM strain and the ε_{rec} of the 100th training cycle; the amount of degradation in TWSM strain as well as the hot and cold-shape strain values during 10 stress-free TWSME cycles. With the exception of TiNiPt, efficiency factors for materials trained under 80 MPa were found to be quite similar around 85%, which indicated that 1st cycle TWSM strain values were very close to the ε_{rec} values of the 100th training cycle. In terms of TWSME stability, binary TiNi

demonstrated poor performance with large degradations in TWSM strain and cold and hot-shape strains during stress-free TWSME cycling. TiNiPd and TiNiPdSc HTSMAs exhibited a superior stability with less degradation in both TWSM strain and cold and hot-shape strains.

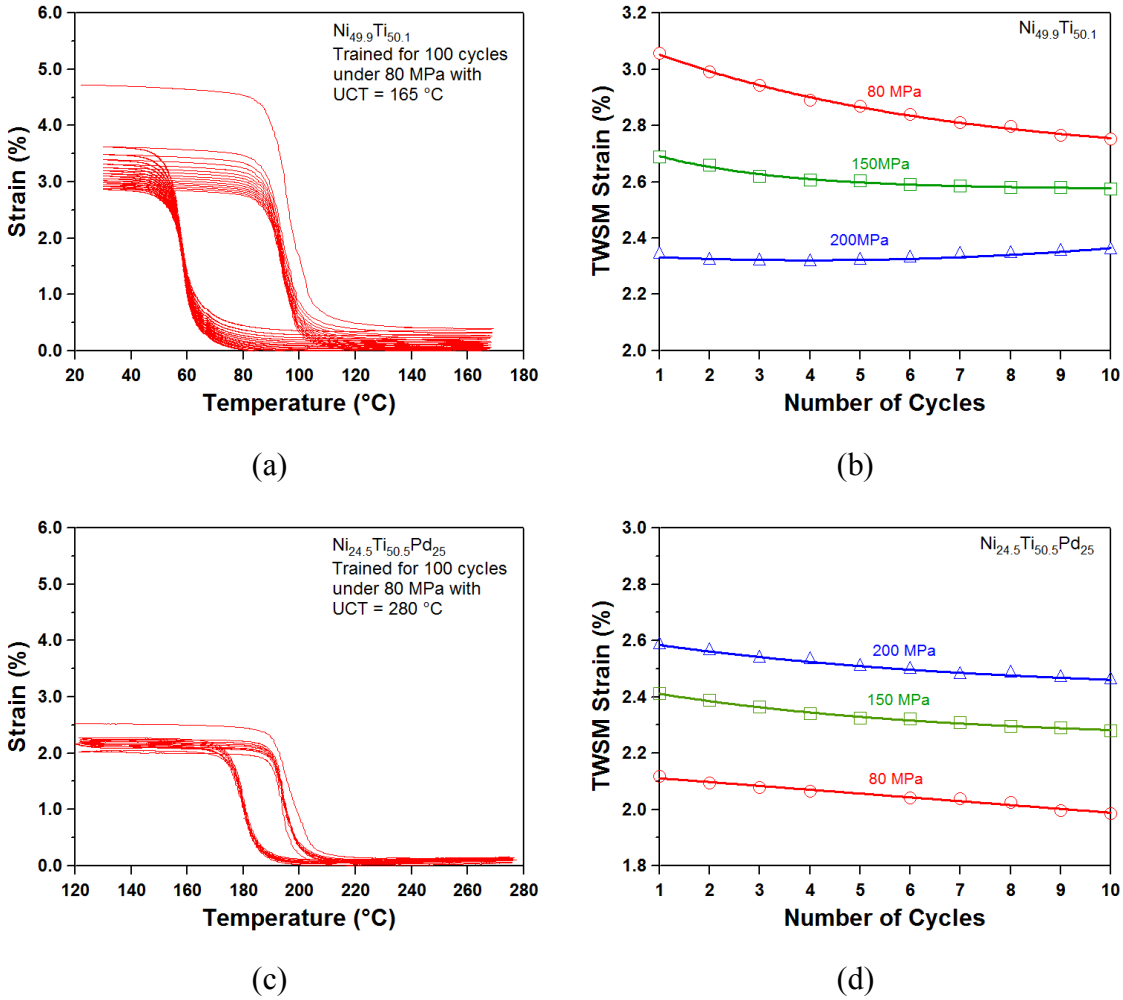

Figure 7.4 The evolution of strain vs. temperature behavior during stress-free TWSME cycling for (a) TiNi, (c) TiNiPd, (e) TiNiPdSc and (g) TiNiPt. The variation of the TWSM strain as a function of stress-free cycles for (b) TiNi, (d) TiNiPd, (f) TiNiPdSc and (h) TiNiPt.

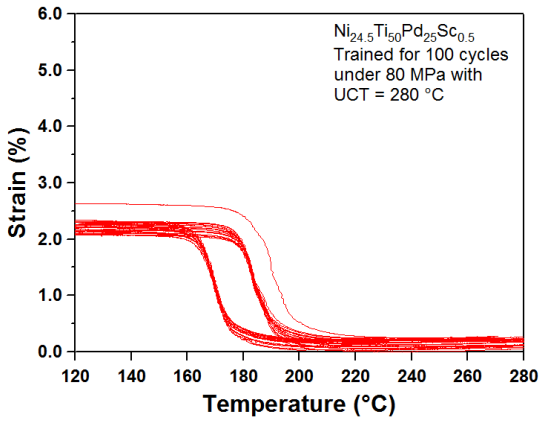

(e)

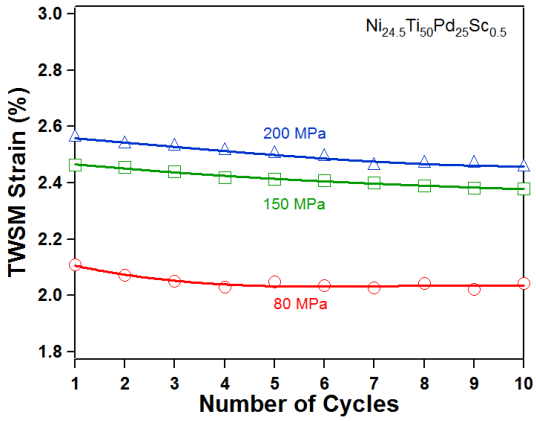

(f)

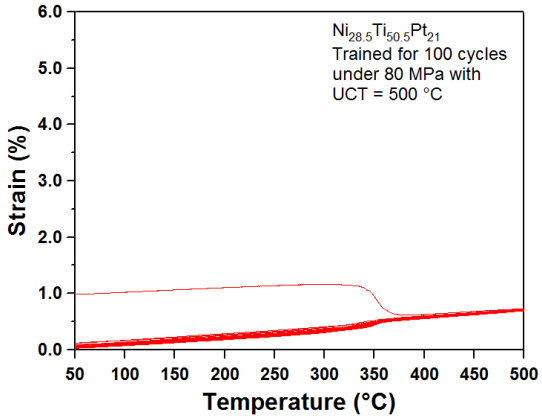

(g)

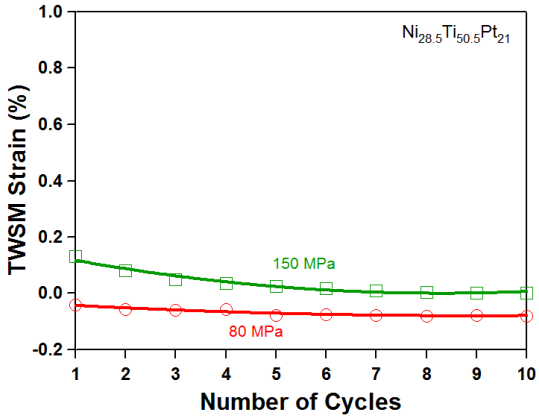

(h)

Figure 7.4 Continued.

Table 7.2 TWSME characteristics of SMA compositions after thermomechanical training under different stress levels and upper cycle temperatures (UCTs).

	Training Stress (MPa)	Training UCT (°C)	TWSME UCT (°C)	1st cycle TWSM Strain (%)	Efficiency Factor	10th cycle TWSM Strain (%)	TWSM Strain Degradation (%)	Hot Shape Degradation (%)	Cold Shape Degradation (%)
$Ti_{50.1}$ $Ni_{49.9}$	80	165	165	3.06	83.00	2.75	0.31	-0.33	-0.6
	150	165	165	2.60	76.70	2.53	0.07	-0.68	-0.64
	150	200	165	2.95	78.42	2.82	0.13	-0.46	-0.49
			200	2.43	64.59	2.09	0.34	-0.64	-0.91
	200	165	165	2.34	68.08	2.36	-0.02	-0.69	-0.58
$Ti_{50.5}$ $Ni_{24.5}Pd_{25}$	80	280	280	2.12	88.27	1.99	0.13	-0.1	-0.24
	150	280	280	2.41	94.54	2.28	0.13	-0.17	-0.31
	150	320	280	2.34	85.71	2.20	0.14	-0.13	-0.27
	200	280	280	2.58	96.07	2.46	0.13	-0.08	-0.23
$Ti_{50.5}$ $Ni_{28.5}Pt_{21}$	80	500	500	-0.04	-7.62	-0.08	0.04	-0.04	-0.09
	150	500	500	0.13	5.80	0.00	0.13	-0.03	-0.09
	200	500							
$Ti_{50}Ni_{24.5}Pd_{25}Sc_{0.5}$	80	280	280	2.11	87.66	2.04	0.07	-0.2	-0.26
	150	280	280	2.46	89.92	2.38	0.08	-0.13	-0.22
	200	280	280	2.56	93.11	2.46	0.11	-0.1	-0.22

7.2.1 Effect of Training Stress on TWSME

It is widely accepted that TWSME arises from the presence of oriented internal stress fields biasing the formation of specific martensite variants during martensitic transformation. The oriented stress field is usually imposed to the material through the presence of defects generated during thermomechanical training. As mentioned previously, some amount of irreversible strain during training cycles is necessary for the generation of TWSME, yet overstressing the material might result in an increase in the plastic deformation of the hot shape and facilitate the formation of retained martensite. This, in turn, results in a decrease in the TWSME due to a decrease in the amount of transforming volume. Thus, the question of what stress level to be used during thermomechanical training is a critical one. In addition, it is also imperative to know the differences between the low-stress and high-stress microstructures resulting in the observed differences in TWSME characteristics.

7.2.1.1 TiNi

For binary TiNi, training stress had a diverse effect on the magnitude of TWSM strain and stability of the TWSME. The magnitude of the 1st cycle TWSM strain varied inversely proportional to the training stress. Increasing training stress levels resulted in lower 1st cycle TWSM strain values (Figure 7.5b). However, with increasing training stress levels, the stability of the TWSM strain increased as evident from the small degradations in successive cycles. Upon unloading the 80 MPa-trained material and heating above the A_f temperature, more than 4% strain was recovered (Figure 7.4a).

Only 73% of this strain, about 3% was carried over to the 1st TWSME cycle but the initial TWSM strain degraded by 0.3% in 10 cycles (Table 7.2). The TWSM strain for the 150 MPa-trained material decreased from 2.6% to 2.5% in 10 cycles. The TWSM strain for the 200 MPa-trained material was found to be very stable during cycling, which actually increased slightly at the end of the 10th thermal cycle (Figure 7.4b). Of course, this is a marginal effect which could result from experimental errors. At this point, it should be noted that a stable TWSM strain is not necessarily a sign of a stable TWSME. The TWSM strain, which is calculated as the strain difference between the cold and hot shapes, might be quite stable while there is a large and equal amount of degradation in cold and hot-shape strains. On the other hand, minimal changes in cold and hot-shape strains will by definition result in a stable TWSM strain. In the case of TiNi, this material was found to display poor dimensional stability associated with the TWSME by exhibiting large changes in cold and hot-shape strains upon TWSME cycling even though the changes in TWSM strain were minor (Table 7.2). After 10 cycles, the hot-shape strain of the 200 MPa-trained material changed by 0.7% even though the magnitude of TWSM strain changed only 0.1%.

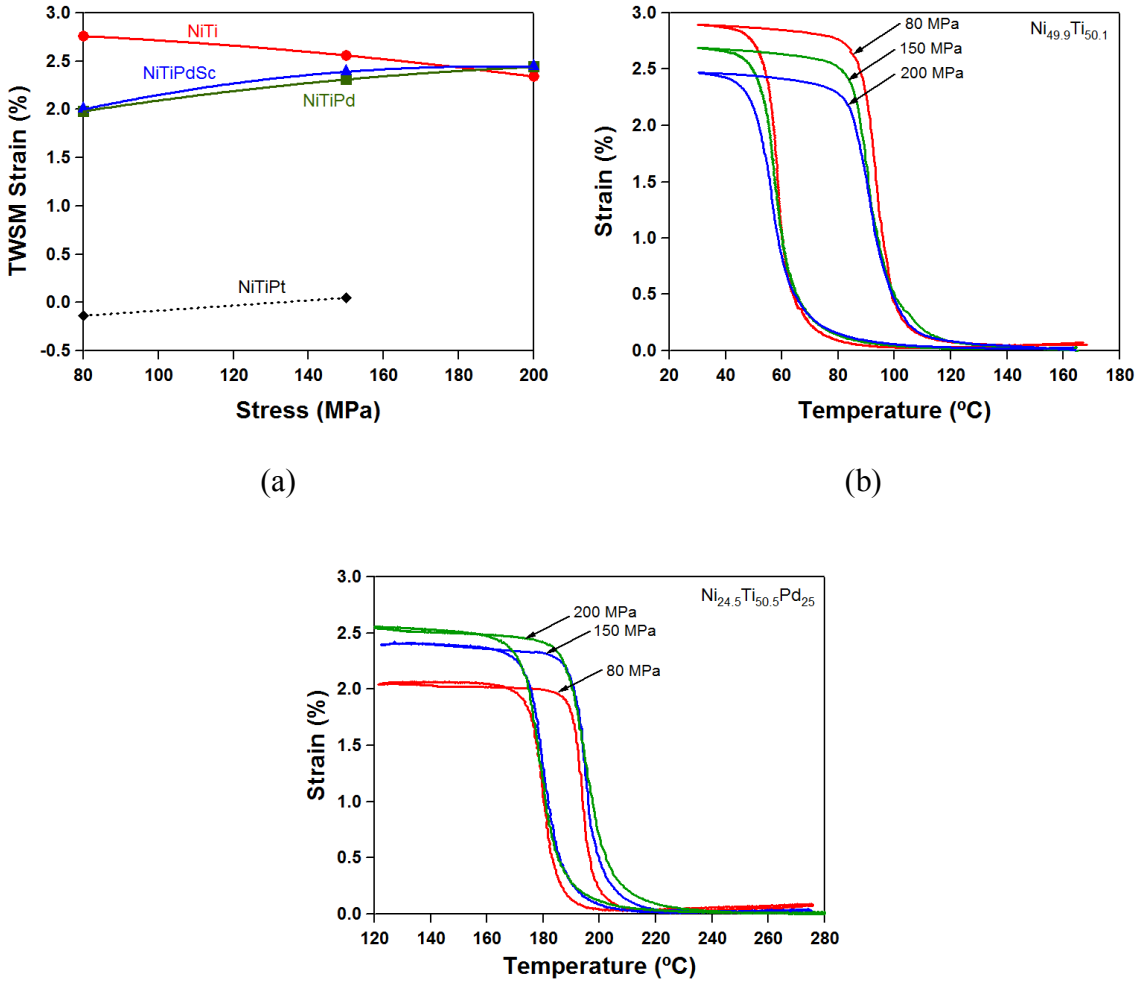

Figure 7.5 (a) TWSM strain values after 10 stress-free cycles for the tested materials as a function of training stress. 10th TWSME cycles for (b) TiNi and (c) TiNiPd after training under 80, 150 and 200 MPa.

For the 150 MPa-trained TiNi, the ε_{total} accumulated during training was around 7% (Figure 7.3). Stress-free thermal cycling altered the post-training dislocation structure in a way that each cycle caused a relaxation of the oriented internal stresses.

This inevitably caused a decrease in the cold-shape strain due to the formation of more self-accommodated martensite instead of oriented martensite (Figure 7.4a). At the end of each cycle, it was noticed that the hot-shape strain did not match the strain value of the previous cycle, i.e. there was also a decrease in the hot-shape strain. There might be several reasons responsible for the decrease in hot-shape strain upon stress-free thermal cycling. It is very likely that after a total residual deformation of 7%, there resides martensite in the structure that cannot transform to austenite [129]. One possible scenario is that the retained martensite might be of oriented type and some of this oriented retained martensite is able to revert back to austenite upon stress-free cycling resulting in a decrease in the hot-shape strain. It is also probable that due to the relaxation of the internal stress during stress-free cycling, some of the oriented retained martensite still cannot be reverted back to austenite but changes its structure to self-accommodated type. Another possible scenario is that the retained martensite in the austenitic structure might be of self-accommodated type. Upon stress-free thermal cycling, new dislocation structures will be generated to accommodate transformation shear and volume change. The stress fields of newly generated dislocations might switch some of the retained martensite to oriented type generating compressive strain upon thermal cycling. Unlike the dislocations generated during thermomechanical training which result in an increase in transformation temperatures, the new dislocation structures generated during stress-free thermal cycling decrease the transformation temperatures. Thus, although it is less likely compared to the first two scenarios, there is still possibility that some of the self-accommodated retained martensite might be converted

to compressive strain generating oriented retained martensite. In the end, the net effect after 10 stress-free thermal cycles is a relative increase in the volume fraction of self-accommodated martensite which brings about a 0.1% degradation in TWSM strain.

TWSME behaviors of 80 MPa and 200 MPa-trained TiNi can be described based on the same scenarios. The notable difference between these conditions is the amount of ε_{total} generation during training. This difference definitely brings about different amounts of retained martensite and dislocation densities in the trained materials, which alter the volume fraction of oriented martensite variants giving the TWSME. For instance, the peculiar TWSM behavior of the 200 MPa-trained material, i.e. stable TWSM strains upon cycling, can be attributed to a recovery of a large volume fraction of retained martensite. For this material, the decrease in the hot-shape strain was actually larger compared to the decrease in the cold-shape strain, resulting in an increasing TWSM strain.

7.2.1.2 TiNiPd(Sc)

Unlike TiNi, increasing training stresses resulted in higher oriented internal stresses without significant plasticity for TiNiPd HTSMA. Compared to TiNi, much lower ε_{total} values were recorded at the end of training under all stress levels. While a ε_{total} of 1.1% was accumulated at 80 MPa training, this value doubled to 2.3% when the training stress was increased to 150 MPa. Under 200 MPa, ε_{total} was found to be 3.0%. Higher internal stresses without significant plastic deformation led to increasing TWSM strains with increasing training stress levels. Furthermore, TWSM strains of trained

TiNiPd HTSMAs were found to be very close to the maximum recoverable strain levels under stress, exhibiting high training efficiencies (Table 7.2). It should be stated that the efficiency values increased for TiNiPd HTSMA with increasing training stress levels, while opposite behavior was seen in binary TiNi.

In terms of TWSME stability, cold and hot-shape strains of TiNiPd were very stable and changed minimally upon stress-free thermal cycling (Figure 7.4c). The strain recovered during the initial heating of the 150MPa-trained material above the A_f temperature was very close to the 1st cycle TWSM strain. Out of the 2.9% strain recovered, 83%, 2.4%, was carried over to the subsequent TWSME cycles. Unlike TiNi, the amount of TWSM strain increased with increasing training stress and its degradation levels were around 0.1 % at the end of 10 stress-free thermal cycles for all training stress levels. In terms of stability of the TWSME, TiNiPdSc displayed very similar results to TiNiPd, with slightly improved TWSM strain and hot and cold-shape strain stability (Table 7.2).

7.2.1.3 TiNiPt

High transformation temperatures of TiNiPt necessitated thermal cycling at elevated temperatures to observe the TWSME. Heating of the 80 MPa-trained sample above the A_f temperature resulted in a strain recovery of 0.5% (Figure 7.4g), which is almost the same as the ε_{rec} of last training cycle (Table 7.2). Further stress-free cycling, however, did not yield any useful TWSM strain. At the end of 10 stress-free thermal

cycles, the TWSM strain of TiNiPt was almost non-existent regardless of the training stress.

Although TiNiPt exhibited good shape memory behavior during training cycles with reasonable recoverable and residual strains, it did not show TWSME behavior due to the required temperature interval for thermal cycling. Regardless of the training stress used during 100 thermal cycles, the first consecutive stress-free cycle up to 500 °C erased almost all the beneficial dislocations giving the TWSME (Figure 7.4g and 7.4h).

7.2.2 Effect of Alloying Additions on TWSME

The most obvious change in the TWSME characteristics between the various SMA compositions is the change in transformation temperatures. Figure 7.6 shows the 10^{th} TWSME cycles for all materials previously trained under 150 MPa. Substitution of 25 at. % Pd with Ni increased the transformation temperatures of TiNi to 200 °C. Quaternary alloying addition of Sc to TiNiPd decreased its transformation temperatures about 10 °C, consistent with the isobaric thermal cycling test and differential scanning calorimetry (DSC) analysis results of shown in Chapter IV. Pt increased the transformation temperatures of TiNi higher per unit of alloying addition compared to Pd: addition of 21% Pt raised the transformation temperatures of TiNi so high (around 350 °C) that, in the temperature range of transformation, the dislocations necessary for the TWSME were annealed out in the initial TWSME cycles regardless of the training stress. This resulted in a significantly low TWSM strain. Noebe *et al.* [130] have already shown that recovery processes begin at 450 °C and end around 600 °C in a

$Ni_{29.5}Ti_{50.5}Pt_{20}$ HTSMA. It thus remains a technological challenge to obtain stable TWSME response in HTSMAs when high transformation temperatures close to recovery/recrystallization temperatures are involved.

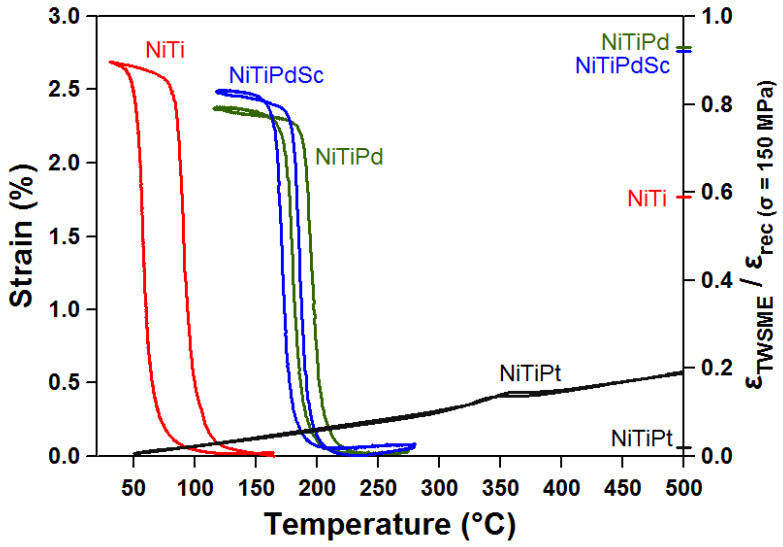

Figure 7.6 Effect of alloying additions to TiNi in terms of the TWSME. The materials have been previously trained under 150 MPa for 100 thermal cycles.

Substitution of Pd with Ni did not only increase the transformation temperatures of the TiNi. Pd also acted as a solid-solution strengthener and converted the monoclinic, B19' martensite structure of TiNi to orthorhombic B19, resulting in improved compatibility between transforming phases (cubic, B2 austenite transforming to orthorhombic martensite instead of monoclinic martensite). As a result of improved crystallographic compatibility coupled with increased strength levels, a much more

stable thermomechanical cycling response compared to that of binary TiNi, evidenced by smaller ε_{total} values during training under all stress levels (Figure 7.3) and smaller changes in cold and hot-shape strains during TWSME cycles (Figure 7.5c), was obtained even though the sample was cycled to a higher UCT. Due to same reasons, there was also a decrease in energy dissipation during transformation, contributing to a significant reduction of the thermal hysteresis in both training and TWSME cycles.

Microalloying with Sc further improved the compatibility of transforming phases in TiNiPd and increased the material strength again due to the solid-solution strengthening effect. As a result, TiNiPdSc had slightly smaller thermal hysteresis compared to TiNiPd during both training and TWSME cycles. Recently, the second eigenvalue, λ_2 of the transformation stretch tensor that maps the austenite lattice to the martensite lattice, has been related to the thermal hysteresis associated with the martensitic transformation [81]. It has been stated that as the λ_2 value gets closer to 1, compatibility between transforming phases increases, leading to a smaller thermal hysteresis. Current results for the λ_2 of binary TiNi (0.9663) [120], TiNiPd (1.0171) and TiNiPdSc (1.0158) (Section 4.2.1) are consistent with this finding for the thermal hysteresis associated with the TWSME, as well.

In terms of two-way shape memory (TWSM) strain, TiNi exhibited a higher value at the end of 10 TWSME cycles compared to TiNiPd and TiNiPdSc. However, when the TWSM values were normalized with respect to the highest amount of recoverable strain that could be obtained from each material at a stress level of 150 MPa, it was seen that TiNiPd and TiNiPdSc HTSMAs outperformed TiNi with values very

close to 1 (Figure 7.6). This indicates that for a specific thermomechanical treatment procedure, TiNiPd based HTMSAs of this study respond to training more efficiently and have nearly perfect TWSME relative to the load-biased behavior during training. A high value of training efficiency indicates that dislocation structures and local stress fields generated by cycling are very effective in biasing the orientation of the martensite variants, which form during subsequent thermal cycling under zero stress [49]. On the other hand, TiNiPt had a value close to 0, indicating that this material is not suitable for TWSME within the specified thermal cycling temperature range.

It should also be noted that although the TWSME cycles are conducted under stress-free conditions, the transformation temperatures associated with these cycles are relatively higher compared to the transformation temperatures of the untrained conditions. This is due to the internal stresses generated during thermomechanical training which decrease the amount of undercooling needed to initiate and complete the transformation.

7.2.3 Effect of Training Upper Cycle Temperature (UCT) on TWSME

It is commonly accepted that for a chosen SMA system, transformation strains generated during thermomechanical training are quite representative of the resultant TWSM strain. Any training parameter that can potentially increase the ε_{rec} of the last training cycle will most likely increase the TWSM strain of the following stress-free cycle. However, as previously seen in the previous section, the evolutionary behavior of TWSM strain might differ between different SMA systems. While ε_{rec} is a function of

applied stress, it is also significantly affected by the UCT the material is exposed to. This is because the magnitude of the CSS to activate martensite reorientation, in addition to being dependent on different crystallographic planes, decreases with increasing temperatures. Similarly, a high UCT value also triggers true plasticity and TRIP due to the decrease in CSS for slip. On the other hand, higher UCT values may help reduce the amount of martensite retained at the end of each reverse transformation cycle due to overheating. It is thus imperative to know what kind of effects UCT selected during thermomechanical training has on the resultant TWSM behavior.

The choice of UCT during thermomechanical training was done in such a way to ensure complete transformation under the applied stress. Since all materials have different transformation temperatures, different UCT's were used during training. TiNi was thermally cycled up to 165 °C, whereas TiNiPd and TiNiPdSc were cycled up to 280 °C and TiNiPt was heated up to a temperature of 500 °C. Padula *et al.* [131] has already demonstrated that UCT affects the thermomechanical response of TiNi under isobaric thermal cycling consisting of a relatively low number of thermal cycles. They have shown that the material cycled using a higher UCT exhibited higher transformation strains under all stress levels. It is of interest whether similar responses will be seen upon a relatively higher number of thermal cycles and how the resulting TWSME will differ using different values of UCTs. To meet this objective, TiNi and TiNiPd alloys were trained using two different UCT values under 150 MPa. TiNi was cycled up to a UCT of 165 °C and 200 °C, while TiNiPd was cycled up to a UCT of 280 °C and 320 °C.

7.2.3.1 TiNi

Strain vs. temperature response of TiNi during thermomechanical training under 150 MPa is shown in Figures 7.7a and 7.7b with UCT's of 165 °C and 200 °C, respectively. At a first glance, it is noticed that ε_{total} generated during training increased from 7.2 % to 12.4 % due to an increase of UCT from 165 °C to 200 °C. There are similarities in the evolutionary responses of these two cases. For both materials, the 1st training cycle is characterized by a relatively large thermal hysteresis and ε_{irr}. During the course of training, due to the introduction of oriented dislocation structures, there was both a hardening effect on the material and a domination of microstructure with increasingly more single-variant martensite instead of self-accommodated martensite. The consequences of these phenomena are double-fold. First, the material started to show a more stable behavior characterized by smaller shifts in transformation temperatures during cycling and smaller values of ε_{irr} per cycle. Second, the interaction between martensite variant pairs was diminished, leading to smaller dissipation of elastic stored energy during transformation, resulting in a smaller thermal hysteresis value. There are also subtle differences between these two cases in terms of ε_{rec} and temperatures. If the 100th cycle is compared to the 1st cycle for the 165 °C UCT case, it is noticed that ε_{rec} decreased from 3.6% to 3.4%. For the 200 °C UCT case, ε_{rec} remained quite stable at 3.8 % during 100 cycles. Compared to the material trained with a UCT of 165°C, the 100th cycle of the material trained with a UCT of 200 °C had noticeably higher ε_{rec} and transformation temperatures. This can be seen from the initial heating curves preceding the 10 stress-free TWSME cycles (Figures 7.7c and 7.7d). As true

plasticity was expected to be more prominent at higher UCT values leading to a reduced transforming volume, the higher transformation strain of the 200 °C UCT case could only be explained with the retained martensite. While a higher UCT results in higher values of ε_{total} during training, the amount of retained martensite was diminished compared to the lower UCT case, evidenced by the increased ε_{rec}.

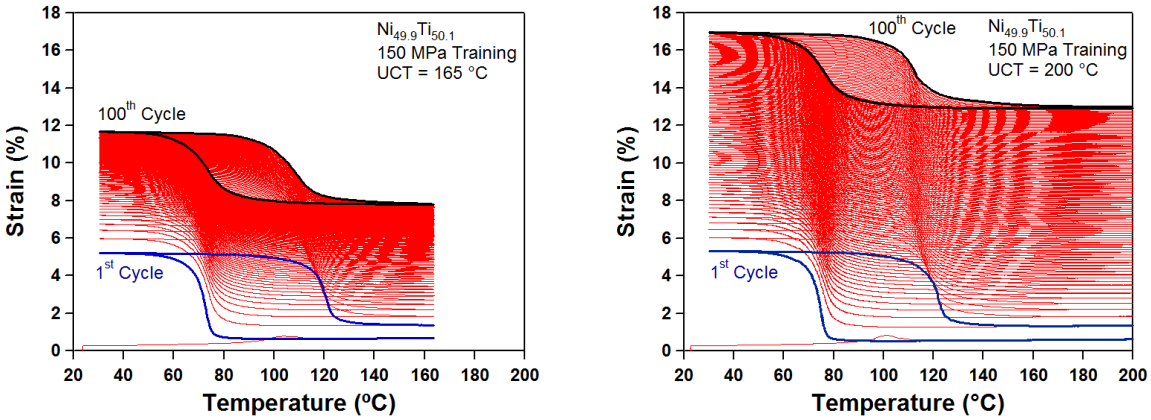

(a) (b)

Figure 7.7 The evolution of strain vs. temperature response of TiNi trained under 150 MPa using a UCT of (a) 165°C and (b) 200 °C. The evolution of the TWSME during the consequent 10 stress-free cycles for the material trained with UCT of (c) 165 °C and (d) 200 °C. (e) A comparison of 10th stress-free TWSME cycles of the materials trained with different UCTs.

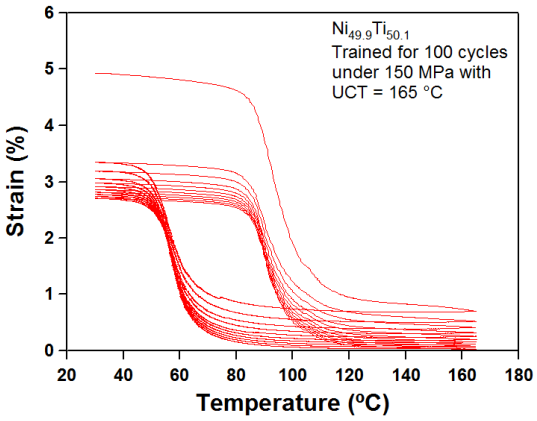

(c)

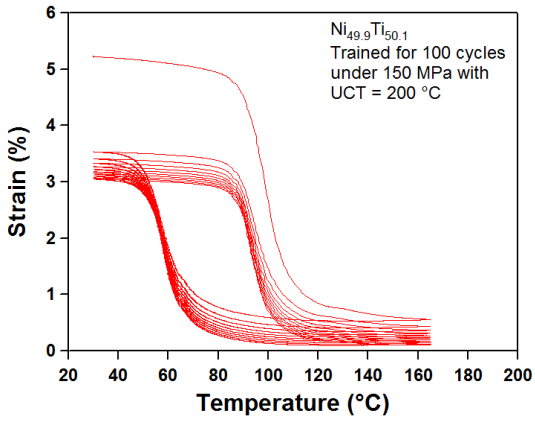

(d)

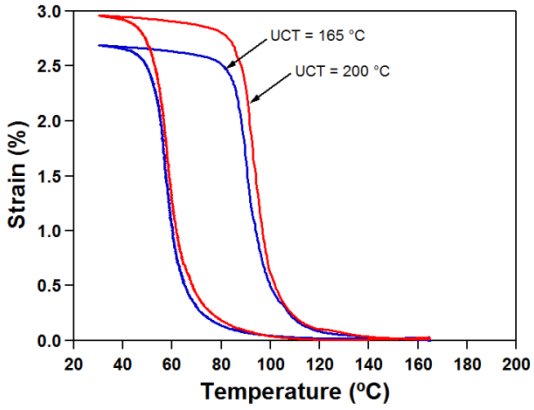

(e)

Figure 7.7 Continued.

The TWSME obtained from these two cases were different in terms of stability and magnitude. Unlike the effect of increased training stresses, a higher value of ε_{total} as a result of higher UCT yielded a higher initial TWSM strain value of 3.0 % in TiNi (Figure 7.7d). The degradation levels associated with cold and hot-shape strains were also different. After 10 TWSME cycles, the material trained with a UCT of 165 °C

exhibited a TWSM strain of around 2.5 % (Figure 7.7e) with about 0.7 % degradation in both hot and cold-shape strains (Figure 7.7c). Figure 7.7d illustrates the TWSM response for the same material trained with a UCT of 200 °C. Compared to the material trained with a UCT of 165 °C, the degradation levels are lower about 0.2 % in both hot and cold-shape strains resulting in a TWSM strain of 2.8 % at the end of 10 TWSME cycles. Larger degradation of the cold-shape strain in the 165 °C UCT trained material is probably due to larger relaxation of internal stresses and thus the substitution of more self-accommodated martensite with oriented martensite. As it was mentioned previously, the larger dislocation density in the 200 °C UCT trained material due to a ε_{total} of 12.4 % is likely to hinder the relaxation of internal stresses in this material, leading to an improved TWSME stability. Smaller degradation in the hot-shape of the 200 °C UCT trained material is possibly associated with the smaller amounts of retained martensite present in the microstructure that can revert back to martensite during transformation.

7.2.3.2 TiNiPd(Sc)

Contrary to TiNi, a 40 °C increase in the UCT used during training of TiNiPd caused only 0.2% difference in ε_{total} levels (Table 7.1). The sample which was thermally cycled under 150 MPa using a UCT of 280 °C had a ε_{total} of 2.3 % (Figure 7.8a), while the same thermomechanical training with a UCT of 320 °C resulted in a ε_{total} value of 2.4% (Figure 7.8b). When the 1^{st} and 100^{th} cycles are investigated for both cases, it is noticed that the evolution of strain vs. temperature responses are hardly affected by the choice of the UCT. Unlike TiNi, the 1^{st} and 100^{th} cycles are very comparable for both

cases in terms of ε_{rec} and thermal hysteresis. This is an indication of the conservation of the transforming volume during the training procedure without significant generation of retained martensite and plasticity. In addition, both materials have around 16 °C shift in transformation temperatures during the course of training compared to the 7 °C shift in TiNi, which shows the existence of larger oriented residual stresses assisting the transformation.

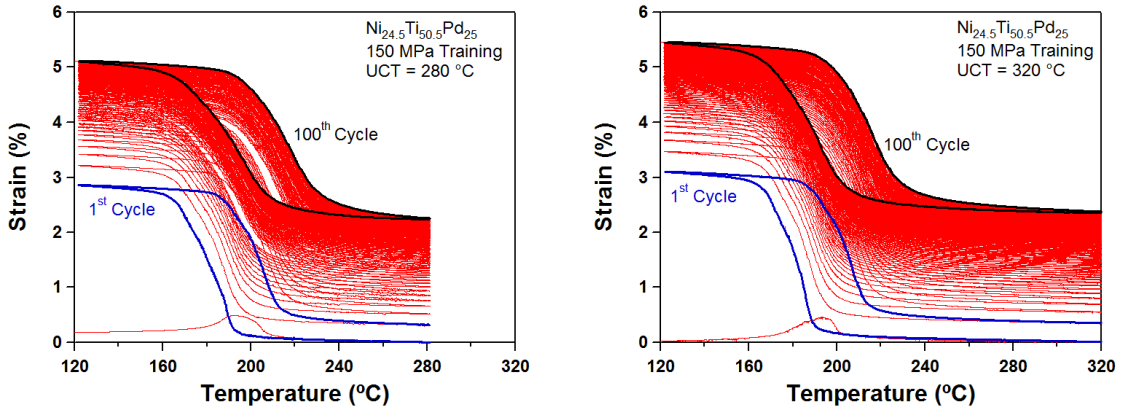

(a) (b)

Figure 7.8 The evolution of strain vs. temperature response of TiNiPd trained under 150 MPa using a UCT of (a) 280°C and (b) 320 °C. The evolution of the TWSME during the consequent 10 stress-free cycles for the material trained with UCT of (c) 280 °C and (d) 320 °C. (e) A comparison of 10th stress-free TWSME cycles of the materials trained with different UCTs.

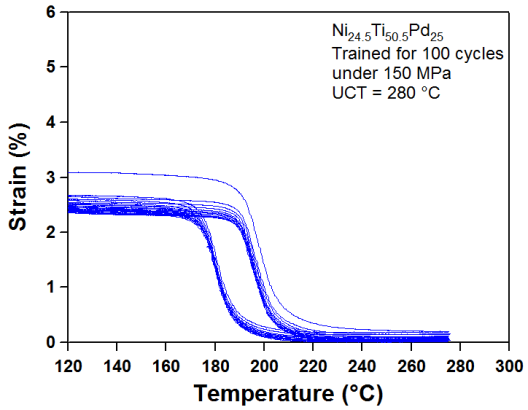

(c)

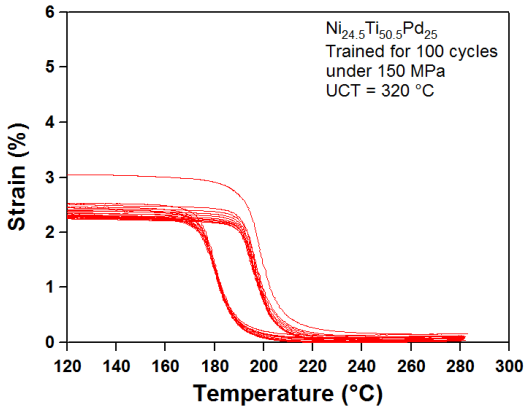

(d)

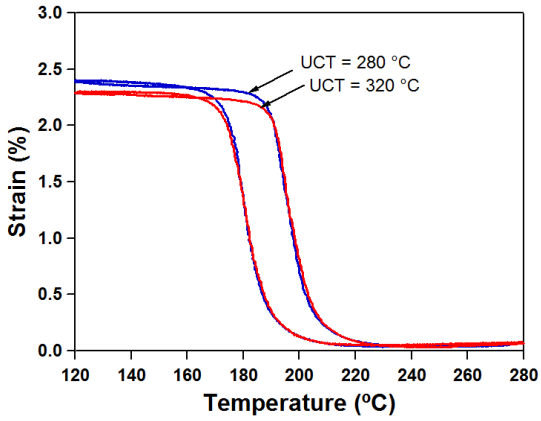

(e)

Figure 7.8 Continued.

The initial heating curves after the training procedure follow almost the same path for the two cases (Figure 7.8c and 7.8d) indicating similar values of internal stresses in both materials. In the same way, the changes in cold and hot-shape strains are indistinguishable. Both materials have minimal amounts of degradation in hot and cold-

shape strains compared to TiNi. The 10th stress-free TWSME cycle for each case is shown in Figure 7.8e. The two strain vs. temperature curves fall almost on top of each other with identical transformation strain, hysteresis and temperatures. The 0.1% difference in TWSM strain of the 10th stress-free cycles might be a result of 0.2% extra plastic deformation during training with a UCT of 320 °C.

7.2.4 Effect of TWSME Cycling Upper Cycle Temperature (UCT) on TWSME

In the previous section, the effect of UCT selection has only been demonstrated for the thermomechanical training cycles. The selection of UCT for the stress-free TWSME cycles deserves equal attention. To show the effect of UCT in TWSME cycling on the stability and magnitude of TWSME, binary TiNi which has been trained under 150 MPa using a UCT of 200°C, was stress-free cycled using also a UCT of 200 °C, instead of 165°C. It was shown that a higher UCT used during stress-free cycling severely affected both the magnitude and the stability of TWSME. Out of the 3.8% ε_{rec} recorded in the last training cycles, only 2.4% could be carried over to the 1st TWSME cycle (Table 7.2). The TWSM strain decreased by 0.3% in 10 cycles and the largest degradation in cold-shape strain was seen among all other conditions, which was undoubtedly due to the rapid relaxation of oriented internal stresses.

7.2.5 Mechanisms Responsible for the Magnitude and Stability of TWSME

In order to better explain the following results, a schematic is presented overviewing the parameters effective in the magnitude and stability of TWSME (Figure

7.9). The amount of ε_{total} generated as a result of training is primarily dictated by training stress. For all tested materials, ε_{total} increases with increasing training stress (Figure 7.3). Other training parameters that can affect the outcome of ε_{total} are the number of thermal cycles and the UCT. The effect of number of cycles on the TWSME was not investigated in this study, since it was kept constant at 100.

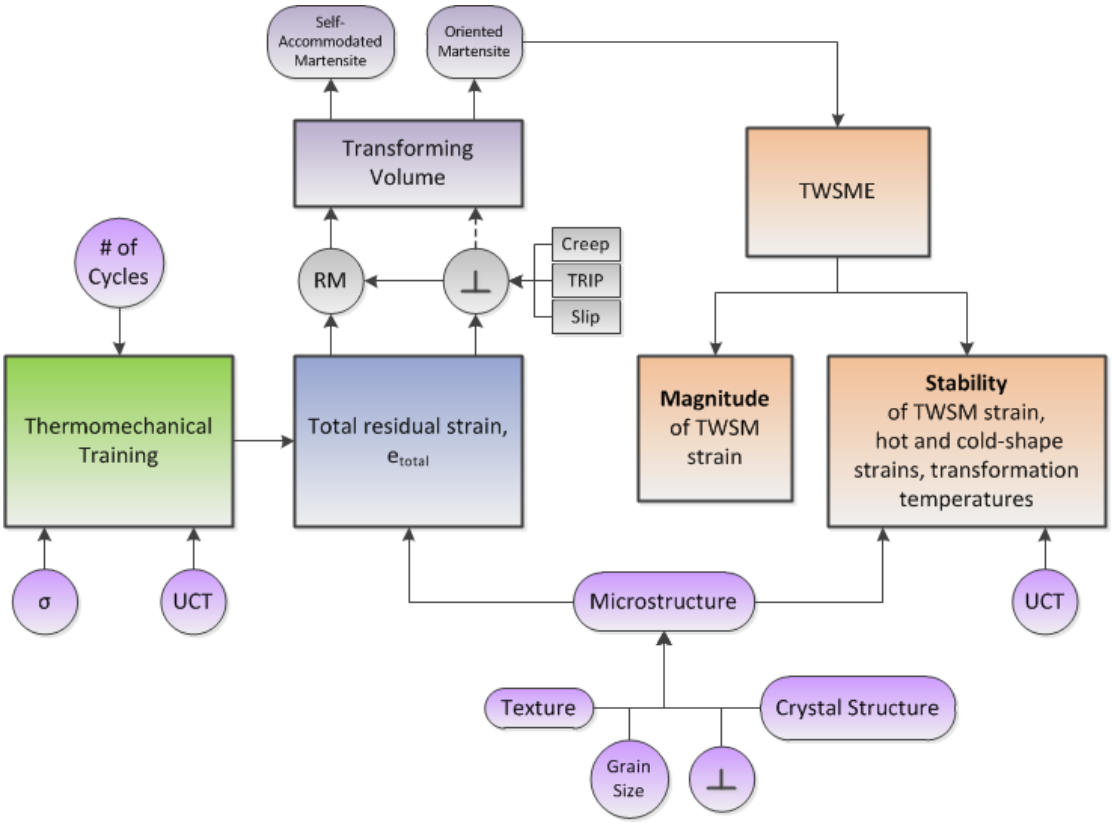

Figure 7.9 Schematic showing the parameters involved in the generation of TWSME, its magnitude and stability.

ε_{total} might be partly due to dislocation structures or retained martensite that cannot revert back to austenite during transformation. Several factors play roles during the generation of dislocation structures such as true plastic deformation (slip) and TRIP. In addition, effects of creep deformation cannot be overlooked during thermal cycling at high temperatures as seen in the TiNiPt case. Obviously, microstructural features such as compatibility, texture, grain size and initial dislocation density also contribute to the manifestation of ε_{total}. Higher strength levels through finer grain size, higher initial dislocation density or preferred orientations as well as improved crystallographic compatibility between transforming phases might decrease defect generation during training, resulting in low values of ε_{total}. However, for the sake of simplicity, the effects of these microstructural parameters on the TWSME are beyond the scope of this study.

The combination of retained martensite and dislocation structures determine the amount of transforming volume available after training. It should be emphasized that there might exist interplay between martensite stabilization and generation of dislocation structures during training, i.e. dislocations might assist in the stabilization process. Thus, a horizontal arrow is used to establish a connection between retained martensite and dislocation structures. On the other hand, it is not exactly known how dislocation structures contribute to the amount of transforming volume. Therefore, the connection between dislocation structures and transforming volume has been shown with a dashed arrow. Due to the presence of oriented internal stresses and/or retained martensite, a fraction of the transforming volume will be comprised of oriented martensite which is responsible for the TWSME and directly controls the magnitude of the TWSM strain.

Stress-free TWSME cycling of the trained material might cause rearrangement and annihilation of the dislocation structures generated during training. It may also assist in the reverse transformation of the retained martensite in the structure. At the same time, new dislocation structures might also be generated hindering subsequent transformations. Microstructural characteristics and the selection of UCT during stress-free cycling have a strong influence on these phenomena. The combined effect of these competing mechanisms is a change in the volume fractions of oriented and self-accommodated martensite. Depending on the relative amounts of both martensite structures, the magnitude of the TWSM strain and the stability of the TWSME are subject to change during stress-free TWSME cycling.

7.3 Summary and Conclusions

In this chapter, TiNi SMA and TiNiPt, TiNiPd and TiNiPdSc HTSMAs were characterized in terms of their TWSM behaviors. The TWSME was induced in these materials through a thermomechanical training procedure consisting of 100 thermal cycles under various stress levels with different UCTs. Stability of the TWSME was assessed by running 10 stress-free thermal cycles following the training cycles.

A summary of the results and some of the conclusions that could be derived from this chapter are:

1. The total residual strain generated during thermomechanical training was indirectly related to the magnitude and stability of the TWSME. It dictated the amount of transformable volume in the trained material, part of which was

comprised of oriented martensitic variants responsible for the TWSME. Residual strain was controlled by microstructural features such as the strength of the material and the compatibility between transforming phases. At the same time, it varied directly proportional to the training stress and the UCT.

2. Trained under 150 MPa, TiNi exhibited a TWSM strain of 2.5% at the end of 10 stress-free cycles. This value was about 60% of the strain recoverable from the same material under stressed conditions. On the other hand, both TiNiPd and TiNiPdSc HTSMAs had much more efficient responses to training. These alloys had TWSM strain values around 2.4%, which corresponded to almost 90% of the recoverable strain that could be obtained from these materials under 150 MPa thermal cycling. Stress-free cycling annealed out all the favorable dislocation structures in TiNiPt due to the inherently high transformation temperatures of this HTSMA, negating the TWSME.
3. In terms of stability, a TWSME with minimal strain changes in the hot (austenite) and cold (martensite) shapes and the magnitude of the TWSM upon stress-free cycling is sought for actuator applications. The mechanism for the degradation of TWSME was explained through a retained martensite & dislocation structure based scenario. TiNi exhibited poor TWSME stability evidenced by large degradations in cold and hot-shape strains upon stress-free thermal cycling. TiNiPd and TiNiPdSc had superior stability levels characterized by minimal shape changes.

4. Both UCT and stress selections for the thermomechanical training have been demonstrated to have significant effects on the outcome of TWSME. UCT deserves extra attention since it also has to be selected carefully for stress-free TWSME cycling. A higher UCT value during stress-free cycling was found to result in a faster degradation of the TWSME.
5. TiNiPd based HTSMAs have been shown to be attractive candidates for TWSME applications. These alloys built up relatively small amounts of residual strains during thermomechanical training, regardless of the selection of UCT and stresses. The resultant TWSME was shown to have excellent stability of hot and cold-shape strains with adequate TWSM strain.

CHAPTER VIII

WORK OUTPUT OF THE TWO-WAY SHAPE MEMORY EFFECT IN $Ti_{50.5}Ni_{24.5}Pd_{25}$ HIGH-TEMPERATURE SHAPE MEMORY ALLOY

If the TWSME is intended to be utilized for actuation purposes, its stability under stress is a major concern since most of the emerging actuator applications require the HTSMA to do work against a load. Thus, there is a need to characterize these HTSMAs in terms of the stability of TWSME during repeated actuation and investigate methods to enhance the stability.

TWSME was induced in $Ti_{50.5}Ni_{24.5}Pd_{25}$ HTSMA through the same training procedure employed in the previous chapter. Stability of the TWSME was characterized during both stress-free thermal cycling and thermal cycling under stress. In addition, isobaric cooling-heating tests were conducted to assess the work output of the TWSME under different stress levels. The effects of SPD on the stability and work output of the TWSME were also studied by training a sample processed with ECAE.

Although outstanding TWSME stability was achieved during stress-free thermal cycling, large degradations were recorded during thermal cycling under stress. ECAE processing did not have a remedial effect on these large degradation levels and UCT was anticipated as the primary parameter responsible for the instabilities.

8.1 Thermomechanical Training

Figure 8.1 shows the strain vs. temperature responses of as-received and ECAE processed samples during the 100-cycle training under 150 MPa. Both materials were thermally cycled to 280 °C to ensure complete reverse transformation while preventing any differences in response that could be attributed to different UCTs. The UCT was shown to significantly influence the evolution of shape memory characteristics, particularly the level of irrecoverable strain that develops, during load-biased thermal cycling of equiatomic TiNi [132].

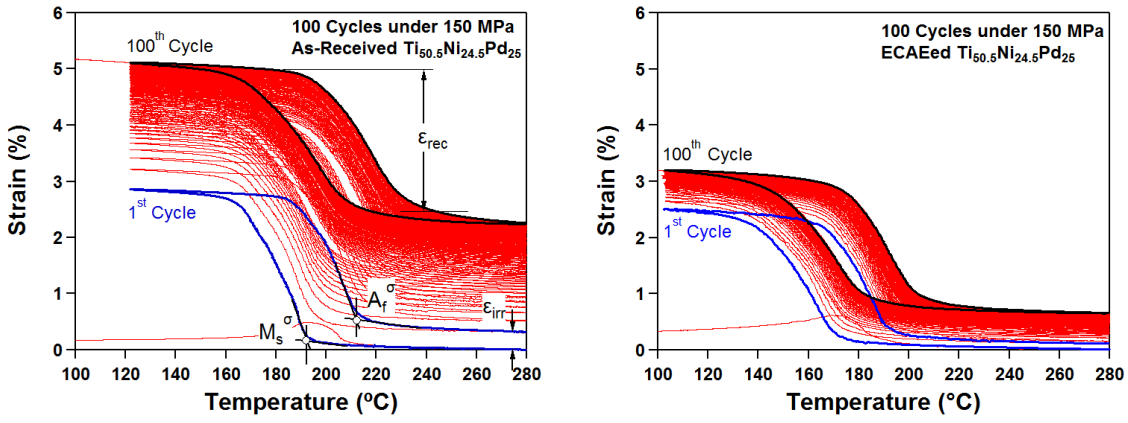

(a) (b)

Figure 8.1 Comparison of strain vs. temperature evolution during the 100-cycle thermomechanical training under 150 MPa for the (a) as-received and (b) ECAE processed $Ti_{50.5}Ni_{24.5}Pd_{25}$. Recovered transformation strain (ε_{rec}), irrecoverable strain (ε_{irr}), martensite start (M_s^{σ}) and austenite finish (A_f^{σ}) temperatures are illustrated in (a).

Both materials exhibited a similar evolution of the shape memory response during training. The first cycle was characterized by a relatively high value of irrecoverable strain, ε_{irr}. Each subsequent cycle induced fewer defects, until a level of functional stability, with negligible ε_{irr}, was achieved at the end of 100 cycles. For the as-received material, ε_{irr} decreased from 0.31 % during the first cycle to 0.01 % at the end of 100 cycles, whereas for the ECAE processed material, the decrease was from 0.10 % to 0.01 %. Hence, the total irrecoverable strains accumulated during training were 2.25 % and 0.65 % for the as-received and ECAE processed $Ti_{50.5}Ni_{24.5}Pd_{25}$, respectively. These results are not surprising since it has already been reported that ECAE improves functional stability during repeated thermomechanical cycling as a result of grain refinement and work hardening [75]. But these same processes also inhibit the amount of recoverable strain that can be generated because they result in a more homogenous nucleation of self-accommodative martensite variants with increased interaction between the variants compared to nucleation and propagation of a few preferred martensite variants as in the case of the hot-extruded material. Another result of ECAE processing was the decreased number of training cycles required to reach a certain level of stability (Figure 8.1b) compared to the as-received condition. However, by the end of 100 cycles, the final levels of irrecoverable strain were quite similar for both materials. Therefore, even though as-extruded $Ti_{50.5}Ni_{24.5}Pd_{25}$ takes longer to reach a stable condition compared to ECAE processed material, both materials ultimately reach the same level of dimensional stability, while a much greater level of recoverable strain is achieved in the as-received condition. Furthermore, this level of stability is

greater in the $Ti_{50.5}Ni_{24.5}Pd_{25}$ alloy and achieved sooner compared to binary TiNi thermomechanically cycled under similar conditions (Figure 7.7a).

In addition to the evolution of ε_{irr}, there were also notable changes in thermal hysteresis (ΔT), recovered transformation strain (ε_{rec}) and transformation temperatures during the course of training. ΔT increased from 23 °C to 25 °C for the as-received material, while it remained constant at 24 °C for the ECAE processed material. Transformation temperatures (M_s^σ) of both materials increased, indicating that the internal stress fields generated due to the applied stress favored the formation of martensitic variants. M_s^σ of as-received TiNiPd increased from 192 °C to 210 °C in 100 cycles, while M_s^σ of the ECAE processed material increased from 172 °C to 183 °C. For both materials, there was also an increase in ε_{rec} as a result of training. The smaller ε_{rec} of the ECAE processed sample can be explained by the difficulty of reorienting martensitic variants, i.e. higher stresses are needed for the ECAE processed sample to reorient the same amount of martensite. In 100 cycles, the 2.23 % recoverable strain increased by 0.27 % for the as-received material, while for the ECAE processed material, the 2.09 % initial ε_{rec} increased by 0.21 %.

8.2 Stability of the TWSME during Stress-Free Thermal Cycling

Following training, samples were unloaded and heated above the stress-free austenite finish temperature, $A_f^{\sigma=0\ MPa}$. During this heating process, a relatively large strain recovery took place which is associated with the reverse transformation of the detwinned post-trained martensite (Figure 8.2). Following this initial no-load cycle, 10

stress-free thermal cycles were performed to assess the stability of the TWSME that was developed due to training.

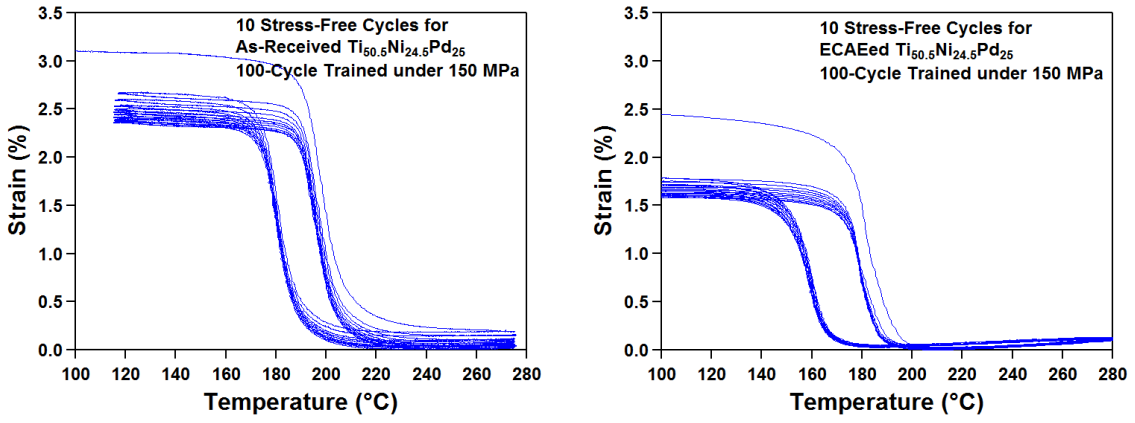

(a) (b)

Figure 8.2 Ten stress-free thermal cycles for the (a) as-received and (b) ECAE processed $Ti_{50.5}Ni_{24.5}Pd_{25}$ performed after 100-cycle, 150 Pa training demonstrating the magnitude and stability of the TWSME.

It was observed that both materials displayed good TWSME stability during stress-free thermal cycling. However, there is still some degradation in TWSME for both materials evidenced by a decrease in martensitic (cold) and austenitic (hot) shape strains. In 10 stress-free cycles, the cold and hot-shape strains of the as-received material decreased by 0.31 % and 0.18 %, while a superior behavior was observed in the ECAE processed material, evidenced by 0.20 % and 0.03 % decreases, respectively. These results are in good agreement with similar work done on $Ni_{49.7}Ti_{50.3}$ (at.%) SMA by

Scherngell *et al.* [133], who showed that an increased dislocation density inhibited the degradation of TWSME during stress-free cycling.

The TWSM strain was calculated as the strain difference between the cold and hot-shape strains for a given stress-free cycle. This strain is reported to be highly related to the recoverable transformation strain, ε_{rec} of the last training cycle [49], which is consistent with the current results. For the as-received material, ε_{rec} of the last training cycle was 2.50 %, while the TSWM strain during the first stress-free cycle was 2.38%. For the ECAE processed material, ε_{rec} during the last training cycle was 2.28%, while the TWSM strain during the first no-load cycle was 1.65%. In terms of magnitude, these values are very close to the ε_{rec} values that could be obtained from these materials under stress-assisted conditions prior to training. For instance, 2.48 % ε_{rec} can be obtained from the as-received material under 150 MPa (Figure 4.7a), while this value is 1.95 % for the ECAE processed material. This indicates the efficiency of the training procedure employed in this study and the response of the $Ti_{50.5}Ni_{24.5}Pd_{25}$ to the training in general.

The stability of the TWSM strain was determined by comparing the TWSM strain at the first and tenth no-load cycles. For the as-received $Ti_{50.5}Ni_{24.5}Pd_{25}$ the TWSM strain decreased from 2.47 % to 2.34 % in 10 cycles, while the decrease was from 1.65 % to 1.48 % for the ECAE processed material. For both materials, this represents about a 10% loss in TWSM strain capability after 10 cycles.

8.3 Work Output of the TWSME

One of the most important characteristics of an SMA actuator is the work output, which is the product of ε_{rec} and applied stress during a thermal cycle. As shown in Figure 8.2, the trained samples exhibited TWSME by contraction and extension during reverse and forward transformations, respectively. If compressive stresses are applied to the samples during forward transformation, work may be done by the TWSME. To quantify the work output of TWSME, isobaric cooling-heating tests were conducted under different opposing compressive stresses. Both as-received and ECAE processed samples, which have previously been trained under 150 MPa and subsequently undergone 10 stress-free cycles were loaded in compression in 25 MPa increments, starting at 0 MPa (Figure 8.3a and 8.3b). As-received materials trained for 100 cycles under 80 and 200 MPa were also tested to assess the effect of training stress on the work output capability of the TWSME developed under different training conditions. At each stress increment, samples were thermally cycled through full transformation while recording the strain vs. temperature response. Loading was done to 75 MPa, at which point the TWSME was almost suppressed for the as-received materials and completely suppressed for the ECAE processed material, suggesting the level of internal stress generated during training, at least in the uniaxial direction, was greater in the as-received material compared to the ECAE processed material. Furthermore, the as-received material maintains its greater transformation strain at all stress levels compared to the ECAE processed material, resulting in a much greater work output as summarized in Figure 8.3c.

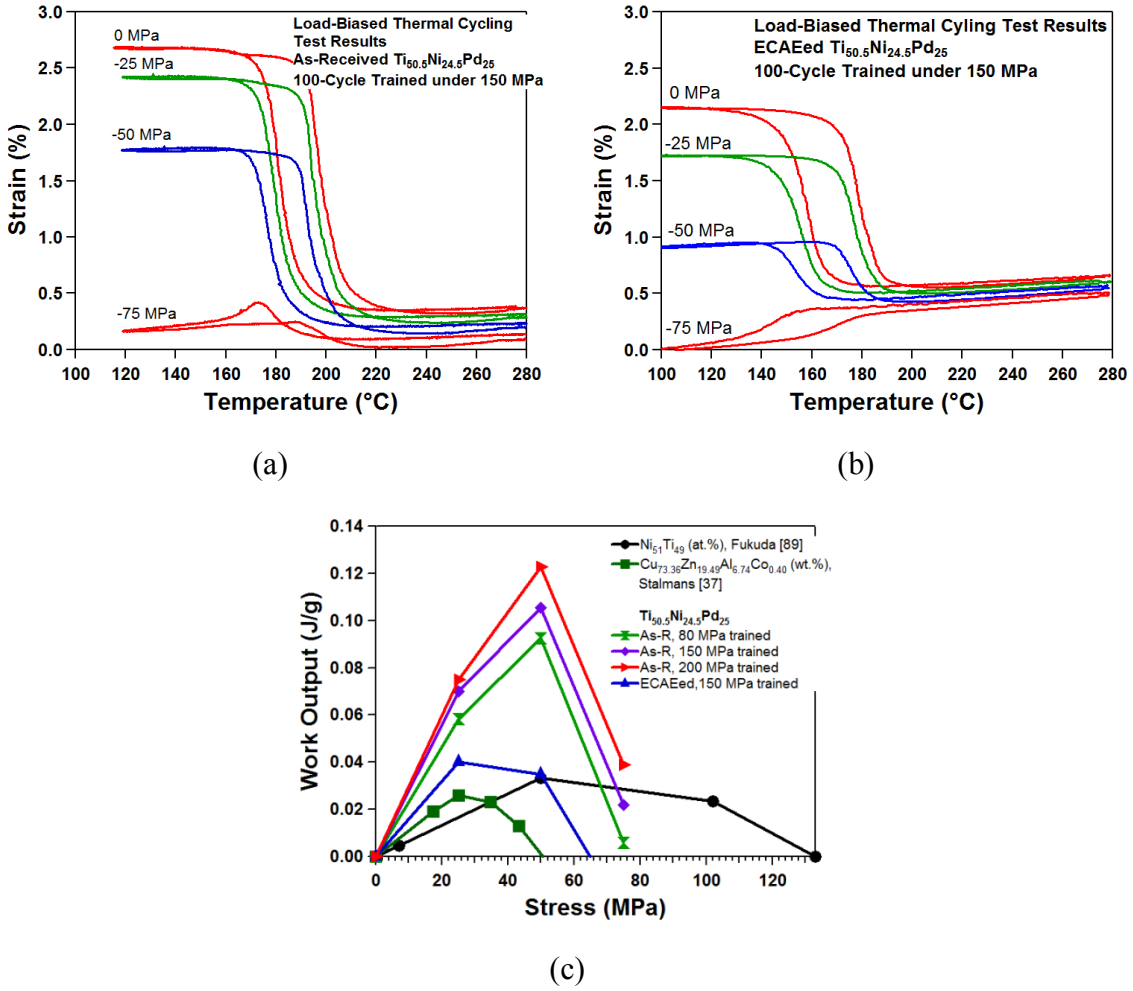

Figure 8.3 Load-biased thermal cycling test results for the (a) as-received plus trained and (b) ECAE processed and trained $Ti_{50.5}Ni_{24.5}Pd_{25}$ performed after 10 stress-free thermal cycles. Samples were loaded under different compressive stress levels to assess the work output of the TWSME. (c) A comparison of the work output values for the as-received and ECAE processed $Ti_{50.5}Ni_{24.5}Pd_{25}$ trained under different stress levels, as well as the work output levels for a binary TiNi [91] and Cu-based SMA [37].

Figure 8.3c is a compilation of work output results obtained from isobaric cooling-heating tests performed on the $Ti_{50.5}Ni_{24.5}Pd_{25}$ HTSMA after various training conditions, along with data from the literature for other systems [37, 91]. If the work

output is defined as $W_{TWSME} = \frac{\sigma_{OPP}\varepsilon_{TWSM}}{\rho}$, where σ_{OPP} is the opposing compressive stress, ε_{TWSM} is the TWSM strain obtained under σ_{OPP} and ρ is the density (taken as 7.532 g/cc for $Ti_{50.5}Ni_{24.5}Pd_{25}$) , it is clearly seen in Figure 8.3c that W_{TWSME} increased with increasing training stress for the as-received material. W_{TWSME} values reaching 0.12 J/g could be obtained from the as-received $Ti_{50.5}Ni_{24.5}Pd_{25}$ under appropriate training conditions. These values are substantially high compared to the reported TWSME work output values for TiNi [91] and Cu-based SMAs [37], which are also shown in Figure 3.c. However, the work output for the TWSME is still less than what can be achieved under a biased OWSME, which is 0.491 J/g and 0.743 J/g of work for $Ti_{50.5}Ni_{24.5}Pd_{25}$ under 150 and 200 MPa bias stresses, respectively.

In hindsight, it is not surprising that the as-received material has superior TWSM characteristics compared to the ECAE processed material. During isobaric cooling-heating experiments, preferred variants of martensite are formed during cycling that will maximize the recoverable strain during transformation. The purpose of training, which is nothing more than repeated isobaric cooling-heating experiments, is to develop an internal stress state through the generation of dislocations and other defects, which stabilizes this group of preferred martensite variants during the transformation process. In essence, training stabilizes the martensite formation path, so even without the external applied stress this same path is followed [37]. The as-received material is superior to the ECAE processed material because it starts out as a clean slate. It has a relatively low defect density, as it was hot extruded and relatively dislocation free, and therefore

training is free to imprint a particular transformation path with variants that can undergo maximum recoverable strain. The ECAE processed material, on the other hand, already has a significant density of dislocations resulting from the SPD processing and also a refined grain size. This internal stress state would favor a more random selection and greater percentage of self-accommodative martensite variants with greater chance for interaction and less capability to carry strain. Training then serves to reinforce this more self-accommodative transformation path resulting from the original ECAE processing. Thus, the variants that are stabilized in the as-received material carry much greater strain than those reinforced in the ECAE processed material due to the refined grain size and prior work already present in the latter material. The recoverable strain levels developed in the two materials (as-received vs. ECAE processed) after training and resulting magnitude of the TWSME, which approaches the recoverable strain developed during training support this argument. Thus, the lesson learned is that the magnitude of the TWSME is maximized by training a material that is initially internally stress free, with few prior dislocations, defects, or coherent precipitates rather than starting with a material that already contains some structure.

8.4 Stability of the TWSME during Thermal Cycling under Stress

It should be emphasized that work output levels reported in the previous section were single cycle measurements. For a reliable implementation in actuator applications, the response of the TWSME during repeated thermal cycling under stress should be determined. To achieve this goal, following the isobaric cooling-heating tests, 10

thermal cycles under 50 MPa compressive stress were performed to assess the stability of the TWSME while performing work. Figure 8.4a and 8.4b show the results of these tests for the 150 MPa trained as-received and ECAE processed material, respectively.

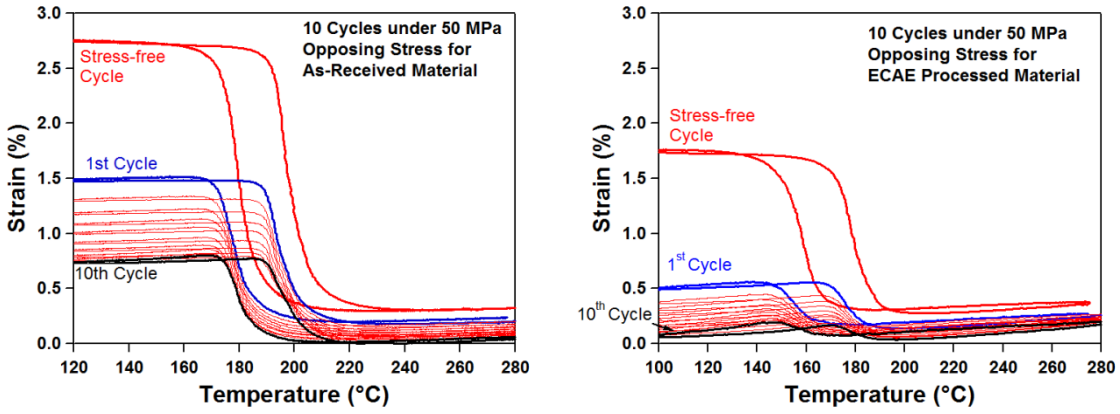

(a) **(b)**

Figure 8.4 Strain vs. temperature evolution during 10 thermal cycles under 50 MPa compressive stress for the (a) as-received and (b) ECAE processed $Ti_{50.5}Ni_{24.5}Pd_{25}$ to assess the stability of TWSME while doing work.

Both materials showed a rapid degradation in TWSM strain as evidenced by the large changes in cold-shape strains. The amount of overheating above $A_f^{\sigma=50\ MPa}$ temperature might play a role in this unforeseen behavior, i.e. ECAE processed sample had to be overheated by roughly an extra 25 °C under each stress level to reach to the same UCT.

Although ECAE resulted in a superior TWSME stability during stress-free thermal cycling, it did not have the same effect on the stability of the TWSME work

output. In only 10 thermal cycles, the TWSM strain of the as-received sample dropped from 1.3 % to 0.8 %. The hot-shape strain of the ECAE processed sample remained quite stable, but the cold-shape strain degraded significantly, reducing the TWSM strain from 0.4 % to 0.1 %. The amount of overheating above A_f^{σ} temperature and the higher dislocation density expected in the ECAEed sample (Figure 5.2b) might play a role in this unforeseen behavior, i.e. ECAE processed sample had to be overheated by roughly an extra 25 °C under each stress level to reach to the same UCT and this may cause easier relaxation of the oriented internal stress due to higher dislocation density.

8.5 Effect of Upper Cycle Temperature on the Stability of TWSME

In order to show the effect of UCT on the TWSME stability, an ECAE processed sample was trained under the same conditions, except this time using a lower UCT of 240 °C. All the subsequent thermomechanical characterization tests including 10 stress-free thermal cycles (Section 8.2), isobaric cooling-heating test under compressive stresses (Section 8.3) and 10 thermal cycles under 50 MPa compressive stress (Section 8.4) were also carried out using this lower UCT value. The results of these tests are illustrated in Figure 8.5.

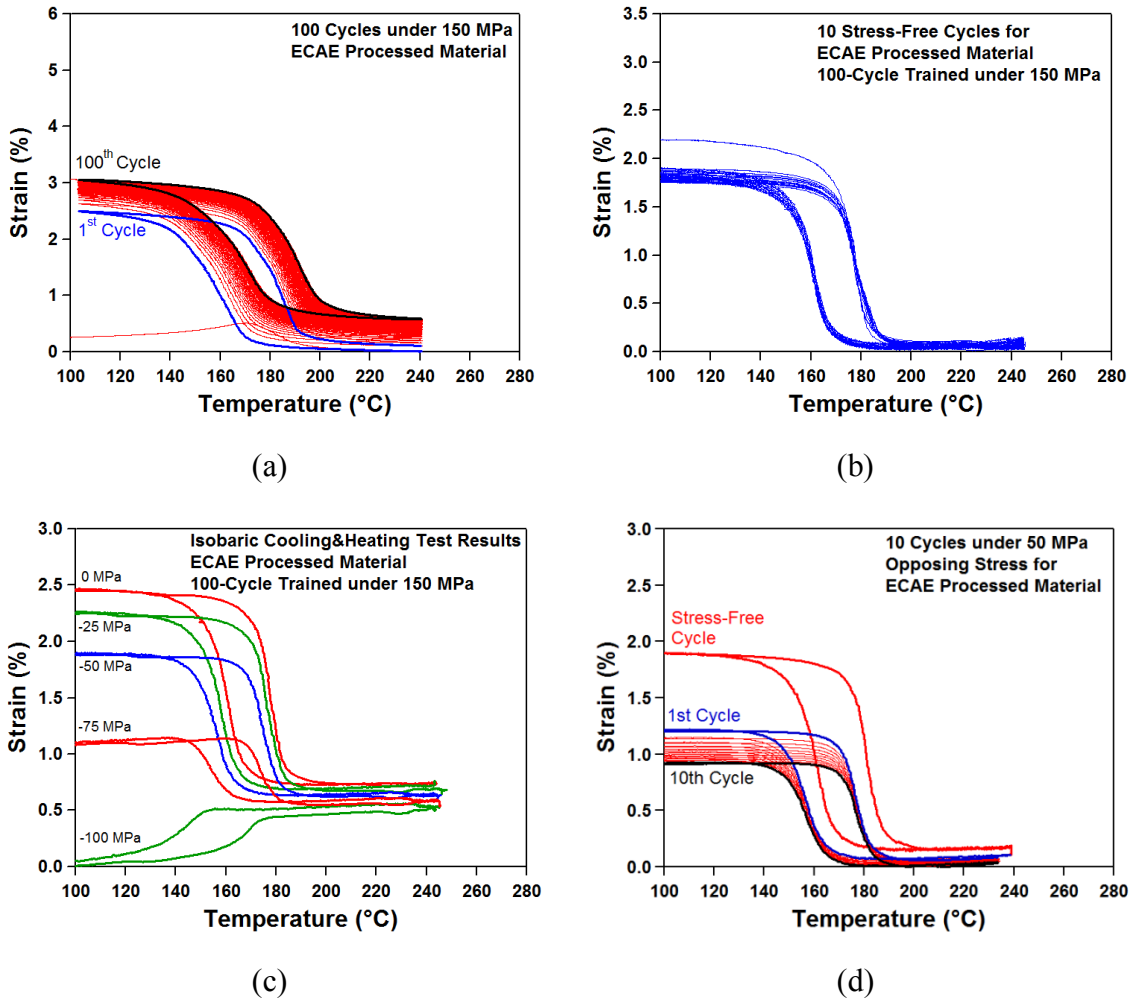

Figure 8.5 Repeating of the thermomechanical characterization tests for the ECAE processed sample at a lower UCT of 240°C. (a) 100-cycle thermomechanical training under 150 MPa, (b) 10 stress-free thermal cycles, (c) isobaric cooling-heat test under various compressive stresses and (d) 10 thermal cycles under 50 MPa compressive stress.

A 40 °C decrease in the UCT barely affected the evolution of shape memory characteristics during training (Figure 8.5a). First cycle ε_{irr} remained unchanged at 0.10 %, while the total irrecoverable strain decreased from 0.65 % to 0.58 %. The change in other shape memory properties, such as ΔT, ε_{rec} and transformation temperatures

followed a similar trend as described in Section 8.1 with slightly different values. ΔT stayed constant at 25 °C, while M_s^σ increased from 171 °C to 181 °C. ε_{rec} of the first cycle was found to be 2.13 % and increased to 2.23 % at the end of 100 cycles.

The functional stability during stress-free thermal cycling was also marginally affected by the lower UCT choice. Cold-shape strain decreased by 0.13 %, while hot-shape strain decreased by 0.06 %, resulting in a TWSM strain degradation from 1.76 % to 1.66 % in 10 cycles. Nevertheless, the stability of the TWSME work output was significantly increased when a lower UCT was used during thermal cycling. The amount of opposing stress required to fully suppress the TWSME increased, leading to larger overall work output levels (Figure 8.5c). In addition, the degradation of the TWSME during thermal cycling under a constant stress level significantly decreased (Figure 8.5d).

8.6 Summary and Conclusions

In this chapter, $Ti_{50.5}Ni_{24.5}Pd_{25}$ HTSMA was subjected to a training procedure consisting of 100 thermal cycles under different stress levels (i.e., 80, 150, and 200 MPa). The resulting TWSME was characterized in terms of its stability during both stress-free and load-biased thermal cycling. The effect of ECAE on the stability of the TWSME was also studied. Major findings and conclusions that can be drawn from this study are as follows:

1. TWSME could resist moderate opposing stresses, resulting in a maximum external work of 0.12 J/g after training under 200 MPa. This level of work output

was significantly higher than that attributed to a TWSME developed in conventional TiNi and Cu-based SMAs. A maximum work output for the TWSME was achieved at an opposing stress of approximately 50 MPa, regardless of the training stress used to develop the TWSME. Additional increases in stress beyond this peak resulted in a substantial degradation in the TWSM strain and consequently work output of the TWSME. In the as-received material an opposing stress of greater than 75MPa was necessary to suppress the TWSME.

2. The effect of ECAE prior to training on the magnitude and stability of the TWSME was also studied. A stable TWSME with small degradations in cold and hot shape-strains upon stress-free thermal cycling was obtained, but due to the nature of the training and the already induced defect structure in the ECAE processed-material, the magnitude of the resulting transformation strain and work output generated by the TWSME effect was far less than that developed in the as-received material. Another reason for this might be the larger overheating above the A_f^{σ} temperature used during the thermal cycling of the ECAE processed material and easier relaxation of the internal stresses due to the heavily deformed microstructure.
3. The stability of TWSME during stress-free thermal cycling was not reflected to the stability under stressed conditions. For both as-received and ECAE processed materials, the cold-shape strains decreased considerably upon repeated thermal

cycling under a constant opposing stress, leading to large degradations in TWSM strains.

4. Similar to the conclusion made in the previous chapter, UCT was demonstrated to have a major role on the outcome of the TWSME stability during both stress-free and load-biased thermal cycling. A higher UCT value was shown to result in faster and larger degradation of the TWSME in the ECAE processed material.

CHAPTER IX

INFLUENCE OF MICROSTRUCTURE ON THE EVOLUTION OF SHAPE MEMORY BEHAVIOR DURING THERMOMECHANICAL TRAINING

The previous two chapters investigated the stability and work output of the TWSME in trained SMAs. The evolution of shape memory behavior during thermomechanical training is equally important as the characterization of the trained material. Most SMAs display a similar evolution of shape memory behavior during training. Transformation temperatures, hot and cold-shape strains change considerably in the early cycles, the amount of change decreasing with number of cycles. Eventually, an almost stable behavior is obtained upon which further cycling results in only minor changes in transformation temperatures and hot and cold-shape strains. Since conventional training procedures are long and costly, it is desired that the trained SMAs reach stability in as few cycles as possible.

The objective of this chapter is to explain the role of microstructural parameters, with a special focus on the crystallographic compatibility between transforming phases, on the response of SMA to training. The influence of training parameters such as applied stress or UCT has to some extent been investigated in previous chapters and is also covered in the literature. With an understanding of the role of the microstructural parameters on evolutionary load-bias behavior, the material behavior during training can easily be predicted. This will greatly help in choosing the right SMA composition for a

specific application and choosing the right training parameters to obtain stability in as few cycles as possible.

9.1 Evolution of Shape Memory Behavior during Training

One interesting phenomenon observed from the thermomechanical training tests covered in both Chapter VII and Chapter VIII was that although materials reached stability in a similar number of thermal cycles, the saturation value of ε_{irr} per cycle during training, at a given applied stress level, was not equal to zero. This indicated that most of the microstructural evolution took place during the early cycles, but there was still a finite amount of defect generation upon transformation at the end of 100 cycles, which was found to be different for different alloy systems. Since λ_2 was previously associated with defect generation and thus the appearance of thermal hysteresis, it was reasonable to question whether λ_2 might also have an influence on this phenomenon.

In order to validate this hypothesis, λ_2 values of all thermomechanically trained materials in Chapter VII, as well as a slightly Ni-rich TiNiPd composition were measured using XRD analysis. The goal was to determine whether a correlation existed between the λ_2 values and the saturation values of ε_{irr} per cycle from thermomechanical training tests under different stress levels or not. In addition to the crystallographic compatibility, strength of the material, as quantified by the $\sigma_y^M - \sigma_{SIM}$ value (see Section 5.4.3) was also expected to have an influence on the evolutionary behavior during training, thus was also examined.

Figure 9.1 illustrates ε_{irr} per cycle vs. number of cycles for different SMA systems under different training stresses. Figure 9.1a shows the level of ε_{irr} generated under 80 MPa. All the tested materials reach a saturated level of ε_{irr} by the end of 100 thermal cycles as evident from the trends of ε_{irr} per cycle, indicating that additional thermal cycling will only cause minor changes in the total deformation of the materials. However, the number of cycles to reach a certain level of stability is different for different compositions. All TiNiPd based and TiNiPt HTSMAs require around 40 cycles, while equiatomic TiNi requires at least 80 cycles to obtain a stable behavior. Once least square lines are fitted to the almost linear regions (between cycles 40-100 for TiNi(Pd,Pt) HTSMAs and cycles 80-100 for equiatomic TiNi), it is obvious that the saturation value of ε_{irr} per cycle is different for equiatomic TiNi and TiNi(Pd,Pt) HTSMAs (Figure 9.1a). Equiatomic TiNi generates a ε_{irr} of 0.024 % per cycle after 100 thermal cycles, while all TiNiPd based HTSMAs generate ε_{irr} of 0.002 % per cycle, almost ten times smaller than that of equiatomic TiNi. TiNiPt, on the other hand, has an intermediate value of 0.011 % per cycle (see the table on p.168).

Increasing the training stress level does not change the observed trend in ε_{irr} per cycle or the number of cycles required to achieve stable shape memory behavior. One exception seen in the 150 MPa training results is the continuously increasing ε_{irr} per cycle values for TiNiPt HTSMA (Figure 9.1b). As mentioned in Chapter VII, this material was thermally cycled between 50 °C and 500 °C to ensure full transformation. Thus, the failure to achieve stability is due to creep effect as a result of high

temperatures and intermediate loads. This effect is even more pronounced at 200 MPa (Figure 9.1c).

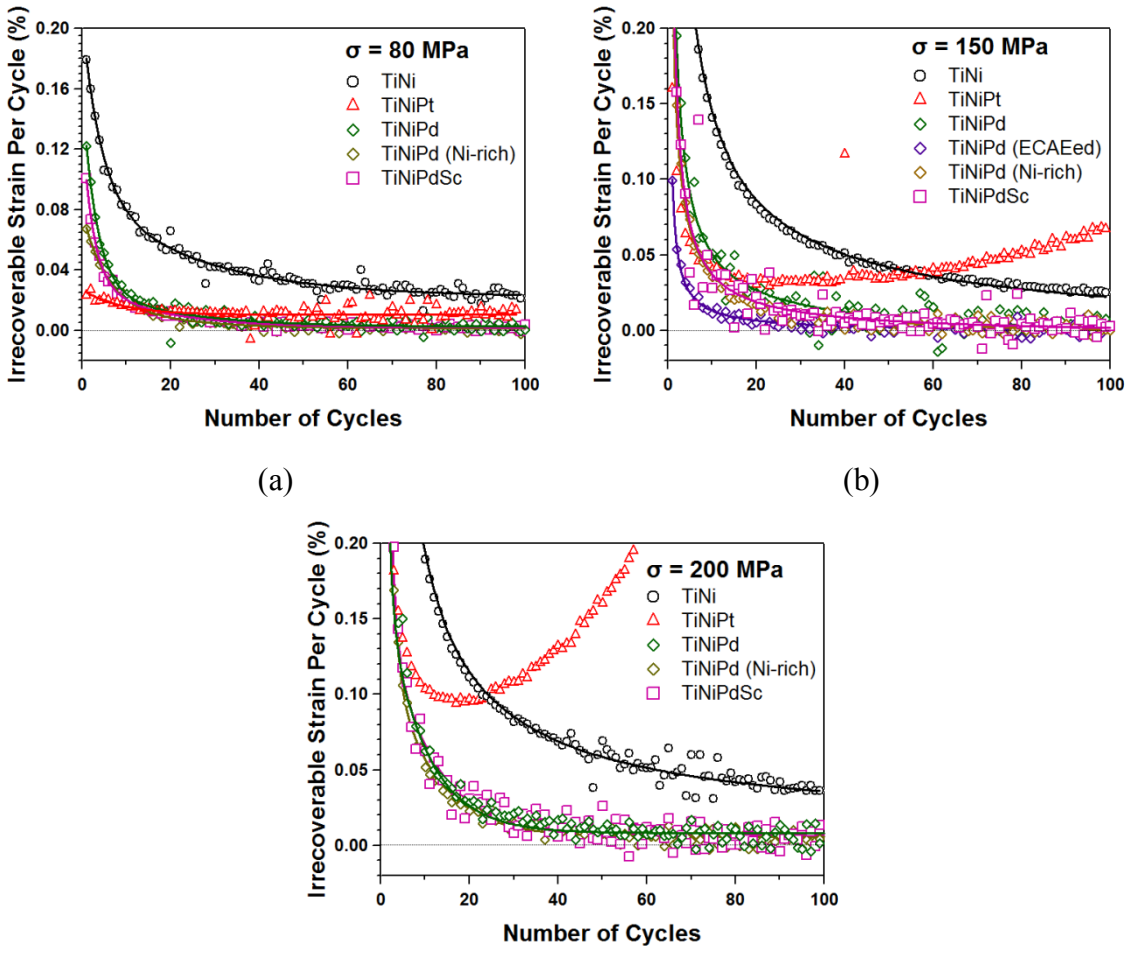

Figure 9.1 Irrecoverable strain, ε_{irr}, per cycle vs. cycle number for different SMA systems under (a) 80 MPa, (b) 150 MPa and (c) 200 MPa.

For the other SMA systems, the difference in the saturation levels of ε_{irr} per cycle can still be discerned in Figure 9.1b. Equatomic TiNi converges to a value of 0.021 %,

while TiNiPd based HTSMAs have a saturation ε_{irr} per cycle value of 0.002 %. On the same figure, it should be noted that ECAE processing significantly reduces the amount of plasticity generated during the early cycles and the number of cycles required to achieve a certain level of functional stability. However, at the end of 100 thermal cycles, the functional stability levels of the ECAE processed sample are indistinguishable from those of the unprocessed TiNiPd based HTSMAs. Similar shape memory evolution trends were also recorded for training under 200 MPa. TiNiPt sample fractured at the 60^{th} cycle due to excessive ε_{irr} caused by creep effects.

As mentioned above, regardless of the processing method or slight changes in composition, all TiNiPd HTSMAs converge to a similar stability level at the end of 100 thermal cycles. The effects of solid-solution strengthening using Sc, ECAE processing or using a slightly Ni-rich TiNiPd composition can be better observed from Figure 9.2, in which the total irrecoverable strains (ε_{tot}) developed during the 100 thermal cycles are plotted as a function of cycle number. An increase in stress results in an increased ε_{tot} for all materials. Equiatomic TiNi exhibits the highest levels of plasticity at all stress levels. Figure 9.2b shows the ε_{tot} levels for different materials during training under 150 MPa. As-received TiNiPd exhibits a ε_{tot} of 2.26 % at the end of 100 thermal cycles. Sc addition reduces this value to 1.74 %, whereas using a slightly Ni-rich TiNiPd composition results in a value of 1.52 %. ECAE processing greatly reduces the amount of plasticity evidenced by a ε_{tot} of 0.58 % at the end of 100 cycles. It should be noted a large part of these differences comes from the initial training cycles since the slopes of the curves after the first 40 cycles are very small.

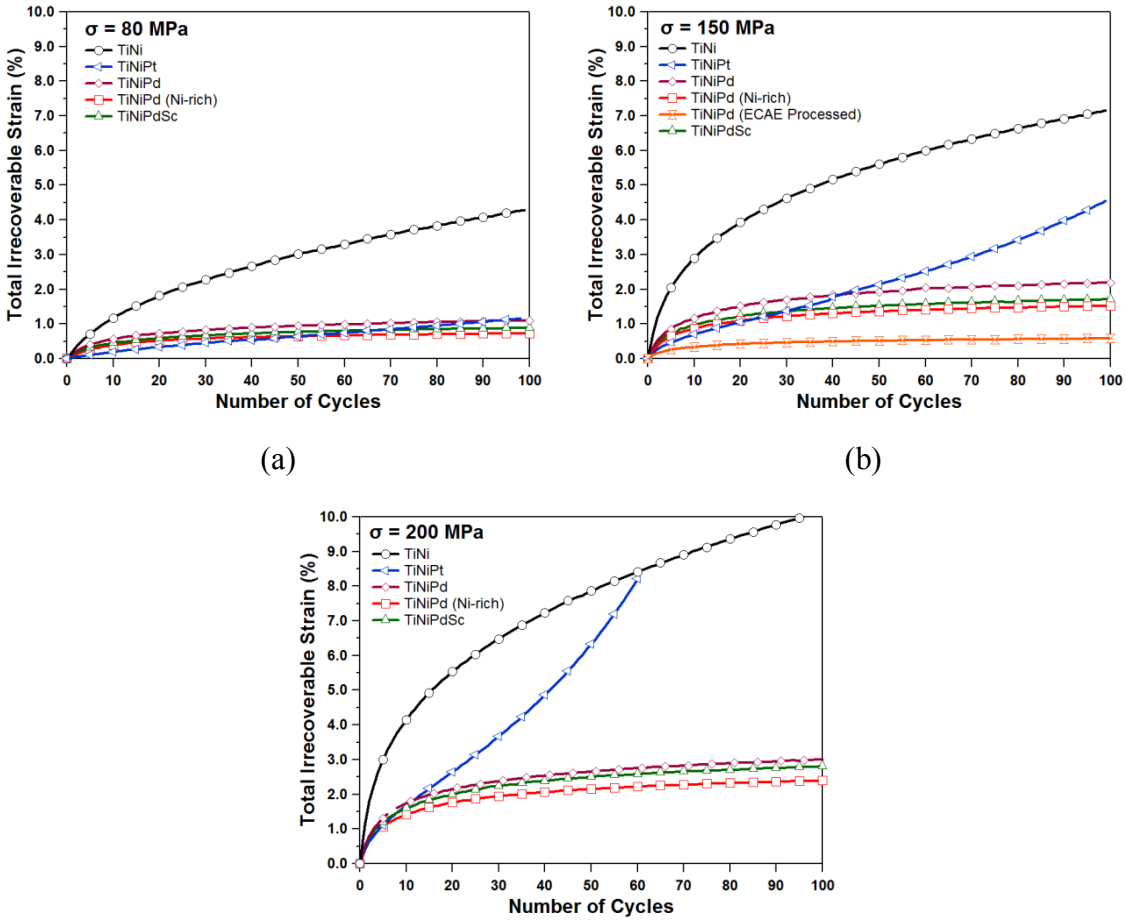

Figure 9.2 Total irrecoverable strain (ε_{tot}) levels generated for different SMA compositions during training under (a) 80 MPa, (b) 150 MPa and (c) 200 MPa.

9.1.1 Influence of Strength on the Evolutionary Behavior during Training

Isothermal monotonic loading tests were conducted to assess the strength levels of the SMAs before training. Tests were done under compression at M_s + 15 °C to measure the $\sigma_y^M - \sigma_{SIM}$ levels, which represented the resistance of the materials against

plastic deformation (See Section 5.4.3). A higher difference indicated a higher resistance to defect generation. Figure 9.3 illustrates the stress vs. strain behavior of different alloys tested. Strength levels were found to be quite similar among as-received materials. Since ECAE processing greatly improved the $\sigma_y^M - \sigma_{SIM}$ of $Ti_{49.5}Ni_{25}Pd_{25}Sc_{0.5}$ (Section 5.4.3) beyond the levels that could be measured within the capacity of the testing frame (Table 9.1), similar behavior was also expected from the ECAE processed $Ti_{50.5}Ni_{24.5}Pd_{25}$ and thus, an additional monotonic loading test was not conducted. The improvements in $\sigma_y^M - \sigma_{SIM}$ levels after ECAE processing were previously shown to be due to the increased dislocation density and refinement of grains. The same microstructural changes are considered to be effective in the early cycles of training for the ECAE processed TiNiPd, which accumulated smaller amounts of ε_{irr} compared to all other as-received compositions (Figure 9.1b and 9.2b).

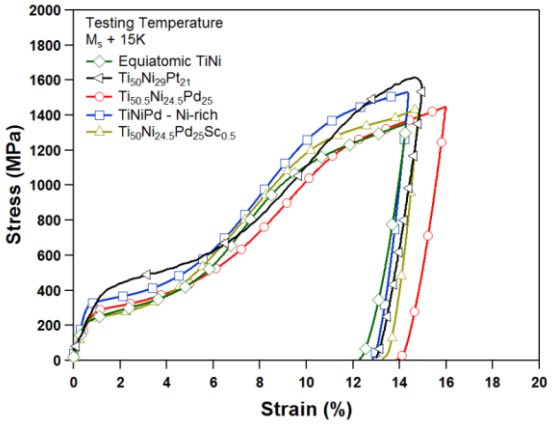

Figure 9.3 Monotonic loading test results for the SMAs in the as-received condition. Tests were performed under compression at $M_s + 15°C$ to ensure similar thermodynamic conditions for each material.

9.1.2 Influence of Compatibility between Transforming Phases on the Evolutionary Behavior during Training

The assumption at the beginning of the chapter was that the dimensional stability of an SMA was mainly dictated by the λ_2 value. Materials with λ_2 values closer to 1 were expected to generate less plasticity upon further thermal cycling after achieving stability of the microstructure, e.g. once the reorientation process and formation of retained martensite were saturated. Figure 9.4 shows a plot of saturation values of ε_{irr} per cycle during 80 MPa training with respect to the deviation of λ_2 values from 1 for different SMA compositions tested in this study.

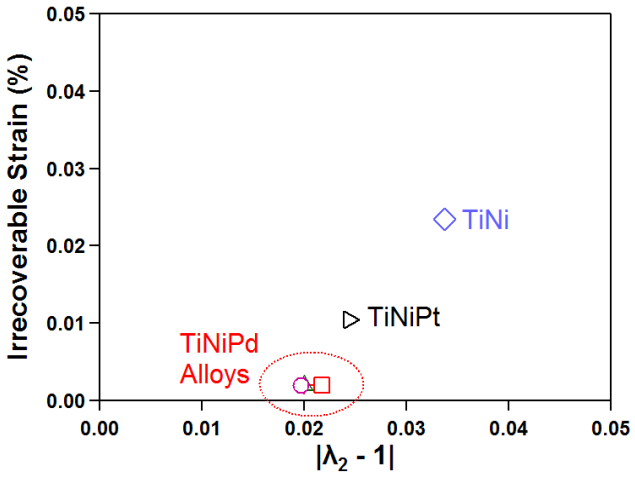

Figure 9.4 Saturation level of ε_{irr} per cycle at the end of thermomechanical training under 80 MPa for different SMA systems with respect to the deviation of λ_2 from 1.

It was previously stated in Section 4.2.1 that 0.5 at. % Sc addition slightly improved the compatibility of $Ti_{50.5}Ni_{24.5}Pd_{25}$ by decreasing λ_2 from 1.0171 to 1.0158. λ_2

calculations were repeated for this study, this time taking measurements from the as-received tension specimens to be trained. All TiNiPd based HTSMAs had very close λ_2 values between 1.020 and 1.022. Small differences were found between $Ti_{50.5}Ni_{24.5}Pd_{25}$ and its Ni-rich counterpart, confirming the results of Frenzel *et al.*[89], who showed that crystallographic compatibility increased with increasing Ni contents in binary TiNi. TiNiPt HTSMA exhibited a relatively higher value of λ_2 which might explain the higher saturation value of ε_{irr} per cycle during 80 MPa training (Figure 9.4). Equiatomic TiNi had the largest deviation from λ_2=1, and also had the largest saturation value of ε_{irr} per cycle. To summarize the results, the λ_2 values for different SMA systems, along with $\sigma_y^M - \sigma_{SIM}$ values, and saturation values of ε_{irr} during 80, 150 and 200 MPa training cycles are listed in Table 9.1.

Table 9.1 $\sigma_y^M - \sigma_{SIM}$, λ_2 values, saturation levels of ε_{irr} during 80, 150 and 200 Mpa training cycles for different SMA systems.

	$\sigma_y^M - \sigma_{SIM}$ **(MPa)**	λ_2	**Saturation level of ε_{irr} (%) during 100-cycle training under**		
			80 MPa	**150 MPa**	**200 MPa**
TiNi	824	0.96630	0.024	0.021	0.034
TiNiPd	930	1.02176	0.002	0.002	0.008
TiNiPd (Ni-rich)	972	1.01998	0.002	0.001	0.006
TiNiPd (ECAE)	> 1300	1.02176		0.002	
TiNiPdSc	966	1.01999	0.002	0.002	0.007
TiNiPt	1071	1.02439	0.011		

9.2 Summary and Conclusions

$\sigma_y^M - \sigma_{SIM}$ levels, which are heavily dependent on microstructural characteristics such as grain size and dislocation density, were found to have an influence on the evolution of shape memory behavior during early training cycles. Yet, the amount of defects that could be generated upon further thermal cycling once the SMA has reached an almost dimensionally stable behavior was determined by the level of compatibility between transforming phases, i.e. λ_2 value. A strong correlation was found between the λ_2 value and the saturation level of ε_{irr} per cycle. More compatible materials with λ_2 values closer to 1 exhibited smaller ε_{irr} per cycle values upon further thermal cycling after reaching stability.

It is not exactly known whether λ_2 is solely responsible for the amount of defect generation after a stable behavior is achieved with negligible changes in shape and transformation temperatures upon further thermal cycling. Encouraged by the recent unpublished results of NASA Glenn Research Center (GRC) on Ni-rich TiNiHf HTSMAs, it is plausible to state that a highly incompatible structure with λ_2 values largely deviating from 1 might exhibit small levels of plasticity if it has high strength levels. The Ni-rich TiNiHf HTSMA, after proper aging heat treatments, illustrated exceptional dimensional stability with almost no ε_{tot} generated during a100-cycle training under 150 MPa. On the other hand, the Ni-rich TiNiHf in its as-extruded form accumulated a certain value of ε_{tot} at the end of the same training procedure. Both of these conditions have the same values of λ_2, yet the age-hardenend TiNiHf is known to

exhibit much higher strength levels compared to the as-extruded condition [134]. These results are hinting the fact that strength of a material might play a more influential role on the overall functional stability of an SMA actuator compared to crystallographic compatibility between transforming phases.

CHAPTER X

MAIN CONCLUSIONS AND FUTURE DIRECTIONS

The functional stability, determined as a measure of change in the shape and the transformation temperatures of an SMA during repeated actuation, was studied in a model HTSMA, $Ti_{50.5}Ni_{24.5}Pd_{25}$ alloy. Different processing methods were undertaken to modify the response of the alloy and the underlying mechanisms responsible for property enhancement or deterioration were studied.

The main reason for functional instability was attributed to the creation of lattice defects (primarily dislocations) during repeated transformation cycles and thus several methods were successfully conducted to improve the functional stability of $Ti_{50.5}Ni_{24.5}Pd_{25}$ HTSMAs for actuator applications. The mechanism for the improvement was either strengthening of the material against defect generation or saturating the material with defects such that additional defect generation upon further thermal cycling was harder to occur. Solid-solution strengthening using Sc microalloying, and grain refinement and work hardening via ECAE were used to increase strength levels, while thermal cycling at a constant stress level was utilized to saturate the HTSMA with defects. The outcome of all these methods was a decrease in the amount of defects generated upon further actuation cycles, leading to more functionally stable behavior.

While strength was a key parameter for functional stability during a relatively small number of thermal cycles, crystallographic incompatibility between transforming phases dictated the functional stability behavior of an SMA in the long run.

As a result of intensive characterization and processing studies conducted throughout this investigation, it is possible to outline fundamental mechanical and microstructural properties for the ideal HTSMA actuator, which is expected to show near perfect functional stability.

1. The ideal HTSMA actuator should have increased strength levels against plasticity. Solid-solution strengthening of $Ti_{50.5}Ni_{24.5}Pd_{25}$ HTSMA using Sc improved functional stability through an increase in strength and crystallographic compatibility between transforming phases, while slightly decreasing transformation temperatures. Grain refinement and work hardening through severe plastic deformation (SPD) is another viable method to achieve increased strength levels, however the decrease in transformation temperatures and transformation strain at a given actuation stress level should be taken into consideration. Post-deformation annealing heat treatments were found to recover both transformation temperatures and transformation strain levels without severely affecting functional stability.
2. As an alternative to the aforementioned strengthening methods, further defect generation can be suppressed if there is already a large volume of transformation induced defects present in the microstructure. Thermal cycling $Ti_{50.5}Ni_{24.5}Pd_{25}$ HTSMA under constant stress for a relatively small number of cycles (10 cycles) improved the functional stability levels similar to the levels achieved with Sc addition. Thermal cycling came with added benefits of increased transformation

temperatures and a 2% TWSM strain. Even larger TWSM strains (up to 2.5%) could be obtained after a 100 thermal cycle training procedure.

3. A high level of crystallographic compatibility between transforming phases is the signature for a reduced potential for defect generation, thus enhanced functional stability. The SMA systems examined in this study had a martensitic structure of either orthorhombic (B19) or monoclinic (B19') symmetry. Since the compatibility levels associated with B19' to cubic (B2) transformation were found to be lower compared to B19 to B2 transformation, the HTSMAs with B19 martensite are preferred for a better functional stability. However, they exhibit lower transformation strains than the SMAs with B2 to B19' transformation.

Most SMA actuators operate based on the one-way shape memory effect (OWSME) combined with a biasing force to reset the SMA after each actuation cycle. In this respect, the two-way shape memory effect (TWSME) was investigated as an alternative means of actuation in HTSMAs to eliminate the need for a rebiasing force. Thermomechanical training in the form of thermal cycling under constant stress levels was employed to induce the TWSME in $Ti_{50.5}Ni_{24.5}Pd_{25}$ HTSMA. Compared to binary TiNi, $Ti_{50.5}Ni_{24.5}Pd_{25}$ exhibited much smaller degradation during stress-free thermal cycling, which makes this material an ideal candidate for actuator applications exploiting the TWSME.

Although the stability of the TWSME during stress-free cycling is a pre-requisite for actuator applications, its stability during cycling under load is much more critical since most applications require the SMA to do work against a load. The TWSME in

$Ti_{50.5}Ni_{24.5}Pd_{25}$ HTSMA degraded substantially during thermal cycling under an opposing external force. The amount of degradation was found to be related mainly to the upper cycle temperature. An increase in the strength of the HTSMA through SPD processing did not prove to be useful in preventing this degradation.

Work output of the TWSME was measured for the first time in $Ti_{50.5}Ni_{24.5}Pd_{25}$ HTSMA. Work output levels well above those obtained from conventional TiNi and Cu-based SMAs, were achieved. Although, these values are substantially lower compared to what can be achieved under a biased OWSME, it is still possible to utilize the TWSME in these HTSMAs for applications requiring relatively low work output.

Overall, through intensive processing and thermomechanical characterization, $Ti_{50.5}Ni_{24.5}Pd_{25}$ HTSMA was proven to be a promising candidate for high-temperature actuator applications with reasonable functional stability for both OWSME and TWSME. However, the thermomechanical characterization in this study consisted of a relatively low number of thermal cycles compared to the large number of cycles required for real applications. Therefore, more work is needed to assess the high-cycle transformation-induced fatigue performance of these HTSMAs. To the author's best knowledge, there is no study on the fatigue life of TiNiPd HTSMAs during high-cycle OWSME actuation. The causes of fatigue failure and influences of microstructural parameters already mentioned in this study on the fatigue life should be investigated as a future work. Similarly, if TWSME is intended to be used for a high number of cycles in application, its stability during stress-free or load-biased thermal cycling should be addressed accordingly.

REFERENCES

[1] Otsuka K, Ren X. Prog Mater Sci 2005;50:511.

[2] Otsuka K, Wayman CM. Shape memory materials. Cambridge: Cambridge University Press; 1998.

[3] Lindquist PG, Wayman CM. Shape memory and transformation behavior of martensitic Ti-Pd-Ni and Ti-Pt-Ni alloys. In: Duerig TW, Melton KN, Stockel D, Wayman CM, editors. Engineering aspects of shape memory alloys. London: Butterworth-Heinemann; 1990.

[4] Donkersloot HC, Van Vucht JHN. J. Less-Common Met 1970;20:83.

[5] Golberg D, Xu Y, Murakami Y, Morito S, Otsuka K, Ueki T, Horikawa H. Scr Metall Mater 1994;30:1349.

[6] Golberg D, Xu Y, Murakami Y, Morito S, Otsuka K, Ueki T, Horikawa H. Intermetallics 1995;3:35.

[7] Golberg D, Xu Y, Murakami Y, Otsuka K, Ueki T, Horikawa H. Mater Lett 1995;22:241.

[8] Cai W, Otsuka K, Asai M. J. Mater Sci Technol 1999;40 895.

[9] Shimizu S, Xu Y, Okunishi E, Tanaka S, Otsuka K, Mitose K. Mater Lett 1997;34:23.

[10] Xu Y, Shimizu S, Suzuki Y, Otsuka K, Ueki T, Mitose K. Acta Mater 1997;45:1503.

[11] Boriskina NG, Kenina EM. Phase equilibria in the Ti-TiPd-TiNi system alloys. In: Kimura H, Izumi O, editors. Titanium 80, science and technology. The Metallurgical Society of AIME, New York; 1980.

[12] Otsuka K, Oda K, Ueno Y, Piao M, Ueki T, Horikawa H. Scr Metall Mater 1993;29:1355.

[13] Sakamoto H, Shimizu K. Trans. Japan Inst Metals 1986;27:601.

[14] Noebe RD, Padula SA, Bigelow G, Rios O, Garg A, Lerch B. In: Armostrong WD, editor. Proceedings of SPIE: smart structures and materials 2006: active materials: behavior and mechanics; 2006, p. 617010-1

[15] Bigelow G. MS thesis, Colorado School of Mines; 2006.

[16] Gautier E, Patoor E. Mechanics of solids with phase changes – CISM International Centre for Mechanical Sciences, courses and lectures. Springer, Berlin; 1997.

[17] Ma J, Karaman I, Noebe RD. Int Mater Rev 2010;55:257.

[18] McCormick PG, Liu Y. Acta Metall Mater 1994;42:2407.

[19] Strnadel B, Ohashi S, Ohtsuka H, Ishihara T, Miyazaki S. Mater Sci Eng A 1995;202:148.

[20] Humbeeck JV. J Phys IV France 1991;01:C4.

[21] Hornbogen E. J Mater Sci 2004;39:385.

[22] Yang WS, Mikkola DE. Scr Metall Mater 1993;28:161.7

[23] Suzuki Y, Xu Y, Morito S, Otsuka K, Mitose K. Mater Lett 1998;36:85.

[24] Tian Q, Wu J, Cheng Y. J. Mater Sci Technol7 2001;19:179.

[25] Bigelow G, Noebe RD, Padula SA, Garg A. In: Berg B, editor. Proceedings of the international conference on shape nemory and superelastic technologies; 2006. p.113.

[26] Bigelow GS, Gaydosh DJ, Garg A, Padula SA, Noebe RD. In: Miyazaki S, editor. Proceedings of the international conference on shape nemory and superelastic technologies; 2007. p.83.

[27] Kumar PK, Lagoudas DC, Zanca KJ, Lagoudas MZ. In: William DA, editor. Proceedings of SPIE: smart structures and materials 2006. p.617012.

[28] Contardo L, Guénin G. Acta Metall Mater 1990;38:1267.

[29] Perkins J, Bobowiec P. Metall Mater Trans A 1986;17:195.

[30] Rios-Jara D, Guenin G. Acta Metall 1987;35:109.

[31] Cai W, Tanaka S, Otsuka K. Mater Sci Forum 2000;327-3:279.

[32] Bigelow G, Padula SA, Garg A, Gaydosh D, Noebe RD. Metall Mater Trans A 2010;41:3065.

[33] Grossmann C, Frenzel J, Sampath V, Depka T, Eggeler G. Metall Mater Trans A 2009;40:2530.

[34] Perkins J, Sponholz RO. Metall Trans A 1984;15:313.

[35] Stalmans R, Van Humbeeck J, Delaey L. Acta Metall Mater 1992;40:501.

[36] Stalmans R, Vanhumbeeck J, Delaey L. J Phys IV 1991;1:403.

[37] Stalmans R, Vanhumbeeck J, Delaey L. Acta Metall Mater 1992;40:2921.

[38] Stalmans R, Vanhumbeeck J, Delaey L. In: Yamamoto R, Furubayashi E, Doi Y, Fang R, Liu B, editors. Advanced Materials '93, V - A & B - A: Ecomaterials 1993; B: Shape memory materials and hydrides; 1994. p.927.

[39] Stalmans R, Vanhumbeeck J, Delaey L. Scr Metall Mater 1994;31:1573.

[40] Cingolani E, Ahlers M. Mater Sci Eng A 1999;273:595.

[41] Rapacioli R, Torra V, Cesari E, Guilemany JM, Miguel JR. Scr Metall 1988;22:261.

[42] Perkins J. Scr Metall 1974;8:1469.

[43] Escher K. Metallwissenschaft 1990;44:23.

[44] Hebda DA, White SR. Smart Mater Struct 1995;4:298.

[45] Lahoz R, Gracia-Villa L, Puertolas JA. J Eng Mater 2002;124:397.

[46] Lahoz R, Puértolas JA. J Alloys Compd 2004;381:130.

[47] Liu Y, Liu Y, Van Humbeeck J. Acta Mater 1998;47:199.

[48] Liu Y, McCormick PG. Scr Metall 1988;22:1327.

[49] Liu Y, McCormick PG. Acta Metall Mater 1990;38:1321.

[50] Luo HY, Abel EW. Smart Mater Struct 2007;16:2543.

[51] Nishida M, Honma T. Scr Metall 1984;18:1293.

[52] Quandt E, Halene C, Holleck H, Feit K, Kohl M, Schlomacher P, Skokan A, Skrobanck KD. Sensor Actuat A 1996;53:434.

[53] Scherngell H, Kneissl AC. Scr Mater 1998;39:205.

[54] Scherngell H, Kneissl AC. Acta Mater 2002;50:327.

[55] Wada K, Liu Y. J Alloys Compd 2008;449:125.

[56] Wang JJ, Omori T, Sutou Y, Kainuma R, Ishida K. Scr Mater 2005;52:311.

[57] Wang LM, Zheng YF, Cai W, Meng XL, Zhao LC. J Mater Sci Technol 2001;17:263.

[58] Wang Z, Zu X, Feng X, Dai J Mater Lett 2002;54:55.

[59] Wang ZG, Zu XT, Dai JY, Fu P, Feng XD. Mater Lett 2003;57:1501.

[60] Chen LP, Si NC. J Alloys Compd 2008;448:219.

[61] Shelyakov AV, Bykovsky YA, Matveeva NM, Kovneristy YK. J Phys IV 1995;5:713.

[62] Wang ZG, Zu XT, Feng XD, Zhu S, Dai JY, Lin LB, Wang LM. Mater Lett 2002;56:284.

[63] Meng XL, Chen F, Cai W, Wang LM, Zhao LC. Mater Trans 2006;47:724.

[64] Wang LM, Meng XL, Cai W, Zhao LC. J Mater Sci Technol 2001;17:13.

[65] Meng XL, Zheng YF, Cai W, Zhao LC. J Alloys Compd 2004;372:180.

[66] Kockar B, Karaman I, Kim JI, Chumlyakov YI, Sharp J, Yu C-JM. Acta Mater 2008;56 3630.

[67] Liu Y, McCormick PG. Acta Metall Mater 1994;42:2401.

[68] Miyazaki S, Ohmi Y, Otsuka K, Suzuki Y. J Phys 1982;43:255.

[69] Brailovski V, Khmelevskaya IY, Prokoshkin SD, Pushin VG, Ryklina EP, Valiev RZ. Phys Metals Metallogr 2004;97:S3.

[70] Sergueeva AV, Song C, Valiev RZ, Mukherjee AK. Mater Sci Eng A 2003;339:159.

[71] Treppmann D, Hornbogen E, Wurzel D. J Phys IV 1995;5:569.

[72] Tian Q, Wu J. Mater Sci Eng A 2002;325:249.

[73] Wu J, Tian Q. Intermetallics 2003;11:773.

[74] Bigelow GS, Padula SA, Garg A, Noebe RD. In: Dapino MJ, editor. Proceedings of SPIE: behavior and mechanics of multifunctional and composite materials; 2007. p.2B1.

[75] Kockar B, Atli KC, Ma J, Haouaoui M, Karaman I, Nagasako M, Kainuma R. Acta Mater 2010;58:6411.

[76] Ishida A, Sato M, Miyazaki S. Mater Sci Eng A 1999;273:754.

[77] Nishida M, Wayman CM, Chiba A. Metallography 1988;21:275.

[78] Potapov PL, Shelyakov AV, Gulyaev AA, Svistunov EL, Matveeva NM, Hodgson D. Mater Lett 1997;32:247.

[79] Kockar B, Karaman I, Kim JI, Chumlyakov Y. Scr Mater 2006;54:2203.

[80] Meng XL, Cai W, Chen F, Zhao LC. Scr Metall Mater 2006;54:1599.

[81] Cui J, Chu YS, Famodu OO, Furuya Y, Hattrick-Simpers J, James RD, Ludwig A, Thienhaus S, Wuttig M, Zhang ZY, Takeuchi I. Nat Mater 2006;5:286.

[82] Bhattacharya K, Conti S, Zanzotto G, Zimmer J. Nature 2004;428:55.

[83] Ball JM, James RD. Phil Trans R Soc Lond A 1992;338:389.

[84] Miyazaki S, Otsuka K, Wayman CM. Acta Metall 1989;37:1873.

[85] Saburi T, Wayman CM. Acta Metall 1979;27:979.

[86] James RD, Hane KF. Acta Mater 2000;48:197.

[87] Delville R, Schryvers D, Zhang Z, James RD. Scr Mater 2009;60:293.

[88] Zarnetta R, Takahashi R, Young ML, Savan A, Furuya Y, Thienhaus S, Maass B, Rahim M, Frenzel J, Brunken H, Chu YS, Srivastava V, James RD, Takeuchi I, Eggeler G, Ludwig A. Adv Funct Mater 2010;20:1917.

[89] Frenzel J, George EP, Dlouhy A, Somsen C, Wagner MFX, Eggeler G. Acta Mater 2010;58:3444.

[90] Perkins J, Hodgson D. Two-way shape memory effect. In: Duerig TW, Melton KN, Stockel D, Wayman CM, editors. Engineering aspects of shape memory alloys. London: Butterworth-Heinemann; 1990.

[91] Fukuda T, Deguchi A, Kakeshita T, Saburi T. Mater T JIM 1997;38:514.

[92] Valiev RZ, Langdon TG. Prog Mater Sci 2006;51:881.

[93] Segal VM. Mater Sci Eng A 1995;197:157.

[94] Mughrabi H, Hoppel HW, Kautz M, Valiev RZ. Z Metallkd 2003;94:1079.

[95] Hoppel HW, Valiev RZ. Z Metallkd 2002;93:641.

[96] Kockar B, Karaman I, Kulkarni A, Chumlyakov Y, Kireeva IV. J Nucl Mater 2007;361:298.

[97] Karaman I, Karaca HE, Maier HJ, Luo ZP. Metall Mater Trans A 2003;34:2527.

[98] Karaman I, Kulkarni AV, Luo ZP. Philos Mag 2005;85:1729.

[99] Pushin VG, Stolyarov VV, Valiev RZ, Lowe TC, Zhu YT. Mater Sci Eng A 2005;410-411:386.

[100] Pushin VG, Stolyarov VV, Valiev RZ, Kourov NI, Kuranova NN, Prokofiev EA, Yurchenko LI. Ann Chim-Sci Mat 2002;27:77.

[101] Pushin VG, Stolyarov VV, Valiev RZ, Kourov NI, Kuranova NN, Prokof'ev EA, Yurchenko LI. Phys Metals Metallogr 2002;94:S54.

[102] Valiev R, Gunderov D, Prokofiev E, Pushin V, Zhu Y. Mater Trans 2008;49:97.

[103] Waitz T, Kazykhanov V, Karnthaler HP. Acta Mater 2004;52:137.

[104] Huang JY, Zhu YT, Liao XZ, Valiev RZ. Phil Mag Lett 2004;84:183.

[105] Kockar B. PhD dissertation, Texas A&M University; 2007.

[106] Furukawa M, Iwahashi Y, Horita Z, Nemoto M, Langdon TG. Mater Sci Eng A 1998;257:328.

[107] Barber RE, Dudo T, Yasskin PB, Hartwig KT. Scr Mater 2004;51:373.

[108] ASTM F2004-05 Standard test method for transformation temperature of nickel-titanium alloys by thermal analysis. ASTM International, West Conshohocken, PA; 2004.

[109] Bozzolo G, Noebe RD, Mosca HO. J Alloys Compd 2005;389:80.

[110] Bozzolo G, Mosca HO, Noebe RD. Intermetallics 2007;15:901.

[111] Sivokha VP, Savvinov AS, Voronin VP, Khachin VN. Phys Met Metall 1982;56:112.

[112] Khachin VN. Doklady Akademii nauk SSSR 1981;257:167.

[113] Matveeva NM, Kovneristyi YK, Savinov AS, Sivokha VP, Khachin VN. J Phys 1982;43:249.

[114] Lindquist PG. PhD thesis, University of Illinois at Urbana-Champaign, 1988.

[115] Lin HC, Wu SK, Chou TS, Kao HP. Acta Metall Mater 1991;39:2069.

[116] Wollants P, Roos JR, Delaey L. Prog Mater Sci 1993;37:227.

[117] Salzbrenner RJ, Cohen M. Acta Metall 1979;27:739.

[118] Ortin J, Planes A. Acta Metall 1988;36:1873.

[119] Hamilton RF, Sehitoglu H, Chumlyakov Y, Maier HJ. Acta Mater 2004;52:3383.

[120] Hane KF, Shield TW. Acta Mater 1999;47:2603.

[121] Roitburd AL, Kurdjumov GV. Mater Sci Eng 1979;39:141.

[122] Kokorin VV, Gun'ko LP, Shevchenko OM. Phys Met Metall 1992;74:502.

[123] Stachowiak GB, McCormick PG. Acta Metall 1988;36:291.

[124] Miller DA, Lagoudas DC. Mater Sci Eng A 2001;308:161.

[125] Hornbogen E. J Mater Sci 1999;34:599.

[126] Miyazaki S, Imai T, Igo Y, Otsuka K. Metall Trans A 1986;17:115.

[127] Qiu S, Padula SA, Noebe RD, Gaydosh DJ, Vaidyanathan R. Acta Mater 2011, in press doi:10.1016/j.actamat.2011.04.009.

[128] Noebe R, Gaydosh D, Padula S, Garg A, Biles T, Nathal M. In: Armstrong WD, editor. Smart structures and materials 2005: active materials: behavior and mechanics; 2005. p.364.

[129] Qiu S. PhD dissertation, University of Central Florida; 2011.

[130] Noebe RD, Draper S, Gaydosh D, Garg A, Lerch B, Penney N, Bigelow G, Padula S. In: Berg B, editor. Proceedings of the international conference on shape nemory and superelastic technologies; 2006. p.409.

[131] Padula SA, Gaydosh DJ, Noebe RD, Bigelow GS, Garg A, Lagoudas D, Karaman I, Atli KC. In: Marcelo JD, Zoubeida O, editors. Proceedings of SPIE: behavior and mechanics of multifunctional and composite materials; 2008. p.692912.

[132] Padula SA, Vaidyanathan R, Gaydosh D, Qiu S, Noebe R, Bigelow G, Garg A. accepted Metall Mater Trans A 2011.

[133] Scherngell H, Kneissl AC. Mater Sci Eng A 1999;273:400.

[134] Bigelow GS, Garg A, Padula Ii SA, Gaydosh DJ, Noebe RD. Scr Mater 2011;64:725.

APPENDIX

FIGURES

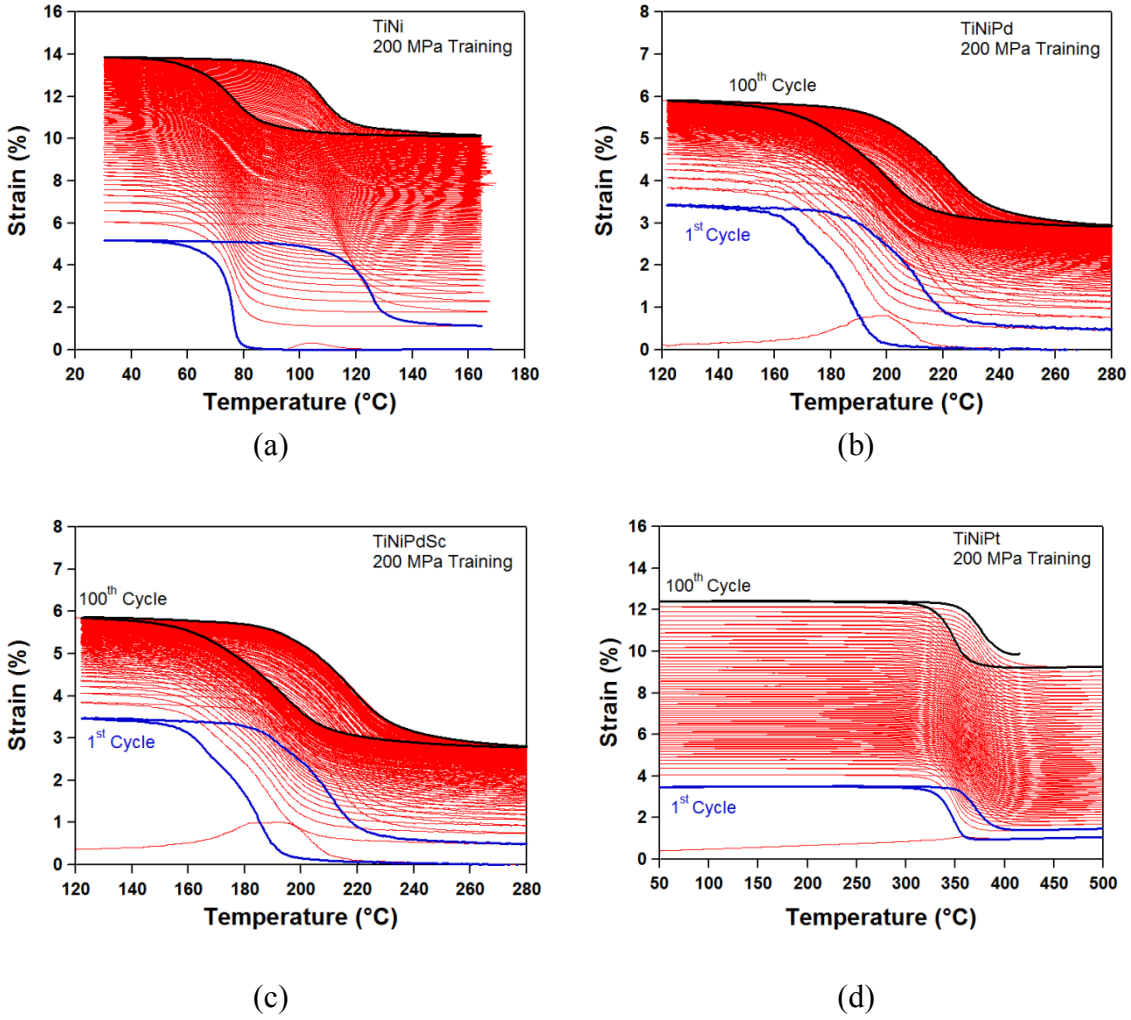

Figure A.1 100-cycle thermomechanical training results for (a) TiNi, (b) TiNiPd, (c) TiNiPdSc and (d) TiNiPt under 80 MPa.

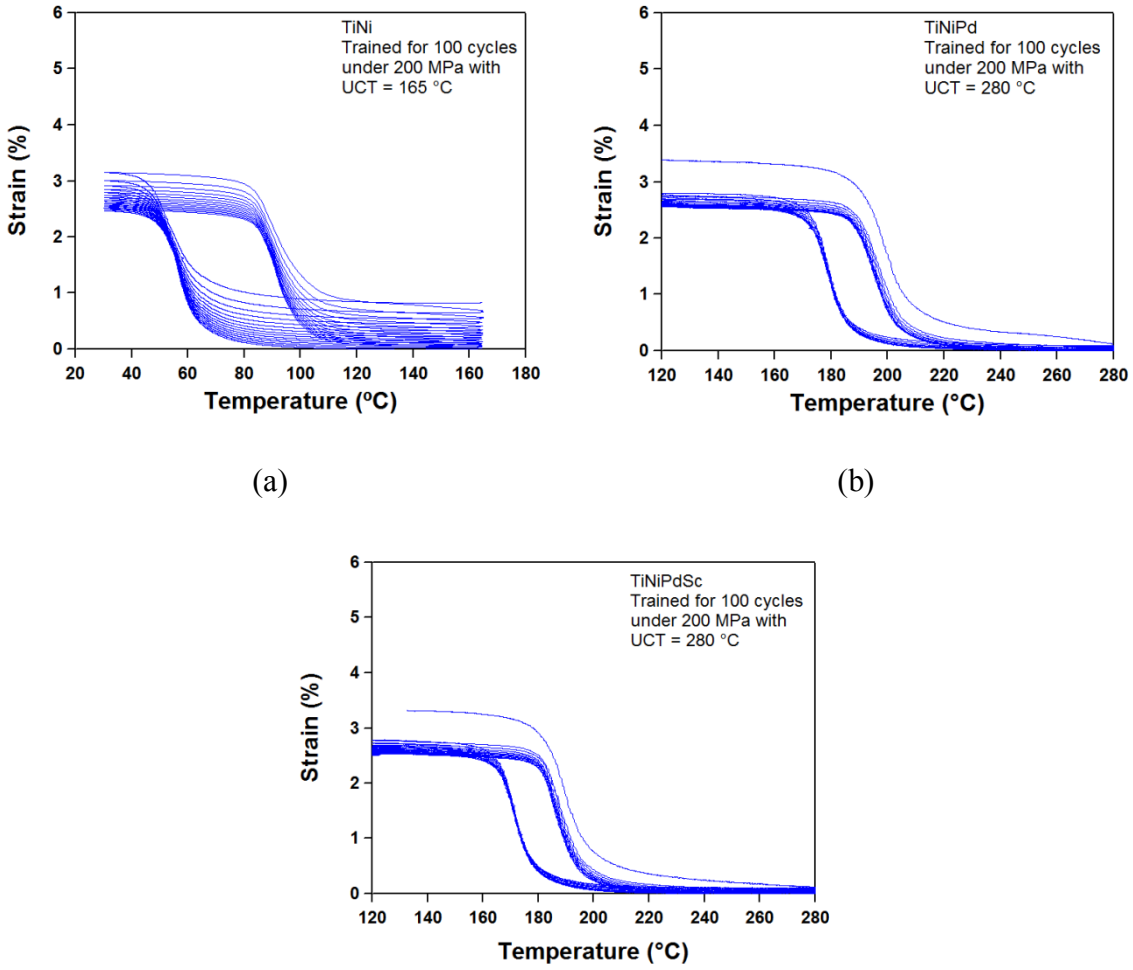

Figure A.2 The evolution of strain vs. temperature behavior during stress-free TWSME cycling for (a) TiNi, (b) TiNiPd and (c) TiNiPdSc

VITA

Kadri C. Atli was born in Istanbul, Turkey. After receiving a B.S. degree in mechanical engineering from Bogazici University in 2002, he took a break from his academic studies until 2005. During this time, he worked as a research and development engineer in G-U Yapi Elemanlari A.S., Istanbul from 2002 to 2003 and Assan Aluminium, Istanbul from 2003 to 2005. In 2007, he received a M.S. degree in mechanical engineering from Bogazici University and started the Ph.D. program at Texas A&M University. During his graduate studies, he continuously held a research assistantship, while publishing five peer-reviewed journal articles and one conference proceeding. He also had the opportunity to present his research in nine international conference symposia. Upon graduation, he will continue his post-doctorate studies in Chemnitz University of Technology in Chemnitz, Germany, studying the dynamic behavior and high-strain rate response of shape memory alloys. His permanent address is:

Department of Mechanical Engineering

c/o Dr. Ibrahim Karaman

Texas A&M University

College Station, TX 77843-3123

Email: canatli@gmail.com